
# Ultrafast Carrier Dynamics of Porous Silicon and Gold-Silicon Composites

By

Rihan Wu

A thesis submitted to
the University of Birmingham
for the degree of
DOCTOR OF PHILOSOPHY

Nanoscale Research Group
School of Physics and Astronomy
College of Engineering and Physical Sciences
University of Birmingham
July 2021

## ABSTRACT

The ultrafast carrier dynamics of nano- and micro-porous silicon and their underlying opto-electronic properties were investigated in this work. The femtosecond pump-probe technique was employed to characterise the excitation, relaxation and recombination processes. The results showed that the recombination rate of the nano-porous silicon is three orders of magnitude higher than that of the crystalline silicon. Auger and Shockley-Read-Hall were the two dominant recombination processes in nano-porous silicon, while the contribution of the bimolecular recombination was diminishing. Due to the fast recombination and high scattering rate of the free carriers in nano-porous silicon, the diffusion process was suppressed. By fitting the rate equation, the recombination time of Auger and Shockley-Read-Hall were retrieved from the experimental results. It was demonstrated that the Auger process was greatly enhanced by the vibrational modes of the surface adsorbates coupling to the phonons of nano-porous silicon.

A study on the micro-porous silicon was conducted to examine the suitability of the material for implementation in an all-optical modulator. A modulation contrast of 30% with a 0.55 ps response time was demonstrated. The modulator was then used to construct a high resolution Time-of-Flight set-up. A pulse broadening caused by group velocity dispersion was measured for the laser pulse traversing a 5 cm silica rod.

To introduce new characteristics to the opto-electronic properties of nano-porous silicon, a novel composite material was fabricated by embedding gold nanoparticles into its pore channels. The combination of plasmonics with semiconducting material greatly enhanced the light coupling efficiency. It was proved that the composite could be used as a SERS substrate which provides an enhancement factor of $10^9$, suitable for a single molecule level detection. Ultrafast dynamics investigation on the composite has also been carried out. The results showed that the free carrier absorption and third order nonlinearity was enhanced by incorporating gold clusters into np-Si.

Dedicated to my parents and my friends

## ACKNOWLEDGMENTS

This is a letter of gratitude to everyone who loves me, helps me, encourages me, and trusts me, not only during my PhD but also in my life.

First of all, I would like to thank my amazing parents for their mental and physical support. I used to be a very annoying child who didn't like to study and always hated school. You did not force me to study and get good grades in my subjects because you were both too busy to educate me. Instead, you always said to your friends: "My daughter is very clever, but her poor grades are because she is not hardworking". So, for your pride (and also mine), I had to study a bit. In the end, I went to a decent university, not the best, but probably good enough for a naughty student like me. I had a simple university life until the last year of my bachelors. I realised that I wanted to go abroad and see the world. I became hardworking to pursue what I really wanted to do. You supported my choice without any doubt, although it would consume quite a lot of money. You believed in me more than myself that I would be able to manage to go abroad and survive in a foreign country. During my PhD, you would always say that I shouldn't work too much, go out and have some fun — just like when I was in secondary school. You would always ask if I still have money and transfer some to me even I didn't need it. You would never put pressure on me or require anything of me. You always listened to my troubles and cheered me up. You are the best parents ever!

I would also like to thank my supervisor, Dr Andrey Kaplan, for all your support and trust. Thank you for selecting me to fill this PhD position and for bringing me to the fantastic field of Ultrafast Spectroscopy — I really love this subject. I cannot imagine enjoying another research field as much as this one. Thank you for tolerating my bad temper and weird working hours. I don't think I would be as patient with a student like me. Thank you for comforting me, instead of blaming me, when I damaged the gratings

in the laser system. You said that people only learn from mistakes, and I really learned a lesson. Even after that, you let me maintain the laser system and align it on my own. I really appreciate all the trust you have given me! I have learned a lot from you over the years. You always have new ideas on research that broadened my knowledge. You always helped me when I got stuck on experiments and pointed me in the right direction. You taught me to think and talk sharp, which has benefited me a lot. I really enjoyed the discussions that we have had on different subjects. There are so so so many other things that I would like to thank you for which would not fit into several pages. You are the best supervisor ever!

I would also like to thank my best sisters, Dr Mahroo Rokni Fard and Dr Mahrokh Rokni Fard. When I met both of you, you were not doctors yet, and now I am the only one left who isn't (sad face). Mahroo, thank you for dragging me to the squash court EARLY every morning, which made me realise that I can get up early. Thank you for all the coffees and cakes that kept my wight constant even when we did exercise every day. I thank you especially for your support during my dark times last summer. I don't know what I would do without you! Thank you for all the lovely food you cooked (although most of them are from your parents, I thank them too!). And most recently, providing me with a warm home (I'm less thankful of the fact that you didn't accept any rent that I transferred you!). You have no idea how much I appreciate the support and love you have given me, boss boss! Rokhi, thank you for most of the reasons listed above too, apart from the morning exercise part, which I guess I should also thank you for that. Thank you for tolerating mine and Mahroo's nerdy physics jokes and all the amazing cakes you made (especially my birthday cake). Thank you for taking so much care in being extremely quiet when I was sleeping during the day (By the way, I really don't hear anything during sleep so just ignore me!). Both of you are really amazing people! You are the best sisters ever!

I would also like to thank my best friend and colleague Jack Collins, the greatest

electronic and programming scientist in our lab and the best drinking companion. I had no idea that electronics can be that fun, and that there are so many types of beer, without you. You were always so helpful and supportive when I had new ideas for our research. I apologise that I didn't have time to finish most of them, such as the NPRL website and the programmable gold impregnation set-up. I feel that there is never enough time for the things we want to do! You always say that I helped you a lot during your PhD, but I think you helped me more! You were extremely supportive during my write-up period. I can't imagine anybody else would read all my thesis and make corrections, apart from our supervisor. Thank you for all the fun activities that we had together: karting (although I broke my neck), skateboarding (although I am still terrible at it), chess (I think you will win more in the end), climbing (hopefully we will have chance to go again after COVID), band practice and drinks after that (the best times ever), various types of games (I am a pro now) and so many other things. There really is not enough time! I am sure we will have time to do all that at some point — life is long, and you will be my friend forever.

In the end, I would like to thank Dr Carmen Popescu for her support during my dark time, fun night-out and relaxing in work breaks. You and Mahroo were my motivation to come to work when I was depressed and had self-doubt. I really miss you, and hopefully, we can meet soon. Thank you Cheng Li for the fried rice, noodles and hotpots, which made me gain 8 kg in a few months. Thank you Dr Yitao Wang for being my late-night companion and for bringing me food when I was starving. Thank you Dr Isabel Ornelas for the great Greece trip, nights out and your suggestions on my chemistry-related projects. Thank you Dr Dimitri Chekulev for your help on our laser system and the discount on my rent. Thank you Dr Wolfgang Thesis, Dr Quanmin Guo, Prof. Leigh Canham and Dr Ziyou Li for all your support and encouragement during my PhD.

I love you all, and I am who I am because of you.

*Dance like there's nobody watching*

*Love like you'll never be hurt*

*Sing like there's nobody listening*

*Live like it's heaven on earth*

— William W. Purkey

# Contents

# List of Figures

# Chapter One

# Introduction

Electron and phonon dynamics in the matter, such as the excitation and relaxation processes, take place on femto- ($10^{-15}$ s) to pico-second ($10^{-12}$ s) time scales[1]. To observe such fast events, the time resolution of the experimental set-up needs to be in the same range or better. Since the mid-20th century, the development of ultrafast lasers brought the opportunity to monitor these rapid interactions. Following the idea of Albert Einstein in 1916 that identical photons which can form coherent light could be generated by stimulated emission process, Aleksandr Prokhorov and Nikolay Basov proposed (1955) that the sustained stimulated emission can be achieved by pumping a gain medium with multi-level excited states[2]. Based on this, scientists successively constructed Fabry-Perot Resonator for laser generation (Gordon Gould 1957), ruby laser (Theodore Maiman 1960), GaAs diode laser ( Robert N. Hall 1962) and helium-neon gas-line laser (Alan White and Dane Rigden 1963) in a short period of time[3]. Soon after, the development of mode-locking and Q-switching technology made it possible to generate ultrafast laser pulses with duration down to the femtosecond range, allowing for the detection of fast dynamic processes[4, 5].

Prior to the ultrafast laser development, E. Muybridge in 1878 demonstrated a high-

speed photography technique that pioneered the science in time-resolved spectroscopy[6]. He successfully achieved an exposure time of $10^{-3}$ s with several cameras equipped with fast shutters, and for the first time, revealed the movement of horseshoes by taking a series of photos of a running horse. This 'freezing' of motion at different times is the basis of time-resolved measurements. In 1899, H. Abraham and co-authors proposed the 'pump-probe' concept, in which light pulses are not only used to monitor the material response but also to trigger changes in material properties[7]. The trigger and monitor pulse is called 'pump' and 'probe', respectively. By changing the arrival time difference between two light pulses, the time-resolved Kerr effect of liquid $CS_2$ was measured and characterised[8]. However, this was before the development of ultrafast lasers, so they only managed to measure the variation of optical properties on the nanosecond scale. As the technology matured, ultrafast lasers provided shorter and shorter pulses which enabled finer measurements, such as the rapid evolution of chemical and electronic states.

As early as 1964, E. Archbold *et al.* employed a Q-switched ruby laser beam to study the time-resolved spectra of laser-generated plasmas[9]. Later in 1979, C.V. Shank *et al.* has measured the time-resolved absorption spectrum in GaAs by using an 800 nm degenerate pump-probe set-up and successfully observed the screening of exciton by photo-excited carriers[10]. Nowadays, with the improvement in ultrafast laser systems and data acquisition techniques, more reliable and complex experiments can be performed using pump-probe set-ups. For example, the development of supercontinuum light generation and nonlinear optical parametric amplification broadened the observation range over a wide spectrum. The appropriate pump and detection wavelengths can be selected for different dynamic processes rather than single-wavelength degeneracy experiments. The latest developments in free electron lasers and terahertz sources further extend the pump-probe measurements to the X-ray and terahertz regions[11, 12]. In addition, by using more than two laser pulses, multi-dimensional pump-probe spectroscopy has been developed to study

the structures and dynamics of biological and chemical molecules[13]. Other techniques, such as pump-probe ellipsometry, pump-probe microscopy and time-resolved fluorescence spectroscopy, all play important roles in various disciplines[14, 15, 16].

This PhD works mainly focuses on probing the carrier dynamics of porous silicon with ultrafast laser covering the range of Short Wavelength Infrared Region (SWIR 1 - 3 μm) to Middle Wavelength Infrared Region (MWIR 3 - 5 μm)[17]. Silicon was selected as the main material of this research due to its wide application range in electronic, opto-electronic and photonic systems[18, 19]. It was first discovered as an element in 1823 and applied in semiconductor devices in 1906, soon after becoming the most famous and widely used semiconducting material[20, 21]. As the primary substance of transistors, silicon is essential for computer central processing units (CPU), sensors and other devices that require integrated circuits[22]. Moreover, the concept of photonic integrated circuits attracted considerable attention in the late 20th century, owing to its advantage of higher speed and lower thermal effects over conventional electronic circuits. Silicon was then considered as the best material to associate photonics with electronics due to its excellent optical properties in telecommunication wavelength and the mature production line of integrated electronic circuits[23]. Therefore, researchers have focused their attention on understanding the thermal, electronic and optical properties of silicon and have conducted a number of excellent studies in the past few decades.

In particular, time-resolved spectroscopy was extensively used to study the dynamics and transport properties of the free carriers in silicon. It is essential to understand the free carrier behaviour of material to further determine its suitable application. For example, the high efficiency of transistors and sensors require carriers to migrate to the electrodes before they recombine[24, 25, 26]. In contrast to that, rapid electron-hole relaxation and recombination are needed for applications such as modulators and switches[27, 28, 29]. Preliminary research on the detection of excited free carriers in silicon using the

pump-probe technique can be traced back to 1981. A. Aydinli and co-workers studied the time-resolved transmission and reflection of silicon and observed enhanced absorption after excitation caused by free-carriers[30]. This was the first time-resolved measurement of silicon. Although the authors did not mention the recombination process in the paper, it can be seen from the results that the recombination of free carriers takes about several hundred nanoseconds. Similarly, in 1982 J. M. Liu *et al.* employed picosecond laser and pump-probe technique to investigate the electron-hole plasma formation and melting effects in crystalline silicon. They observed an increase in probe reflection caused by the optical pumping induced semiconductor-metal phase transition[31]. Later on, more attention was paid to modifying the structure and carrier concentration of crystalline silicon in order to alter its optical and electronic properties. A number of outstanding works, such as the charge transport mechanism of amorphous silicon by T. Tiedje[32], and minority-carrier transport in heavily doped silicon by CH. Wang[33] was published in the late 20th century. These studies show that doping and structures can significantly modify the characteristics of silicon, thereby further broadening its application range.

The discovery of quantum confinement effects in nano-porous silicon (np-Si) in 1990 by L.T. Canham opened a new chapter in the silicon industry[34]. Porous silicon (p-Si) is a sponge-like material composed of silicon skeleton and air pores with nanometer to micrometer size. Compared to conventional crystalline and amorphous silicon, it has the advantage that its mechanical, electronic and optical properties can be widely adjusted by tuning the porosity, skeleton diameter and surface chemistry[35]. Besides, its enormous surface to volume ratio and constrained skeleton size lead to the confinement of free carriers, enhancing its efficiency of photoluminescence and light harvesting[36, 37, 38, 39, 40]. It has been demonstrated that these unique properties of p-Si brings new possibilities for pharmaceutical and food industries[35], sensing and imaging[41], optical communication[42, 43], anti-reflection coatings in photovoltaic devices[44] and displays[45].

Although many experiments have been conducted to study the carrier dynamics of p-Si, most of them focused on its optical properties in the visible to near-infrared wavelength range[46, 47], while left its performance in MWIR region out of the research. This is due to the difficulties to implement a suitable light source, constructing an efficient light path, maintaining a short pulse duration until it reaches the sample and obtaining a low-noise signal with a suitable detection method[48]. However, this area of research would be interesting due to its potential applications in night vision, thermal imaging, free-space communication, military defence system and astronomy telescopes[49]. The loss of MWIR propagating in space is less than visible and near-infrared due to the existence of atmosphere transmittance window and the low scattering cross-section of long-wavelength light (Rayleigh scattering inverse proportional to the fourth power of wavelength). These advantages make MWIR suitable for remote-distance applications[50].

Despite the enormous interests and demands in the market, the development of MWIR materials and technologies is still lagging behind other wavelength regions. Taking sensing materials as an example, only a few types, such as amorphous silicon, lead selenide (PbSe) and mercury cadmium telluride (MCT), are suitable and have been commercialized for MWIR detection. Most of them have the disadvantages of narrow bandwidth, nonlinear response or low-temperature requirements[51, 52, 53]. To resolve this deficiency, it is urgent to explore new materials suitable for MWIR applications. Previous studies have shown that p-Si has the suitable optical properties in this wavelength range[54, 55, 40]. Therefore, this work aims to further study the excited state response of different types of p-Si by probing with MWIR light, and to examine its performance when used as an optical modulator.

The thesis is organised as the following: Chapter 2 introduced the theoretical background involved in this work, including propagation of electromagnetic waves in the linear regime, nonlinear optics, carrier dynamics and transport in semiconductors, as

well as effective medium theory. Chapter 3 focused on the experimental set-ups that have been used in this work. The major part of it was the femtosecond laser system and pump-probe set-up. The principle of operation was introduced, along with a detailed description of optical components used. Chapters 4, 5 and 6 presented the results obtained from experiments. In Chapter 4, the excitation and recombination processes of optically excited free carriers in np-Si were investigated. The pump used to excite the charge carriers has a wavelength of 800 nm, which is above the band-gap of silicon. Mid-wavelength infrared light in the range of 3.4 to 5 μm was employed to probe the excited sample properties. The time-resolved transmittance and reflectance for different pump intensities and probe wavelengths were measured. An optical model based on the effective medium approximation, including the contribution of free carriers, is used to analyse the experimental results. The carrier density as a function of pump intensity and probe wavelength was extracted from the fitting. Analysis shows that Shockley-Read-Hall and Auger processes are the main mechanisms of np-Si recombination, and the contribution of diffusion is insignificant. Moreover, the recombination rate of the Shockley-Read-Hall and Auger process was evaluated as a function of probe wavelength. The results revealed that the Auger recombination is more active when the probe wavelength is in resonance with the vibration mode of the np-Si surface adsorbates. The effective recombination rate of np-Si is about three orders of magnitude higher than in bulk silicon. This study gives a deep insight into the recombination mechanism of np-Si, which can be further used in the design of np-Si based optical and opto-electronic devices.

In Chapter 5, a different type of p-Si, macro-porous silicon (mp-Si), was studied. Different from np-Si, the pore size of mp-Si is in micrometer range and is regularly distributed over the entire sample. This Chapter, instead of focusing on the recombination mechanism, pay more attention to the application side of mp-Si. It demonstrates the possibility of employing mp-Si as the material for the MWIR all-optical modulator. The

same experimental set-up as in Chapter 4 was used to conduct the experiments. The pump can be treated as a 'switch' of the modulator, and the probe is the signal carrying the modulated information. The experimental results successfully demonstrated a modulation depth of 80% with a 3.8 mJ/cm$^2$ pump. In addition, an example of ultrafast switching within 0.55 ps with 30% signal contrast was presented by using the reflection mode of the modulator. Afterwards, the all-optical modulator was further combined with the Time-of-Flight (ToF) technique. It was shown that the ToF of the signal passing through silicon with a few centimeters thickness can be retrieved from the results. The high resolution of the set-up was demonstrated by the observation of pulse broadening due to the group velocity dispersion, the value of which was retrieved and compared to the literature. It was concluded that the resolution of the set-up is mainly limited by the pump pulse duration.

In Chapter 6, a novel composite material that combined plasmonics with semiconductors was proposed. It was made by embedding gold (Au) nanoparticles in the pores of np-Si through an immersion-plating method. This is the first reported plasmonic-semiconductor 3D composite material with the advantages of low cost, high uniformity and suitability for mass production. It has been reported that incorporating plasmonic material with a semiconductor can enhance its light coupling efficiency, beneficial for applications such as detectors and light-harvesting devices[56, 57]. However, due to the lack of a suitable method, most published works focus on the surface modification of semiconductors with plasmonics. The most successful case was the invention of Surface Enhanced Raman Spectroscopy, where the presence of metal nanoparticles localise the electric field by orders of magnitude, leading to the magnification of the Raman signal. However, only the modification of the surface constrains the application range of the composite material. On the one hand, there is a limited number of metal clusters that can be fitted into a certain area on the surface, therefore, limits the magnification of the

field intensity. On the other hand, this type of composite is relatively fragile compared to the bulk material. Therefore, a 3D composite material was fabricated with the Au nanoparticles uniformly distributed over the np-Si. To examine the localised surface plasmon resonance (LSPR) of the composites, the scattering spectrum and dark field image were taken. The results show a scattering peak centred around 700 nm, which indicates the presence of LSPR. In addition, the linear and nonlinear optical properties of the composite were studied through time-resolved measurements. The LSPR was excited by the optical pump with 790 nm wavelength and probed by 2.5 μm light. The results demonstrated that embedding Au nanoparticles in np-Si amplifies its excited response to the probe. It was also found that the nonlinear response of the composites is also enhanced compared to bare np-Si, owing to the presence of LSPR. After characterising the optical properties, the composite was used as the substrate for Raman measurements. Due to the high density of the Au clusters and the short distance between each of the clusters, the Raman signal is greatly enhanced. The results show that the enhancement factor can reach $10^9$ by using the 3D composite, which corresponds to a single molecule detection level.

Chapter 7 is the conclusion of this work. The main achievement and findings are introduced in this Section. There are also two chapters in the appendix, including the detailed derivation of the scattering matrix method and nonlinear measurements of bare np-Si, which helped my understanding of the np-Si optical properties.

This PhD work involves a deep investigation of the carrier dynamics, linear and nonlinear optical response of different types of porous silicon and its metal-cluster impregnated composites in a broad spectrum range spanning from visible to MWIR region. The experimental results and following analysis answered several unresolved questions in the field of nanomaterials, such as, the influence of the surface chemistry on carrier recombination process, the contribution of localised plasmon resonance towards the nonlin-

earity of the metal-semiconductor composites, as well as the charge transport mechanism at the metal-semiconductor interface. So far, these findings have not been reported by any other research groups, and they will certainly contribute to the understanding of the light-semiconductor interaction and help broaden the range of potential applications of porous silicon.

# Chapter Two

# Theoretical Background

This Chapter focuses on the theory behind the carrier dynamics and transport mechanism of excited state semiconductors. Prior to this, the linear and nonlinear responses of unexcited materials to incoming light are interpreted by classical electromagnetic (EM) theory. As the most conclusive and powerful equation set in EM theory, Maxwell's equations are introduced in Section 2.1. In addition, the detailed derivation of the transfer matrix method (TMM) for simulating the intensity of transmitted and reflected light through a slab material is presented. By comparing the simulation results with the experimental ones, material properties such as absorption coefficient and refractive index can be obtained. However, the TMM is only applicable to the linear regime while it cannot be used when the material's polarisation has a nonlinear relation with the incident electric field. This nonlinear response occurs when the nonlinear coefficient is significant, or the incident light intensity is high. In Section 2.2, the concept of optical nonlinearity and several nonlinear phenomena are discussed in detail.

As for optically excited semiconductors, the excitation and decay process (such as relaxation and recombination) of free carriers and its time scale are exclusively introduced in Section 2.3. The change of free carrier concentration as a function of time during the

decay process is represented by a rate equation. The dominant recombination pathway of a specific material can be determined by fitting the experimental results to the rate equation if the carrier concentration is known. There are two ways to estimate the carrier concentration of an excited material: It either can be estimated through the absorbed pump fluence, or can be extracted from experimental results by using an optical model that combines the Drude model with TMM. The Drude model is used to incorporate the contribution of free carriers to the dielectric function of the material. Thus, the change of transmittance and reflectance of samples due to the free carrier injection can then be fitted, and the carrier concentration can be extracted. Beside, the carrier scattering rate, which also plays a vital role in the recombination process, can be obtained through this model. A detailed discussion is included in Section 2.3.

Section 2.4 targets the Effective Medium Theory (EMT), which is a suitable approach to approximate the response of composite materials to an incoming electromagnetic field. The sub-wavelength porous silicon used in this work is one type of hybrid material with a structural element size smaller than that of the wavelength of incident light. Under this condition, EMT can be used to approximate the effective dielectric function of composites based on the fraction of each constituent for both homogeneous and inhomogeneous mixing. Compared with the exact solution of the EM response of ordered structure silicon (uniform mixing), EMT has the advantages of fast calculation speed and low computational cost. While for inhomogeneous mixed materials (random structure), it is almost impossible to obtain their explicit EM response, therefore, EMT is essential for accessing their optical properties. It has been proved that a good approximation of the effective dielectric function of randomly mixed materials can be obtained by EMT[58, 59].

## 2.1 Maxwell Equation and Transfer Matrix Method

Maxwell equations are a set of partial differential equations which describe the relationship between charge density, current, electric and magnetic fields. It is a mathematical description of classical electromagnetic theory and can explicitly explain the generation, interaction and propagation of electric and magnetic fields. The most common form of Maxwell equations can be written as[60]:

$$\nabla \cdot \vec{E} = \frac{\rho}{\epsilon_0} \quad (Gauss's\, law), \tag{2.1}$$

$$\nabla \cdot \vec{B} = 0 \quad (Gauss's\, law\, for\, magnetism), \tag{2.2}$$

$$\nabla \times \vec{E} = -\frac{\partial \vec{B}}{\partial t} \quad (Faraday's\, law), \tag{2.3}$$

$$\nabla \times \vec{B} = \mu_0 \epsilon_0 \frac{\partial \vec{E}}{\partial t} + \mu_0 \vec{J} \quad (Ampere's\, law), \tag{2.4}$$

where $\vec{B}$ denotes the magnetic flux density, $\vec{E}$ is the electric field strength, $\rho$ is the electric charge density, $\vec{J}$ represents the electric current density, $\epsilon_0$ is vacuum permittivity ($8.854 \times 10^{-12}$ F/m), and $\mu_0$ is vacuum permeability ($4\pi \times 10^{-7}$ H/m).

Gauss's law (Eq.2.1) states that the electric fields are always left from positive charges and point to negative charges, and the amount of electric field flow through a closed surface (electric flux) is proportional to the charge inside the surface. This is easier to understand from its integral form: $\oint \vec{E}\, d\vec{A} = \frac{Q}{\epsilon_0}$, where Q is the charge enclosed by a surface. Gauss's law for magnetism (Eq.2.2) states that there is no source for the magnetic field. Therefore, the magnetic flux through a closed area is always zero. From these two Gauss's laws, it can be concluded that a charge can generate electric fields while the magnetic field is a non-source field. Faraday's and Ampere's laws further explain how a time-varying magnetic/electric field induces an electric/magnetic field. These two

self-sustaining equations describe the propagation of electromagnetic field in space, and the wave equation can be derived from them (assume in vacuum):

$$\nabla \times (\nabla \times \vec{E}) = \nabla \times (-\frac{\partial \vec{B}}{\partial t}) = -\frac{\partial}{\partial t}(\nabla \times \vec{B}) = -\mu_0 \epsilon_0 \frac{\partial^2 \vec{E}}{\partial^2 t} \tag{2.5}$$

$$\nabla \times (\nabla \times \vec{E}) = \nabla(\nabla \cdot \vec{E}) - \nabla^2 \vec{E} = -\nabla^2 \vec{E} \tag{2.6}$$

The wave equation of electric field is obtained by combining Eq.2.5 with Eq.2.6:

$$\frac{\partial^2 \vec{E}}{\partial^2 t} - \frac{1}{\mu_0 \epsilon_0} \nabla^2 \vec{E} = 0 \tag{2.7}$$

Same practice can be applied to derive the magnetic field wave equation. By comparing with the general wave equation $\frac{\partial^2 \vec{V}}{\partial^2 t} - \nu^2 \nabla^2 \vec{V} = 0$, the speed of electric wave is retrieved $c_0 = \frac{1}{\sqrt{\mu_0 \epsilon_0}}$. This is essentially the speed of light in vacuum.

The next step is to consider the propagation of EM fields in a medium. The energy of an electromagnetic wave is absorbed when it encounters the atoms of a material. The absorbed energy causes the displacement of electrons with respect to the nucleus position. This process is called polarisation. The polarisability of a material is described by the dielectric constant of the material $\epsilon$. For materials with larger polarisability (higher $\epsilon$), they respond strongly (separation of an electron from nuclei is greater) to the incident field than materials with weaker polarisability. After a short time, the electrons return to their original position, and the energy is released again. This vibration of electrons forms a new EM wave with the same frequency as the incident one, which is then absorbed by the next atom. This process repeats until the EM wave leaves the media. Since the absorption and release of energy require additional time, the velocity of the wave is reduced compared to the vacuum velocity. In addition, loss occurs during the absorption and re-emission

process. Therefore, the dielectric constant $\epsilon$ is a complex parameter, with the real part representing propagation and the imaginary part describing the extinction of the EM wave.

In order to describe mathematically the material influence on EM field, Maxwell equations are modified by incorporating the material permittivity $\epsilon$ and permeability $\mu$ in Eq.2.4 as $\nabla \times \vec{B} = \mu_0 \mu \epsilon_0 \epsilon \frac{\partial \vec{E}}{\partial t} + \mu_0 \mu \vec{J}$. The wave equation changes accordingly and the speed of light becomes $c = \frac{1}{\sqrt{\mu_0 \mu \epsilon_0 \epsilon}}$. The additional factor $\epsilon$ in the equation confirms that the speed of light in the medium is reduced compared to in vacuum. In homogeneous, isotropic materials, Maxwell equations can be simplified by considering $\rho = 0$, $J = 0$, $\mu = 1$ and $\epsilon$ as scalar values. This indicating the EM field propagating through the medium will only be affected by the material's polarisability.

Knowing the propagation characteristics of EM waves in the medium, the interaction between EM waves and material boundaries also needs to be considered by incorporating the boundary conditions:

$$(\vec{E_2} - \vec{E_1}) \times \vec{n_{12}} = 0 \quad (Electric\, field), \tag{2.8}$$

$$(\vec{H_2} - \vec{H_1}) \times \vec{n_{12}} = 0 \quad (Magnetic\, field), \tag{2.9}$$

where $\vec{H} = \frac{1}{\mu_0}\vec{B}$ (constitutive equation) is the magnetic field strength and $\vec{n_{12}}$ is the normal vector from medium 1 pointing towards medium 2 as shown in Figure 2.1. From the boundary condition, it can be seen that the tangential component of $\vec{E}$ and $\vec{H}$ are continuous across the interface[61].

Since the material reacts linearly to the incident electromagnetic wave, its response can be expressed in a matrix form. The method using this matrix to analyse the optical response of materials is called the Transfer Matrix Method (TMM). The mathematical expression of TMM is derived from the boundary conditions and Maxwell's equations.

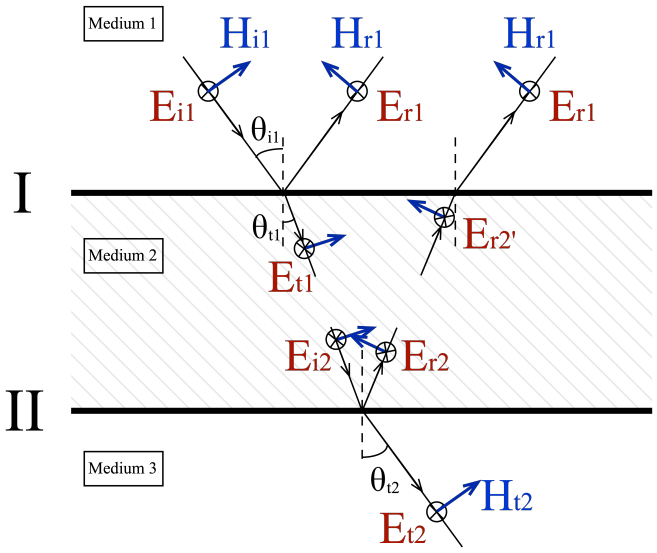


Figure 2.1: Reflection and transmission of EM wave at the boundaries of a dielectric slab. For simplicity, both medium 1 and 3 are assumed to be the vacuum.

Take a dielectric slab sitting in vacuum as an example (Figure 2.1), light with an incident angle of $\theta_{i1}$ is partially reflected at the first interface while the rest is transmitted. Due to the continuity of the tangential components of the electric and magnetic fields, the following relation holds for the s-polarised (E field oscillates out of the incidence plane) light:

$$E_i + E_r = E_t \tag{2.10}$$

$$H_i cos\theta_i - H_r cos\theta_i = H_t cos\theta_t \tag{2.11}$$

The EM field on the two sides of the first boundary (medium 1 and 2) has the relation:

$$\begin{cases} E_1 = E_{i1} + E_{r1} = E_{t1} + E_{r2'} \\ H_1 = H_{i1} cos\theta_{i1} - H_{r1} cos\theta_{r1} = H_{t1} cos\theta_{t1} - H_{r2'} cos\theta_{r2}, \end{cases} \tag{2.12}$$

with the angle relation of $\theta_{i1} = \theta_{r1}$ and $\theta_{t1} = \theta_{r2}$. A similar equation set can be obtained

at the second boundary[60]:

$$\begin{cases} E_2 = E_{i2} + E_{r2} = E_{t2} \\ H_2 = H_{i2}cos\theta_{i2} - H_{r2}cos\theta_{r2} = H_{t2}cos\theta_{t2}, \end{cases} \tag{2.13}$$

with $\theta_{i2} = \theta_{t1}$. Inside the slab, the wave experience a phase shift due to the change of wavevetor $k = k_0 n$, where $k_0$ is the wavevector in vacuum and n is the refractive index of medium 2. The optical path length of the slab is $l = dcos\theta_{t1}$. The E field just before the second boundary encounters the phase shift accumulated through the entire slab:

$$E_{i2} = E_{t1}exp(-ikl) \quad (forward\,propagation), \tag{2.14}$$

$$E_{r2} = E_{r2'}exp(ikl) \quad (backward\,propagation), \tag{2.15}$$

Further simplification of Maxwell equations (Eq.2.1 — Eq.2.4) results in a relation between E and B field: $-ik\vec{E} = -i\omega\mu_0\vec{H}$ with $k = k_0 n = \dfrac{\omega n}{c_0}$, where $\omega$ is the angular frequency of the EM wave. Therefore, the relation between electric and magnetic field can be written as:

$$\vec{H} = n\sqrt{\frac{\epsilon_0}{\mu_0}}\vec{E}, \tag{2.16}$$

By combining Eq.2.12 — Eq.2.16, the relation between the E and H fields on both sides of the slab (medium 1 and 3 in Fig.2.1) is obtained:

$$E_1 = E_2 coskl + H_2 isinkl/\sqrt{\frac{\epsilon_0}{\mu_0}}ncos\theta_{t1}, \tag{2.17}$$

$$H_1 = E_2 isinkl\sqrt{\frac{\epsilon_0}{\mu_0}}ncos\theta_{t1} + H_2(coskl), \tag{2.18}$$

which is then rearranged in a matrix form:

$$\begin{bmatrix} E_1 \\ H_1 \end{bmatrix} = \begin{bmatrix} coskl & isinkl/\sqrt{\frac{\epsilon_0}{\mu_0}}ncos\theta_{t1} \\ isinkl\sqrt{\frac{\epsilon_0}{\mu_0}}ncos\theta_{t1} & coskl \end{bmatrix} \begin{bmatrix} E_2 \\ H_2 \end{bmatrix}, \tag{2.19}$$

The matrix connecting the E and H field of both sides of the slab (medium 2) is the transfer matrix of the slab. For a multi-layer material, each layer can be represented by a transfer matrix $M_i$. The total transfer matrix of the multi-layer is $M_{total} = M_1 \times M_2 \times \dots M_i \times \dots M_j$, with $j$ the total number of layers.

The reflection and transmission coefficient of a material can be worked out from the TMM:

$$r = \frac{Y_0 m_1 + Y_0 Y_s m_2 - m_3 - Y_s m_4}{Y_0 m_1 + Y_0 Y_s m_2 + m_3 + Y_s m_4}, \tag{2.20}$$

$$t = \frac{2Y_0}{Y_0 m_1 + Y_0 Y_s m_2 + m_3 + Y_s m_4}, \tag{2.21}$$

with $M_{total} = \begin{bmatrix} m_1 & m_2 \\ m_3 & m_4 \end{bmatrix}$, $Y_0 = Y_s = \sqrt{\frac{\epsilon_0}{\mu_0}} cos\theta_{i1}$ for a slab placed in the vacuum. Accordingly, the reflectance $R = \mid r^2 \mid$ and transmittance $T = \frac{Y_s}{Y_0} \mid t^2 \mid$ are obtained, which can be used to fit with experimental results and retrieve the material's dielectric function. However, the TMM is numerically unstable because of the growing exponential term in the backward propagating wave[62]. When the material is lossy, such as metal, the exponential term grows rapidly and can cause calculation errors. Appendix A of this thesis discusses a more stable method, the Scattering Matrix Method (SMM), revised from TMM to solve the instability issue.

## 2.2 Optical Nonlinearity

As mentioned at the beginning of this Chapter, the material's polarisation $P$ is linearly proportional to the electric field $E$ in the linear optical regime. The mathematical expression of this relation is $P = \epsilon_0 \chi^{(1)} E$, with susceptibility $\chi^{(1)} = \epsilon - 1$. However, if

the intensity of incident light is high or the material has a strong nonlinear response, the above equation is expanded to a power series[63]:

$$P = \epsilon_0[\chi^{(1)}E + \chi^{(2)}E^2 + \chi^{(3)}E^3...] \tag{2.22}$$

where $\chi^{(2)}$ and $\chi^{(3)}$ are known as the second and third order nonlinear optical susceptibilities.

Second order nonlinearities (SON) can only occur in noncentrosymmetric materials. The most common case of SON is the second harmonic generation (SHG), also known as the frequency doubling process. By expanding the second order polarisation $P(t)^{(2)} = \epsilon_0\chi^{(2)}E(t)^2$, with the electric field $E(t) = Ee^{-iwt} + c.c$ ($c.c$ is the complex conjugate), the following equation is obtained:

$$P(t) = \epsilon_0\chi^{(2)}E(t)^2 = 2\epsilon_0\chi^{(2)}EE^* + (\epsilon_0\chi^{(2)}E^2e^{-2iwt} + c.c). \tag{2.23}$$

It can be noticed that a new frequency component $\omega_{new} = 2\omega$ appears in the equation, whose frequency is twice than that of the incident light. This additional component indicates that the incident EM wave is partially converted into a new EM with half of the original wavelength. The energy diagram shown in Figure 2.2 describes this process more intuitively. Figure 2.2(a) shows an example of SHG of 1550 nm light: Two photons are absorbed at the same time and release a photon of double of the incident photon frequency. Figures 2.2(b) and 2.2(c) illustrate two other types of SON phenomena: optical parametric amplification (OPA) and sum frequency generation (SFG). In OPA, the incident light beam with frequency $\omega_p$ is absorbed, and two light beams with lower frequencies $\omega_s$ and $\omega_i$ are generated (they can have the same or different frequencies), which are called 'signal' and 'idler', respectively. The three frequency components need to fulfil the energy conservation $\omega_p = \omega_s + \omega_i$. The femtosecond laser set-up used in

this work consists of several OPA stages to generate tunable wavelengths from fixed wavelength input. SFG can be considered as a reverse process of OPA — two photons with different frequencies are absorbed, and the frequency of the newly generated photon satisfies $\omega_{new} = \omega_1 + \omega_2$.

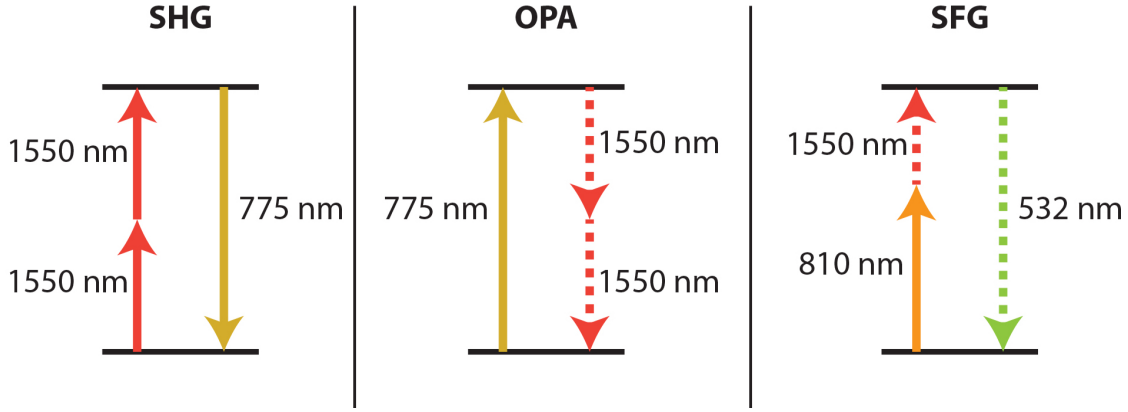


Figure 2.2: Energy diagram of (a) second harmonic generation, (b) optical parametric amplification and (c) sum frequency generation[64].

Unlike SON, the third order nonlinear (TON) process is less efficient since three photons are involved instead of two, and the matching conditions are more difficult to achieve[65, 66]. Typical TON such as third harmonic generation (THG), two-photon absorption (TPA) and intensity-dependent refractive index (IDRI) can occur in centrosymmetric materials. Silicon has a centrosymmetric point group, and its third-order nonlinear susceptibility is larger ($\chi \sim 10^{-18}$ m$^2$/V$^2$) than other semiconductor materials. Therefore, the TON of silicon can be observed and characterised experimentally. It should be noted that for the porous silicon studied in this work, the structures modify the material's properties by changing its band-gap or breaking the centrosymmetry[67, 68], which can lead to enhanced nonlinearity or enable SON.

The mathematical expression of TON can be derived from the nonlinear polarisation relation (Eq.2.22). Take IDRI as an example, the dependence of the material refractive index on the incident electric field is obtained from the following equation:

$$P(\omega)^{(3)} = 3\epsilon_0\chi^{(3)}E(\omega)^3 = 3\epsilon_0\chi^{(3)} \mid E(\omega) \mid^2 E(\omega), \tag{2.24}$$

where $\mid E(\omega) \mid^2 = I$, the intensity of light. Therefore, the total polarisation of the material is:

$$P(\omega)^{(Total)} = \epsilon_0\chi^{(1)}E(\omega) + 3\epsilon_0\chi^{(3)}E(\omega)^3 = \epsilon_0\chi^{(eff)}E(\omega) \tag{2.25}$$

with

$$\chi^{(eff)} = \chi^{(1)} + 3\chi^{(3)} \mid E(\omega) \mid^2 \tag{2.26}$$

It can be seen that the material refractive index $n_{eff} = (1 + \chi^{(eff)})^{\frac{1}{2}}$, varies with different incident light intensities. This equation is further arranged as $n_{eff} = n_0 + n_2 I$, with the linear refractive index $n_0 = (1 + \chi^{(1)})^{\frac{1}{2}}$ and the nonlinear refractive index $n_2 = \frac{3\chi^{(3)}}{4n_0}$[63].

There are a few phenomena related to the IDRI, such as self-focusing/defocusing, self-phase modulation and self-trapping of light. In the case of self-focusing/defocusing, it is caused by the Gaussian-like intensity distribution of the incident beam cross-section. Since the center intensity of the laser beam is higher than the surroundings, a refractive index gradient is formed. This refractive index variation in space makes the material act as a lens, which refracts the beam and distorts the wavefront, resulting in self-focusing or defocusing depending on the sign of nonlinear refractive index $n_2$ (Figure 2.3). The Z-scan technique is one of the approaches for characterising this third-order effect by measuring the intensity of the total and center part of the transmitted light. The total and partial transmission reveals the level of nonlinear absorption and self-focusing/defocusing, respectively. A more detailed discussion of the z-scan technique and TON of crystalline and nano-porous silicon can be found in the Appendix B.

Alternatively, one can directly measure the transmittance and reflectance as a function of light intensity to extract the effective dielectric function of material which

contains the information of nonlinear refractive index $n_2$ and absorption coefficient $\beta$:

$$\epsilon_{eff} = \sqrt{n + n_2 I + i(\alpha + \beta I)}, \tag{2.27}$$

The nonlinear coefficients of the metal-semiconductor composites presented in Chapter 6 were obtained through this method. It should be noted that SMM was used to retrieve the effective dielectric function from the experimental results under the thin-layer linear approximation. In the simulation, the composite slab was split into several sublayers, each with a different incident intensity and dielectric function due to the presence of nonlinear effects. Therefore, the distribution of the light intensity in slab and variation of the dielectric function can be obtained, which was further used to calculate the nonlinear refractive index and absorption coefficient. Although SMM should only be used in a linear regime, by dividing the slab into many layers with each layer's linear effect dominating over the nonlinear process, the linear approximation is valid.

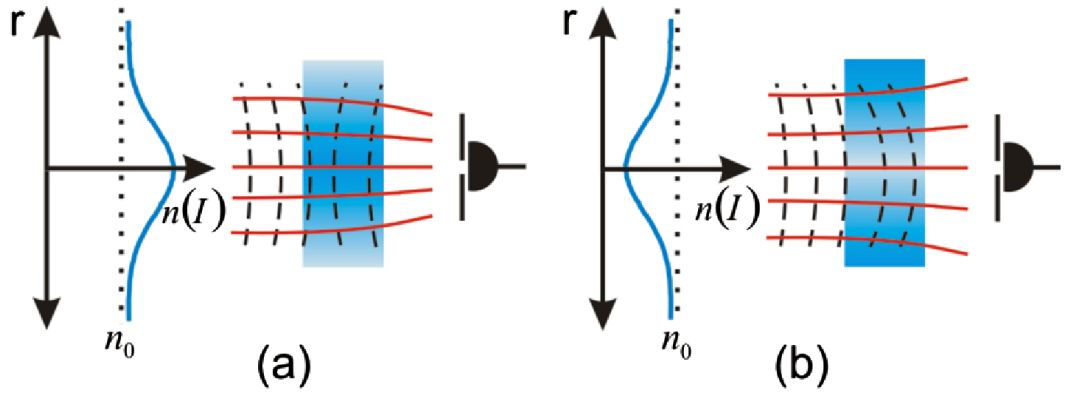


Figure 2.3: Nonlinear self-focusing (a) and self-defocusing (b)[69].

## 2.3 Carrier Dynamics in Semiconductors

Ultrafast light-matter interactions include several complex processes such as carrier excitation, relaxation, recombination and diffusion. Figure 2.4 illustrates the most representative

carrier dynamics for a direct band-gap semiconductor. Initially, an electron absorbs the energy of a photon and 'immediately' jumps from the ground to the excited state. Both energy and momentum need to be conserved in this process. For the direct band-gap semiconductors, the momentum is naturally conserved due to the momentum of a photon being much smaller than that of an electron. Hence the excitation only requires extra energy from photons to cross the band-gap vertically. While for indirect gap semiconductors such as silicon, the electrons require extra momentum from phonons to transit to high energy states due to the maximum of the valence and minimum of the conduction band are not at the same point in k-space.

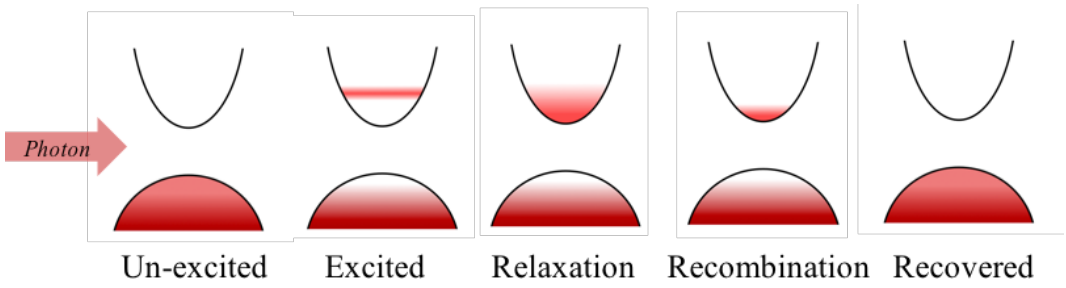


Figure 2.4: Carrier dynamics in direct band-gap semiconductors.

After excitation, the initial population of electrons on the conduction band is in a non-equilibrium state, and their temperature cannot be defined. After a few tens of femtoseconds, electrons redistribute over the conduction band as shown in Figure 2.4 through carrier-carrier scattering without changing the total energy. This process is called electron thermalisation (or relaxation), where the electronic system evolves from a non-thermal to a thermal distribution with rising carrier temperature. It should be noted that the thermalisation of the electronic system is typically referred as 'internal thermalisation', which is different from the 'external thermalisation' through the interaction between carriers and phonons[70]. Afterwards, electrons release their energy and return to the ground state through radiative or non-radiative recombination. Meanwhile, the spatially localised electrons diffuse to the surroundings due to the concentration gradient[71].

The time scales of the ultrafast laser-semiconductor interaction are summarised in Figure 2.5. Compared to the recombination and diffusion processes which take place on longer time scales, excitation and relaxation can be considered as instant phenomenon. Therefore, the perturbed system can be treated as an equilibrium system (carrier temperature can be defined) after a few hundred femtoseconds. The time-dependent carrier concentration, scattering rate and lattice temperature can be calculated to help to understand the temporal variation of material's excited state.

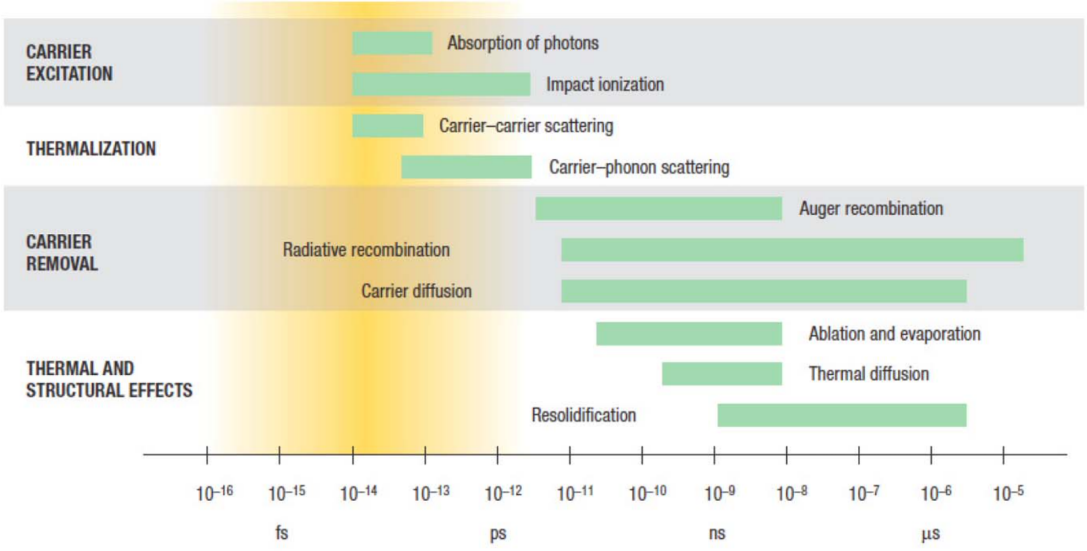


Figure 2.5: Time scale of ultrafast light-semiconductor interaction[72].

Since the excitation and relaxation events are fast and challenging to capture, the main goal of this work is to investigate the carrier recombination and diffusion processes. The pump-probe technique was employed, and its working principle is shown in Figure 2.6. A pump beam excites electrons from the valence to the conduction band with the help of phonons for indirect band-gap material. A probe beam arrives later to examine the optical properties of the material in the excited state. By controlling the arrival time difference between the pump and the probe beam, the temporal evolution of the excited state can be revealed by the change of optical response.

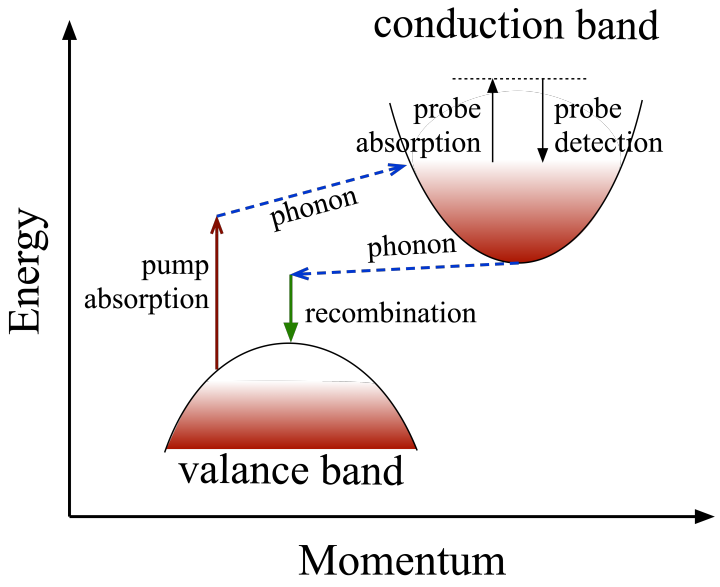


Figure 2.6: An illustration of the carrier dynamics and energy level of indirect band-gap semiconductors.

For direct band-gap materials, photons are re-emitted during the recombination process (radiative decay), while for indirect band-gap materials, the excited electrons lose energy through phonons or impurities instead of re-emitting photons. Shockley-Read-Hall (SRH), electron-hole pair and Auger recombination are the three main non-radiative recombination processes. In SRH, the carriers recombine through a localised trap state that is caused by impurities (such as dopants) or lattice deformation. Electron-hole non-radiative recombination is a bimolecular recombination process in which both the electrons and holes participate in the decay event. Auger recombination occurs when an electron in the conduction band recombines with a hole in the valence band, the released energy is absorbed by another electron which transits to a higher energy state. The relation between the carrier concentration and recombination rate for different recombination terms can be represented by the following rate equation[29]:

$$\frac{dN}{dt} = -bN - cN^2 - dN^3 \tag{2.28}$$

where N is the carrier concentration, b,c and d represent SRH, electron-hole and Auger recombination coefficients, respectively. The above equation further confirmed that SRH only involves a single carrier, while the electron-hole and Auger recombination involve two and three carriers, respectively.

To obtain the time-dependent carrier concentration of an optically excited material from experiments, one needs to associate the concentration with the measured transmittance and reflectance of incident light. As introduced in Section 2.1, the transmittance and reflectance can be fitted with TMM or SMM to retrieve the material dielectric function. The Drude model is then used to correlate the free carrier concentration $N$ with the dielectric function by:

$$\epsilon_{\text{excited}} = \epsilon_{\text{un}} - \frac{{\omega_{\text{p}}}^2}{\omega^2 + i\omega\gamma} \quad , \tag{2.29}$$

with the excited and unexcited material's dielectric function $\epsilon_{\text{excited}}$ and $\epsilon_{\text{un}}$, scattering rate $\gamma$, light frequency $\omega$ and plasmon frequency $\omega_p$:

$$\omega_p^2 = \frac{Ne^2}{\epsilon_0 m_{eff}}, \tag{2.30}$$

where $e$ ($1.610^{-19}$ C) is the elementary charge, $\epsilon_0$ is the vacuum permittivity, and $m_{eff}$ is the effective mass of carriers. Eq.2.29 - 2.30 show that the material dielectric function is not only modified by the carrier concentration $N$ but also by the scattering rate $\gamma$, which contributes to the imaginary part of the excited material's dielectric function. It reveals the extinction of carriers through scattering processes (carrier-phonon, carrier-impurity) during the recombination.

## 2.4 Effective Medium Theory

Effective Medium Theory (EMT) is an approach to approximate the macroscopic optical properties of composite materials. It was used to calculate the dielectric function of nano-/macro-porous silicon (Chapter 4 and 5) and Au/np-Si composites (Chapter 6) in this work. The EMT is derived from the Lorentz local field relation, which considers the local electric field experienced by a dielectric particle. This is different from the macroscopic (external) field due to the presence of particle surface charges. As shown in Figure 2.7, an external electric field causes the redistribution of charges near and on the particle's surface, and new fields arise. Inside the particle, the field $E_s$ has the same direction as the external field, pointing from positive to negative charges on the surface. While outside the particle, the field direction is opposite to the external field, which is called the depolarisation field $E_d$. Therefore, the local field around the particle can be described as[73]:

$$E_{local} = E_0 + E_d + E_s + E_{near}, \tag{2.31}$$

where $E_0$ is the external field and $E_{near}$ is the field generated by nearby particles. For isotropic materials, the contribution from nearby particles is zero due to the symmetry. The depolarisation field caused by surface charge can be calculated by the charge density $E_d = -\frac{\rho}{\epsilon_0} = -\frac{P}{\epsilon_0}$ (surface charge density equals the polarisation density). Therefore, $E_0 + E_d = E_0 - \frac{P}{\epsilon_0} = E$, $E$ is the macroscopic field. The local field is then connected to the macroscopic field as:

$$E_{local} = E + E_s, \tag{2.32}$$

The relation between spherical polarisation field $E_s$ and surface charge density is calculated through slicing the sphere into annular ring with the axis in the same direction as the polarisation[75]. The charge in the ring with width $Rd\theta$ can be calculated which is $dq = (-Pcos\theta)(2\pi Rsin\theta)Rd\theta$ and the induced electric field is $dE = \frac{dqcos\theta}{4\pi\epsilon R^2}$, where $R$ is

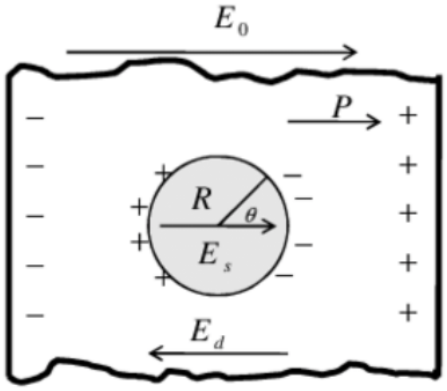


Figure 2.7: Charge distribution and local field around a spherical particle[74].

the radius of the particle. The total charge on the sphere surface is the integration of $q$ over $\theta$ from 0 to $\pi$. The total electric field can then be calculated:

$$E_s = \rho \int_0^{2\pi} \frac{(-Pcos^2\theta)(2\pi R^2 sin\theta)d\theta}{4\pi\epsilon R^2} = \frac{P}{3\epsilon_0} \tag{2.33}$$

Therefore, the final relation between local and macroscopic field $E_{local} = E + \frac{P}{3\epsilon_0}$ is obtained. Assuming there are $N$ particles in the material, each with polarisability $\alpha$. The polarisation caused by local field on each particle can be represented by $p = \alpha E_{local}$. Hence, the total polarisation of the material is $P = \sum_j N_j p_j = \sum_j N_j \alpha_j E_{local} = \sum_j N_j \alpha_j (E + \frac{P}{3\epsilon_0})$. By rearranging this equation, the effective dielectric function of the material can be calculated through $\epsilon = \frac{P}{\epsilon_0 E}$. Arranging the total polarisation gives the relation $\frac{\epsilon - 1}{\epsilon + 2} = \frac{\sum_j N_j \alpha_j}{3\epsilon_0} = \frac{1}{3V\epsilon_0}\alpha$ with $V$ the volume of unit cell. This is relation is called the Clausius-Mossotti relation[76].

The polarisability of a dielectric sphere is $\alpha = 4\pi R^3 \epsilon_0 \frac{\epsilon_i - 1}{\epsilon_i + 2}$ with the dielectric function $\epsilon_i$ of the spherical inclusion. Therefore the relation between effective and inclusion dielectric function is:

$$\frac{\epsilon_{eff} - 1}{\epsilon_{eff} + 2} = \frac{4\pi R^3 \epsilon_0}{3V\epsilon_0} \frac{\epsilon_i - 1}{\epsilon_i + 2} = f \frac{\epsilon_i - 1}{\epsilon_i + 2}, \tag{2.34}$$

with $f$ the volume fraction of the inclusion. Eq.2.34 is known as the Maxwell-Garnett Mixing Rule (MGMR). It is extensively used to obtain the effective dielectric function of

the composite materials investigated in the following Chapters of this work.

Note that Eq.2.34 is derived for inclusions in a vacuum. For the inclusions embedded in other materials, MGMR has the form of

$$\frac{\epsilon_{eff} - \epsilon_m}{\epsilon_{eff} + 2\epsilon_m} = f\frac{\epsilon_i - \epsilon_m}{\epsilon_i + 2\epsilon_m}, \tag{2.35}$$

where $\epsilon_m$ is the dielectric function of the environment.

The MGMR can also be generalised for n-dimensional inclusions[77]:

$$\frac{\epsilon_{eff} - \epsilon_m}{\epsilon_{eff} + (n-1)\epsilon_m} = f\frac{\epsilon_i - \epsilon_m}{\epsilon_i + (n-1)\epsilon_m}. \tag{2.36}$$

For the porous silicon studied in this work, the silicon skeletons were treated as 2D inclusions since their columnar shape. Therefore, the 2D MGMR was employed in the optical model.

# Chapter Three

# Femtosecond Laser System and Experimental Approaches

Optical methods of characterisation and analysis have the advantage of non-contact, non-destructive, time-saving and high accuracy compared to electronic and mechanical counterparts. Therefore, they are widely used to investigate and characterise various types of materials. For example, by measuring the transmittance and reflectance of a material, one can work out its complex permittivity, estimate the conductivity, absorption coefficient[78] and determine the band-gap energy[79]. More complicated techniques, such as ellipsometry and Raman Spectroscopy, further extend the capabilities of transmission and reflection measurements to investigate the optical properties of complex structured materials (such as multi-layers) or chemical/biological interactions. In addition, the material properties in the excited state and the carrier dynamics can be evaluated by promoting electron transitions from lower to higher energy states and probe the temporal change of transmittance and reflectance[80]. Due to the short lifetime of these processes, ultrafast lasers with pulse duration shorter than the state evolution are required.

The ultrafast pump-probe technique was employed to study the carrier dynamics

of semiconducting materials in this work. The core experimental set-up is a femtosecond laser system (Coherent Ltd), which consists of 3 main parts: a Mode-locked seed laser 'Micra' with 800 nm central wavelength (CWL) and 100 nm full-width at half-maximum (FWHM, corresponds to a 10-fs transform-limited pulse); a Q-switch amplifier 'Regen' which amplifies the seed beam from 450 mW to 3 W intense laser pulses with 60 fs pulse duration without changing its wavelength; an Optical Parametric Amplifier (OPA) 'Opera' converts the 'Regen' pulse to output with tunable wavelengths, covering the spectral range between 250 nm and 10 μm. In Section 3.1, the two core techniques, mode-locking and Q-switching, used in 'Micra' and 'Regen' to generate ultrashort pulses, are introduced in detail. In addition, the working principle of OPA using optical nonlinearity is explained. Its ability to generate pulses in a broad wavelength range makes the time-resolved spectroscopy measurements possible. Section 3.2 discusses the experimental approaches involved in this work, including time-resolved pump-probe set-up, VIS-NIR spectrometer and Surface Enhanced Raman Spectroscopy. Section 3.3 focuses on the sample preparation methods of nano- and macro-porous silicon and the set-up for impregnation of gold (Au) nanoparticle impregnation into porous silicon. The optical properties of these materials are presented in Chapters 4, 5 and 6.

## 3.1 Core Techniques of the Femtosecond Laser System

Mode Locking and Q-switching are the two standard techniques to produce laser pulses with extremely short duration[81]. The main difference between these two methods is that the pulses delivered by a mode-locked laser have lower power and higher repetition rate than Q-switching technology. Therefore, a mode-locked laser is commonly used as a seed laser in a femtosecond laser system, followed by a Q-switched cavity to amplify the pulse power.

### 3.1.1 Mode-Locking

The frequencies of photons in a laser pulse are not identical. Instead, they show a Gaussian-like distribution in the spectrum. The bandwidth and central wavelength of a laser are determined primarily by the material of its gain medium[82]. Titanium-doped sapphire (Ti: sapphire) crystal which can generate 800 nm wavelength pulse with $\sim$ 200 nm FWHM was used as the gain medium of 'Micra' and 'Regen' in this work[83]. Figure 3.1 briefly illustrates the principle of a mode-locked laser. The frequency envelope in Figure 3.1(a) is the luminescence spectrum of a gain medium. The discrete line under the envelope is the frequencies that fulfil the standing wave condition of the cavity $f = cq/2L$, with $c$ the speed of light, $L$ the cavity length and $q$ the mode order. The interference of standing waves with different frequencies resulting in the discrete wave packets in the time domain with short pulse duration as shown in Figure 3.1(b). Unlike other resonators, a mode-locked laser has a single-mode output due to the mode competition inside the cavity. That is, different modes experience different amplification in the same gain medium. The one with the highest gain factor suppresses other modes and reaches the stable gain saturation state[84].

### 3.1.2 Q-switching

Q-switching is obtained by trapping a laser pulse inside a cavity for several rounds to achieve multi-stage amplification and outputting a high peak power pulse at the gain saturation stage. Generally, Q switching technique can be classified into two types:

(1) Active Q-switch: An external output trigger, such as a mechanical shutter, electro-optical modulator or acusto-optical modulator, is used to trigger laser pulse. In this work, a pair of pockel cells were employed to trap and output pulses by changing

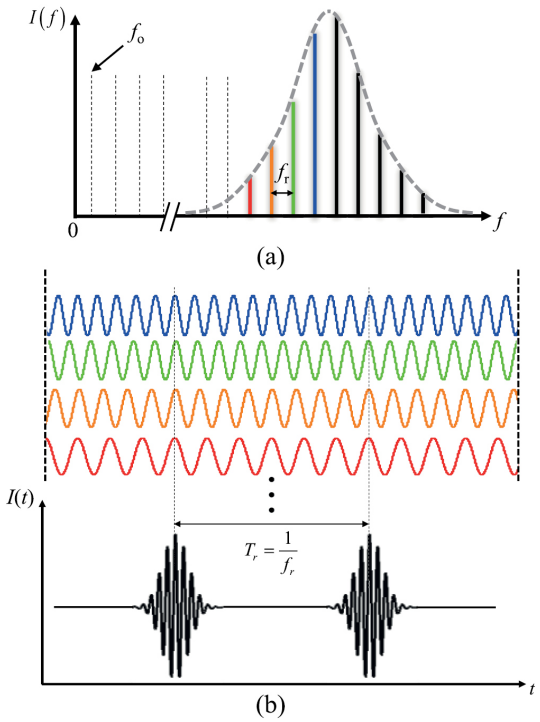


Figure 3.1: Laser modes in the frequency (a) and time (b) domains[85].

the polarisation of the beam inside the Q-switch cavity. As shown in Figure 3.2, the s-polarised seed beam is coupled to the Q-switch cavity by mirror RM7. It passes through the quarter-wave plate RWP twice, resulting in a polarisation change from s to p and leaves the cavity after one round trip by reflecting off the output coupler RP. When the first pockel cell (PC1) is switched on, it alters the polarisation of the pulse as a quarter-wave plate, thereby cancelling the polarization change caused by the RWP. The beam remains s-polarised and is trapped inside the cavity. It experiences multiple amplifications until the second pockel cell (PC2) is triggered. The s-polarised light then turns to p-polarised and leaves the cavity[86].

(2) Passive Q-switch: A saturable absorber (such as Cr: YAG) is used as the output trigger. Initially, the absorber is not transmissive. The pulse is trapped in the cavity and amplified every time it passes through the gain medium. After several round trips, the pulse intensity is sufficient to saturate the absorber, resulting in a significant decrease in

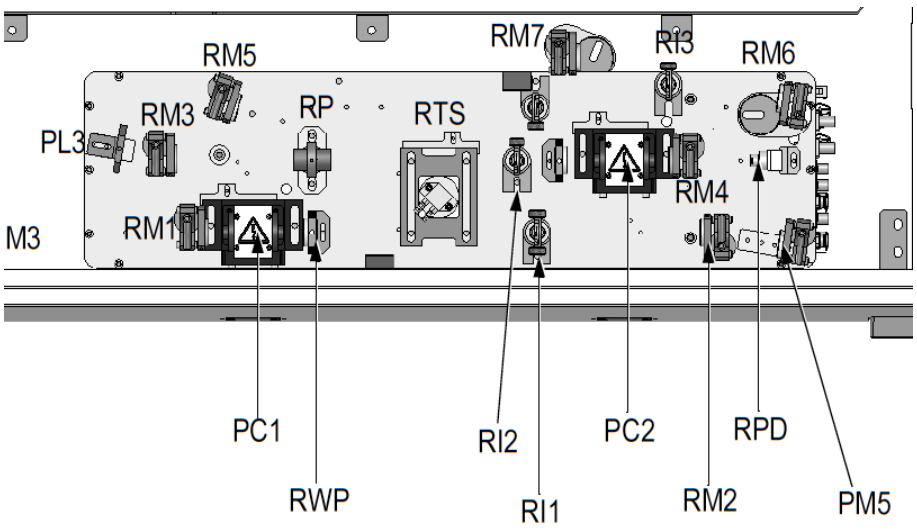


Figure 3.2: An illustration of the active Q-switch cavity. RTS represents the Ti-sapphire crystal (gain medium); four mirrors (RM1-4) form the amplification cavity; RWP is a quarter-wave plate, PC1-2 are pockel cells; RP is an output coupler; mirrors RM5-7 are used to direct the amplified beam to exit; RPD is a fast diode for monitoring the build-up trace of the seed beam[87].

absorption and an increase in transmission. The high-power pulse then passes through the absorber and leaves the cavity. After that, due to the low intensity level in the cavity, the absorber returns to a high absorption state[88].

### 3.1.3 Optical Parametric Amplifier

An optical parametric amplifier (OPA) is a passive laser device that converts a monochromatic input into an output laser with tunable wavelength. Several nonlinear crystals are used in OPA to alter the wavelength through Super-Continuum Generation, Parametric Amplification and Difference Frequency Generation processes[89].

More specifically, OPA includes three stages to generate variable wavelength output.

In the first stage, the monochromatic input is split into two beams. 10% of it is guided to a Sapphire plate for the continuum white light generation (seed beam). The rest of it is directly guided to the second and third amplification stages (pump beam). The generation of white light is a result of self-phase modulation inside the crystal. Nonlinear optical Kerr-effect occurs when the pulse travels through the Sapphire plate, which causes the material refractive index to vary with pulse intensity profile. This variation induces a phase change $d\Phi$ in time which is equivalent to the spectrum modification ($\Delta\omega = \frac{d\Phi}{dt}$).

After the sapphire plate, a dispersive plate is used to stretch the pulse with different frequency components in time. In the second nonlinear stage, the pump amplifies the seed beam through the OPA process, as shown in Figure 3.3. The desired wavelength of the seed beam is selected at this stage by controlling the arrival time difference between the seed and the pump on the nonlinear crystal. The angle of a nonlinear crystal (Beta barium borate, BBO) is adjusted to satisfy the phase-matching condition of the pump and signal pulses. The third amplification stage also utilises the OPA, where the signal beam is further amplified by pump, and another beam (Idler) with frequency $\omega_{idler} = \omega_{pump} - \omega_{signal}$ emerges. The frequency of the idler beam can be adjusted by tuning the frequency of the signal beam. However, the actual case is more complicated. Due to the high intensity of the pump beam, other nonlinear processes, such as fourth harmonic generation, may occur in nonlinear crystals, resulting in multi-wavelength output. Therefore, dichroic mirrors are employed to separate output beams with different wavelengths and guide them to different optical paths according to experimental needs.

For the OPA used in this work, the signal's wavelength is in the tunable range between 1.2 and 1.4 μm, while the idler beam varies between 1.8 and 2.5 μm. The idler beam was used as the probe for the experimental results in Chapters 5 and 6. In Chapter 4, Mid-Wavelength Infrared (MWIR) probe was used. The MWIR beam was generated by adding another nonlinear crystal, Silver Thiogallate (AGS), to the OPA as the fourth

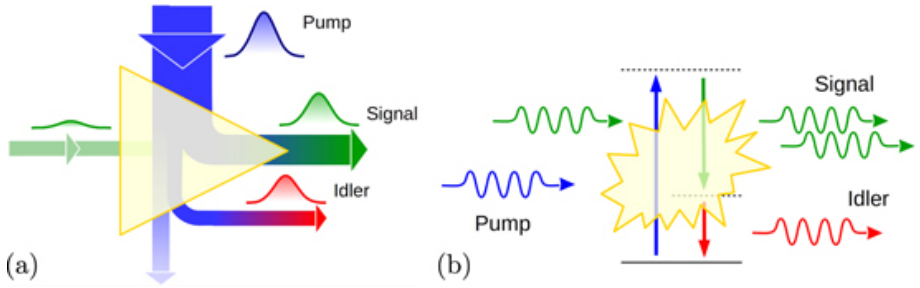


Figure 3.3: An illustration of the OPA process (a) and the energy level diagram (b)[90].

stage. The signal and idler beams were directed to the AGS and overlapped both in time and space on the crystal surface. The mixing of the signal and idler beam leads to the Difference Frequency Generation (DFG) nonlinear process, as shown in Figure 3.4.

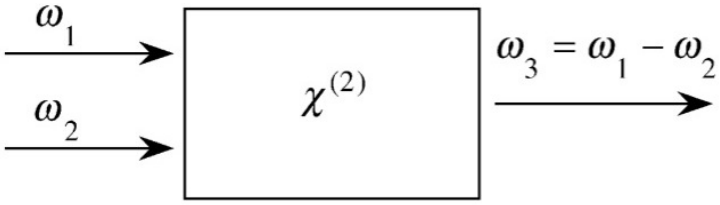


Figure 3.4: Generation of Middle Infrared beam with DFG process.

Figure 3.5 illustrates the relation between the output wavelength and the input signal/idler wavelength of the DFG process. For example, to generate the 4 μm MWIR beam used in Chapter 4, the signal and idler wavelengths need to be adjusted to 1.3 μm and 2 μm, respectively. The phase-matching condition are satisfied by tilting the AGS crystal to 110° relative to the incoming beam. In general, the DFG process has around 5% efficiency, indicating that the average power of signal and idler needs to exceed 100 mW to obtain a detectable MWIR. In addition, the nonlinear process not only amplifies the signal but also the noise. The noise level increases with the number of nonlinear stages in OPA. Therefore, due to the low signal-to-noise ratio (SNR), the MWIR experiments are more complex than the Short-Wavelength Infrared (SWIR) ones.

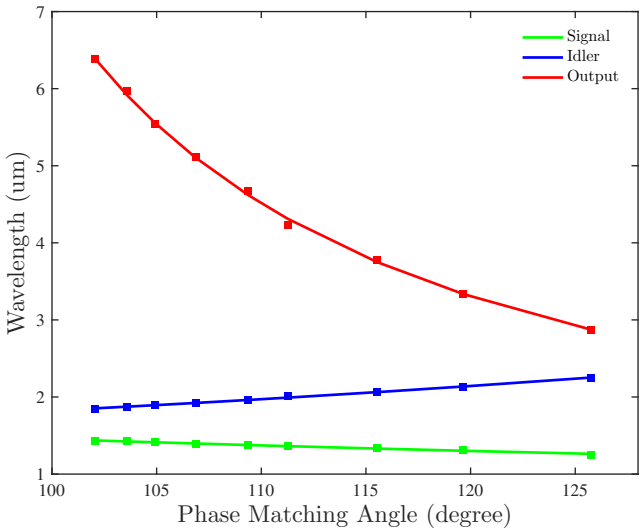


Figure 3.5: The wavelength relation between the Signal, Idler and MWIR output.

## 3.2 Experimental Methods

### 3.2.1 Time-Resolved Pump Probe Technique

The Pump-probe technique has been employed in this work to investigate the carrier dynamics with femtosecond resolution. The sketch of the experimental set-up is shown in Figure 3.6. A sample is optically excited by an intense pump pulse with fluence in the range between 1 and 10 mJ/cm$^2$. Another weak pulse (0.1-0.3 mJ/cm$^2$) is used to probe the optical response of the sample in the excited states. By varying the arrival time difference at the sample surface between the pump and probe pulses, the evolution of the optical properties of a material can be obtained by measuring its transient change of transmittance and reflectance. A motorised delay stage was used to control the arrival time of the pump and probe pulses. The resolution of the stage is in the micron scale, which corresponds to sub-femtosecond in time, much shorter than the laser pulse duration (60 fs). Therefore, the time resolution of the whole set-up only depends on the pulse duration of the pump and probe pulses.

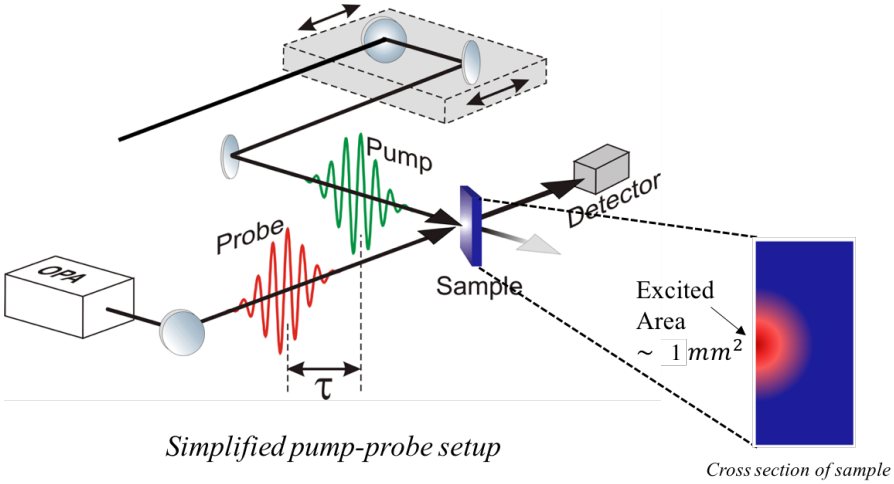


Figure 3.6: A illustration of Pump-Probe Set-up[91].

Before the start of the experiment, the spatial overlap of the pump and probe beams was checked with laser cards and a CCD camera. To avoid influences from the unevenly excited area and the excitation boundaries, the pump beam must be homogeneous and at least twice larger than the probe beam spot. Therefore, two convex lenses with different focal lengths have been used for the pump and probe respectively to control the spot size on the sample surface. For the results demonstrated in Chapters 4, 5 and 6, the pump and probe beam has 1 mm and 500 µm diameter, respectively, on the sample surface. Afterwards, two detectors were used to collect the reflected and transmitted probe signal. For the SWIR signal, polycrystalline lead selenide (PbS) detectors were used, while mercury cadmium telluride (MCT) detectors were employed for MWIR measurements. A two-channel lock-in amplifier (Zurich Instruments) was used to convert the analogue signals collected by the detectors to digital signals. The data was then read out by a LabVIEW program.

In addition, two sets of half-wave plates and linear polariser were placed in the pump and probe optical paths, respectively, in order to control their power and polarisation state. The sample was mounted on a motorised rotational stage with two movable arms

for two detectors to carry out angle dependence measurements. This flexible pump-probe set-up enables the measurements of transient transmittance and reflectance with different pump power, probe power, probe wavelength, pump and probe polarisation, incident angle and detection angle to characterise the material properties with or without excitation.

### 3.2.2 VIS-NIR Spectrometer

A VIS-NIR spectrometer was used to identify the plasmon resonance peak (results in Chapter 6). A broadband unpolarised white light source was used to illuminate the samples, while back-scattered light was collected by a PerkinElmer Lambda 1050 UV/Vis/NIR spectrometer equipped with an integrating sphere. The samples were placed at the back of the sphere, where the light was reflected off the sample and collected by the sphere. Both total and scattered reflections were measured. For the scattered reflection, the specular component was excluded by opening a corresponding aperture on the port, which allowed the specularly reflected light to exit the sphere. The increase of the scattered light intensity at the plasmon resonance can be identified with this method.

The VIS-NIR spectrometer was also used to estimate the band-gap of the samples. In addition to the specular reflection measurement, a transmission measurement is also required to obtain the absorptance $A = 1 - T - R$, with $T$ and $R$ the transmittance and reflectance, for band-gap determination. The transmittance of a sample is evaluated by placing it at the light entrance port of the integrating sphere and collecting the total and scattered transmitted signal at another port. The band-gap is then retrieved using the tauc plot method, where the y-axis of the plot is equal to $\sqrt{\alpha\omega}$, and the x-axis is the photon energy[92], with $\alpha$ being the absorption coefficient calculated from absorptance $A$ of the material. The band-gap of the sample is obtained by extrapolating the linear part of the curve to the abscissa. Figure 3.7 shows an example of employing tauc plots

to determine the band-gap of hydrogenated and oxidised porous silicon with different porosity.

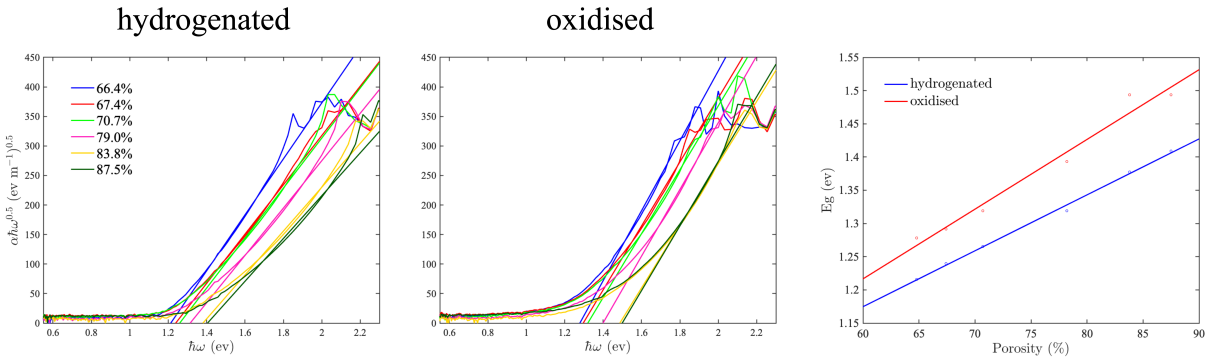


Figure 3.7: Tauc plots used to determine the band-gap of hydrogenated and oxidised porous silicon and the retrieved band-gap as a function of porosity.

### 3.2.3 Raman Spectroscopy

Raman spectroscopy utilises the Raman scattering process to reveal the chemical structure and molecular interactions of materials. Raman scattering is an inelastic scattering accompanied by the change of incident photon energy[93]. During the Raman process, the electrons are excited by the photons to high-energy states and then relaxes through the vibrational states, as shown in Figure 3.8. Therefore, the change in photon energy directly reflects the energy of different vibrational states.

Surface-Enhanced Raman spectroscopy (SERS) utilise the localised electromagnetic fields provided by the substrate to amplify Raman signals[94]. The most common SERS substrate is made of plasmonic materials, such as rough metal surfaces and metallic nanoparticles[95, 96]. In Chapter 6, a novel SERS substrate consisting of Au nanoparticles and np-Si was fabricated and characterised by a Raman spectrometer. The excitation wavelength was chosen to be 808 nm, corresponding to the LSPR wavelength of the Au

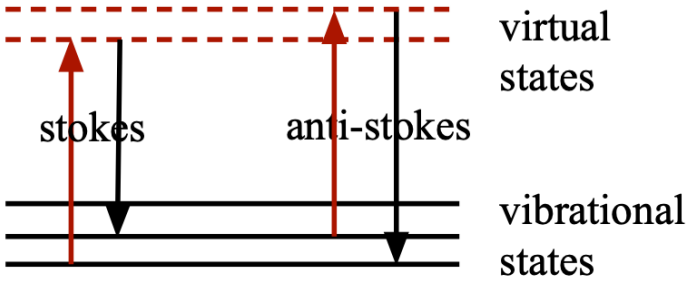


Figure 3.8: Energy diagram of Raman process

clusters in the np-Si matrix. An objective with 40X magnification was used to focus the excitation beam onto the sample. The back-scattered light was collected by the same objective. A beam splitter was used to separate the incoming and reflected light. A notch filter that blocks the 800 nm light was added to the reflected light path to filter out the specularly reflected light. A CCD camera was used to record the Raman spectrum of the probed molecules.

## 3.3 Sample Preparation

### 3.3.1 Nano- and Micro-Porous Silicon

Nano- and micro-porous silicon (np-Si and mp-Si) are the two primary materials investigated in this work. Their optical and electronic properties are very different from their bulk counterparts and can be easily modified by varying the size, shape and arrangement of the porous structure. This flexibility makes porous silicon easier to meet research and industrial requirements for different applications. On the one hand, the advantages of silicon, such as transparency in the infrared region and controllable excited-state optical properties, are conserved. On the other hand, unique properties are introduced owing to

the inner structures, which brings a new aspect to applications in solar cells, opto-electronic modulators and nonlinear optical components[97].

Figure 3.9 shows the top view of np-Si (left) and mp-Si (right) as an example. np-Si is a sponge-like material with disordered nano-pores, while the mp-Si used in this work has regularly oriented micrometer pores. The fabrication technique is different for np-Si and mp-Si — electrochemical etching was employed for disordered np-Si, whereas E-beam lithography was used to generate the ordered pattern of mp-Si.

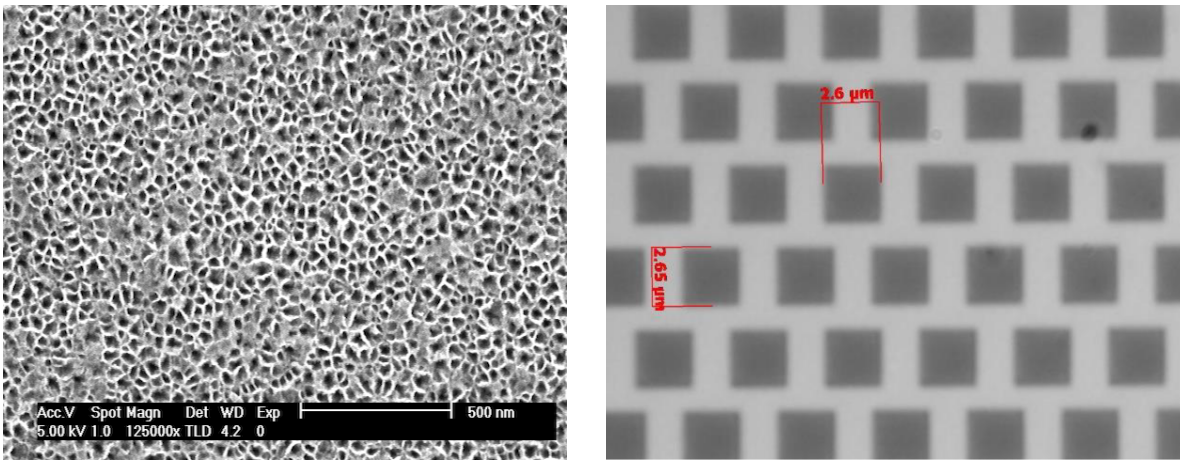


Figure 3.9: Top view of nano-porous silicon (left) and macro-porous silicon (right).

The left diagram in Figure 3.10 shows the electrochemical anodization process of np-Si fabrication. The bulk silicon substrate was immersed into an electrolyte which is a mixture of methanol and 40% Hydrofluoric acid (HF) (ratio 1:1). A DC voltage is then applied between the anode and cathode to accelerate the reaction between HF and silicon. The dissolution of silicon is caused by the replacement of silicon-hydrogen bound by silicon-fluorine bound on the surface[98]. Pores are formed due to the reaction products $SiF_4$ and $H_2SiF_6$ are soluble in the electrolyte. The detailed reactions involved during the np-Si formation are shown in Figure 3.11. By varying the electrolyte concentration and the current density, the porosity can be tuned from 0 to 90%, while the thickness is

controlled by the anodization time. For the sample used in Chapter 6, the 500 nm np-Si layer was etched from 500 µm-thick bulk silicon, and the np-Si layer was not separated from the bulk silicon substrate. Free-standing np-Si membranes were used in Chapter 4. The separation of np-Si from its bulk substrate is realized by applying a short current pulse with the current density of 120 mA/cm$^2$ at the end of the anodization. Under this current density, the pore collapse at the boundary between np-Si and Si results in the partition of the np-Si layer.

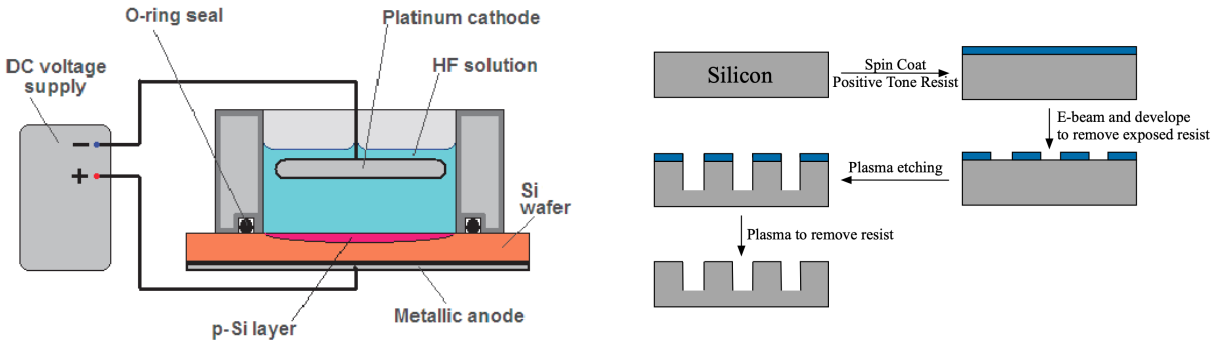


Figure 3.10: Fabrication Processes of np-Si(left)[99] and mp-Si (right)[100].

The right plot of Figure 3.10 illustrates a flow diagram of the mp-Si production process with E-beam lithography. The bulk silicon substrate is first covered by a layer of polymethyl methacrylate) (PMMA) resist, and then exposed to the electron beam for pattern generation. The resist at the exposed area is then washed out by developer. Afterwards, the sulfur hexafluoride (SF6) plasma is applied to etch out the silicon in the unprotected area, and Fluoroform (CHF3) plasma is employed to remove the residual resist[101].

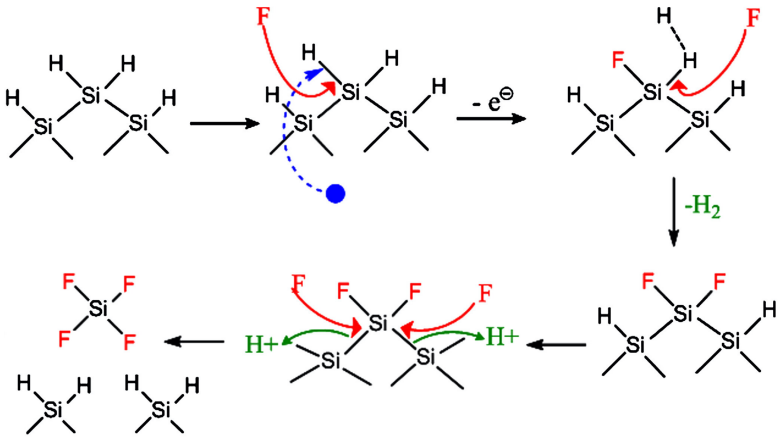


$$Si_{(s)} + 2HF_{(aq)} \rightarrow SiF_{2\,(s)} + H_{2\,(g)}$$

$$2SiF_{2\,(s)} \rightarrow Si_{(amorphous)} + SiF_{4\,(aq)}$$

$$SiF_{4\,(aq)} + 2HF_{(aq)} \rightarrow H_2SiF_{6\,(aq)}$$

Figure 3.11: An illustration of the silicon dissolution process and the reaction equations involved in the formation of np-Si[102, 103].

### 3.3.2 Gold Nanoparticle Impregnation

The optical properties of composite material consist of np-Si and Au nanoparticles were investigated in Chapter 6. The electroless immersion plating technique was employed to impregnate Au nanoparticles into the pores of np-Si. Tetrachloroauric acid (9.85 mg, $HAuCl_4$) was dissolved in ethanol (50 ml) and used as the plating solution. When np-Si was immersed in the solution, Au was spontaneously reduced from its compound by the hydrogen termination at the pore interface and form Au nanoparticles: $[AuCl_4]^- + 3e^- \xrightarrow{H^+} Au + 4Cl^-$. The np-Si samples need to be freshly made to avoid the growth of oxide at the pore interface because the oxygen-terminated np-Si does not react with $HAuCl_4$. Alternatively, 2% of HF can be used to pre-treat (30 seconds) the np-Si sample to replace

the oxygen- with hydrogen-termination. During the immersion process, an ultrasonic bath was employed to remove air bubbles in the np-Si channel and stimulate the solution to flow into the pores. The immersion time and temperature need to be controlled during this process to regulate the Au nanoparticle size. After the immersion plating, the sample was dipped in ethanol to remove the residual plating solution, and the sample was dried in a fume cupboard purged with nitrogen gas.

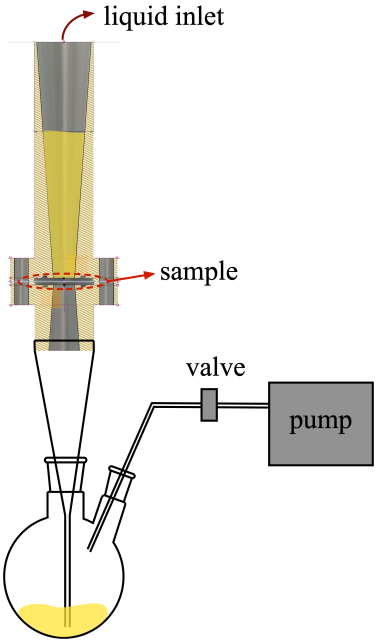


Figure 3.12: Au impregnation set-up.

Due to the fast reduction rate of Au nanoparticles on the np-Si surface and slow liquid diffusion rate of np-Si[35], the Au tend to clutter on the pore tips instead of distributing evenly in the depth of np-Si. Therefore, the ultrasonication method is only suitable for np-Si thin layers with thickness less than 1 μm. Another impregnation method was developed to resolve this obstacle by applying a pressure difference between the two sides of a sample and forcing the plating solution to flow through. Figure 3.12 shows the sketch of the setup. A sample is clamped by two tubes that one side of it is connected to

a rotary pump. The other side of the tube is filled with the plating solution. The solution is forced through the sample when the pump is switched on. By regulating the pressure applied by the pump, the flow rate of the plating solution can be controlled. The optimum condition is reached when the flow rate equals the reduction rate of Au. With this method, the Au nanoparticles with a radius less than 50 nm were successfully embedded in np-Si with a thickness of more than tens of microns.

# Chapter Four

# Carrier Dynamics and Surface Vibration-Assisted Auger Recombination in Nano-Porous Silicon

**This chapter is a reformatted version of my paper 'Carrier dynamics and surface vibration-assisted Auger recombination in porous silicon', A. Zakar, R. Wu, D. Chekulaev, V. Zerova, W. He, L. Canham, and A. Kaplan, Phys. Rev. B 97, 155203 (2018).**

The main motivation of this Chapter is to investigate the excited charge carrier dynamics of nano-porous silicon (np-si) using Medium Wavelength Infrared (MWIR) light covering the range between 3.4 and 5 μm. This method allows probing the carrier density in the range of $10^{17}$—$10^{21}$ $cm^{-3}$ following the excitation by a few tens of femtoseconds optical pump pulse having the above band-gap photon energy of 1.5 eV.

It has been reported previously that both quantum confinement and surface chemistry influence np-Si carrier dynamics[38]. The confinement effects in a nano-scale regime induce different decay mechanisms of the excited carrier from the bulk counterpart. For

example, phonon bottleneck effect was proposed to interfere with relaxation and decay dynamics[104, 105, 106]. As well, the reduction of np-Si internal structure size also causes an increase, not only in the band-gap, but also in the surface-to-volume ratio. This can induce a strong coupling of the carrier to the surface states affecting the recombination and scattering channels, as well as opens new pathways by the confinement and coupling to the surface states. In particular, the surface composition can play an important role in the initial energy relaxation of the photo-excited electrons [107, 108, 109, 110]. Due to the large internal surface of np-Si (1000 $m^2/cm^3$[111]), the np-Si surface contains an enormous quantity of impurities from the electrochemical etching and the surrounding environment. The native impurity such as hydrogen is introduced in np-Si production process, while oxygen as a non-original impurity is adsorbed in a few minutes after drying in air[38]. The surface defects therefore form stable energy states which interacts with the carrier and affects its transport and recombination. This works demonstrates that, by use of MWIR probe tuned to the frequencies overlapping with the IR-active vibrational modes of the surface impurities, the influence of these states on the carrier dynamics can be quantified and discriminated from other phenomena.

This Chapter is organised in the following way. Section 4.1 shows the main experimental particulars. The details of the sample's fabrication method and their characteristic dimensions as observed by Scanning Electron Microscope (SEM) and other methods are described. The experimental setup based on the MWIR probe - near IR pump spectroscopy are also presented. Section 4.2 is devoted to the experimental findings, analytical and numerical models used for the data analysis along with discussions of the physical mechanisms pertinent to the results. In Section 4.2.1, the probe interaction with the optically pumped samples is linear are confirmed. In Section 4.2.2, the time-resolved pump-probe results of the transmittance and reflectance change at four probe wavelength of 3.5, 4, 4.5 and 5 μm as a function of the pump fluence are presented. Furthermore,

the wavelength-resolved pump-probe transmittance change at the fixed pump fluence are shown. Section 4.2.3 presents an optical model based on the 2D Maxwell-Garnett mixing formula, modified to incorporate the contribution of optically-pumped free carriers, using the Drude model. The WKB model is used to account for the effect of the dielectric function non-uniformity. Section 4.2.4 investigates the absorption of the injected free carriers in the MWIR range. Section 4.2.5 derives the governing mechanisms of the dynamics and recombination of the free carriers from the experimental data. Section 4.2.6 correlates the recombination mechanism and vibrational modes of the surface molecular impurities active at various wavelength of MWIR spectrum.

## 4.1 Experimental Details

### 4.1.1 Np-Si Samples Fabrication

The np-Si membranes described in this Chapter were prepared using electrochemical anodisation as introduced in Chapter 3. Boron doped Si (100) wafer was used as the substrate (5-15 mΩcm, corresponding to the dopant density of 1—$3\times10^{18}$ 1/cm$^3$). The membranes were stored in air, and the passivation at ambient conditions results in the presence of the dangling oxides', hydroxides' and silanes' molecular bonds on the surface of the pores. More details are covered in the Handbook of Porous Silicon, chapters by M.J.Sailor and Y.H.Ogata[35]. A porosity of 71% was measured using gravimetric analysis and the thickness of 111 μm was estimated from the images of the cross-section obtained by SEM. Representative SEM images, showing the top and side views of the pores structures respectively, can be seen in Figure 4.1. The structure of the obtained samples can be described as a sponge-like silicon material consisting of interwoven wires with mean diameter of about 10 nm. The samples used in this study are different from those usually

employed to investigate photoluminescence in np-Si, as p-silicon substrates are generally better suited to this purpose[112]. Instead, the main focus here is to obtain relatively thick and optically uniform membranes for which p+ substrates are a better choice[113]. A well-founded model, describing the optical response, is needed to achieve the main goal of investigating the change of dielectric function induced by an external perturbation of optical excitation; and the optical uniformity of the membranes is helpful in avoiding additional parameters in the theoretical calculations. It was verified separately that the samples do not demonstrate any detectable photoluminescence when illuminated with 517 and 800 nm lasers. Therefore, the results of the carrier dynamics investigation reported here solely relate to the non-radiative processes. The membranes are semi-transparent for the MWIR probe range, allowing simultaneous measurements of the reflectance and transmittance. This is an important advantage over using thin films on a substrate, which might introduce unwanted optical response from an interface and a supporting substrate for both the pump and probe, complicating the development of an optical model and skewing the interpretation.

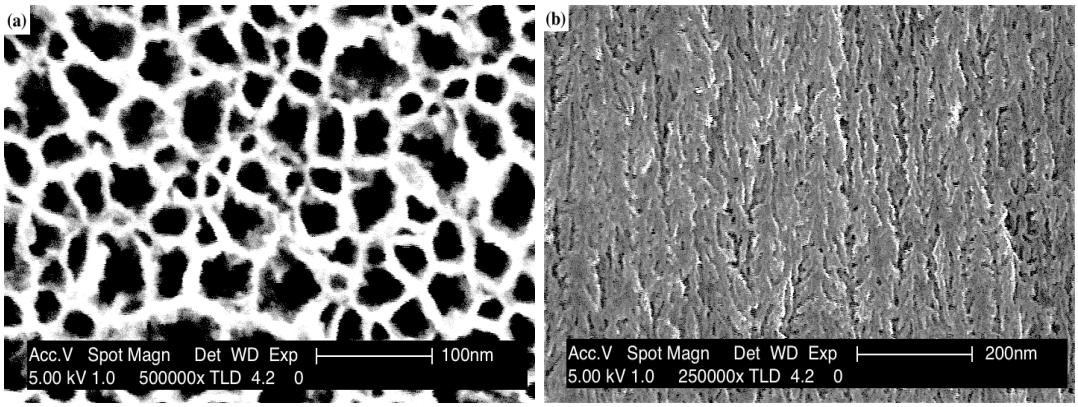


Figure 4.1: SEM images of the np-Si membrane used in this chapter, showing (a) the surface of the sample and (b) the cross-section of the sample.

### 4.1.2 Ultrafast MWIR Pump-Probe Setup

The majority of the measurements in this Chapter were investigated using a femtosecond pump-probe technique. The set-up is based on a Coherent ultrafast laser system as introduced in Chapter 3. A beam splitter was used to split the laser output from 'Regen' into two beams. The smaller fraction of the beam (about 5%) was used as the pump beam to excite the free charge carriers in the np-Si membranes. The remnant of the beam was guided into an optical parametric amplifier (OPA) to generate a probe beam, tunable in the range between 3.4 and 5 μm. According to the manufacturer specification, the OPA generates pulses with the spectral width of about 200 nm around a central wavelength, corresponds to $\sim$ 100-fs transform-limited pulses. The incident angle of the $p$-polarised pump was set to 60°, with the purpose of achieving a stronger absorption near the Brewster angle and reduce any unwanted reflection. The angle of incidence for the probe beam was near 20° and it was set to have $s-$polarisation. More detailed information about the experimental setup can be found in Chapter 3.

The majority of the raw pump-probe experimental results are presented as change of the transmittance, $\frac{\Delta T}{T_0}(\Delta t) = \frac{T_e(\Delta t) - T_0}{T_0}$, and, reflectance, $\frac{\Delta R}{R_0}(\Delta t) = \frac{R_e(\Delta t) - R_0}{R_0}$, where $T_0$ and $R_0$ are the unexcited sample transmittance and reflectance, respectively. $T_0$ and $R_0$ were measured by using pump-probe set-up and fourier-transform infrared spectrometer (FTIR). The $T_e(\Delta t)$ and $R_e(\Delta t)$ are the transient transmittance and reflectance of the excited sample as a function of the pump-probe delay time, $\Delta t$.

A Bruker FTIR Hyperion microscope was used for the FTIR measurements. The main reason to use FTIR is to provide high resolution for the identification of the vibrational modes of surface adsorbates and impurities in the samples. It was confirmed that the FTIR and pump-probe measurements quantitatively agree with each other, although the pump-probe set-up does not have high spectral resolution and tends to smear sharp

features in the spectra[40].

## 4.2 Experimental Results, Analysis and Discussion

### 4.2.1 Probe Fluence Dependence

Before presenting the main bulk of the results and data analysis, a series of measurements needed to be completed to demonstrate that the probe beam traversing through the optically excited samples does not change their optical properties. That is, the interaction of the probe with the medium can be described using linear optical models and a complexity involved in the non-linear analysis, which includes the dependence on the probe intensity, can be avoided. The measurements have been carried out because it is extremely difficult to generate and detect weak low-noise signals in this range of wavelength and it was necessary to push the probe intensity to a higher level than it is normally used for the visible or near-infrared wavelength. Another concern was that the absorption of the probe beam might increase the temperature of the samples and affect their optical properties in an unpredictable way.

The measurements were conducted by the simultaneous recording of the transmitted and reflected fluence of the incoming probe beam covering the range between 0.3 and 2.5 mJ/cm$^2$. The pump fluence was fixed at 4 mJ/cm$^2$. Figure 4.2(a) and (b) show the representative data of the measured transmitted, $F_t$, and reflected, $F_r$, probe fluence, respectively. The wavelength of the probe was set to 4 μm and the experiment repeated at several probe fluences as a function of delay time, $\Delta t$. Figure 4.2(c) shows the transmittance, $T$, and reflectance, $R$, evaluated from the data shown at Figure 4.2(a)-(b) by calculating the ratios between the transmitted, reflected and incoming probe fluences at near-zero

delay times, $\Delta t \sim 0$, where the signal's change is at its maximum. Figure 4.2(c) also shows absorptance, $A$, which is connected with $R$ and $T$ by the relationship $R + T + A = 1$. It can be seen that $R$, $T$ and $A$ are nearly flat and the shape of the decay curves shown in Figure 4.2(a) and (b) is unchanged as a function of the probe fluence, indicating that its interaction with the samples is predominantly linear and the probe is not affecting the optical properties of the samples through an absorption process.

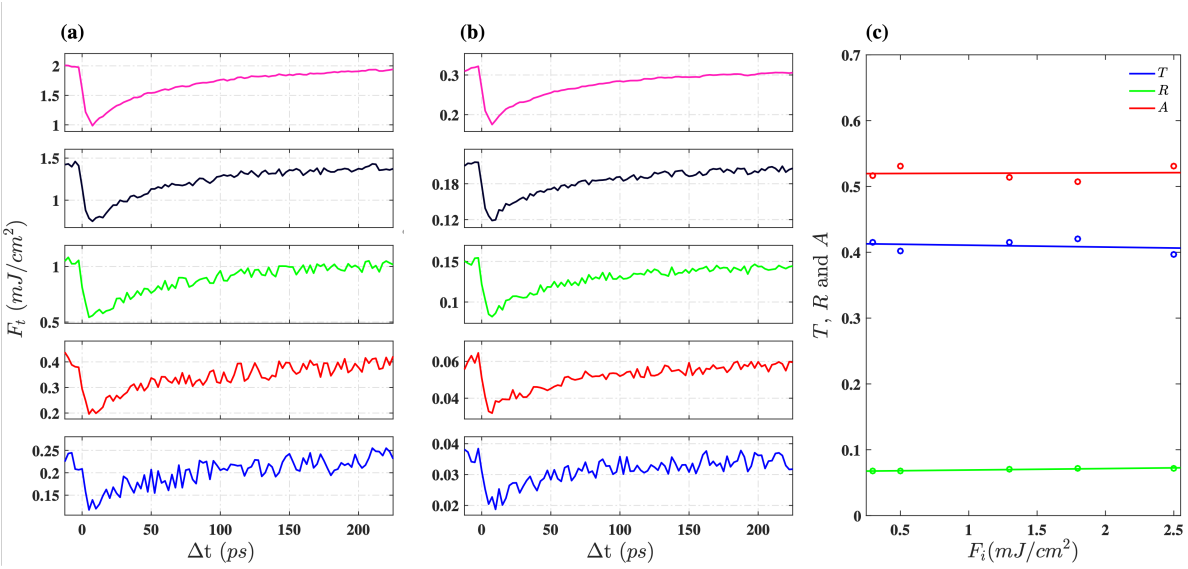


Figure 4.2: (a) Transient transmitted, $F_t$, and (b) reflected, $F_r$, fluence of the 4 μm probe recorded for different incoming probe fluences, $F_i$, at the fixed pump fluence of 4 mJ/cm$^2$. $\Delta t$ is the delay time between the pump and probe. (c) Transmittance, $T$, reflectance, $R$, and absorptance, $A$, as a function of $F_i$, evaluated from the measurements shown at 2 (a) and (b) at around zero delay time, $\Delta t \sim 0$, corresponding to the maximum change of $F_t$ and $F_r$.

It is also useful to note that pumping of the samples with the 4 mJ/cm$^2$, 800 nm pump increased the absorptance of the unpumped samples from 7% to 52% at nearly zero delay, in line with previously published findings[40, 29]. It was shown that the probe effective absorption coefficient extracted from those measurements is around 74 cm$^{-1}$

which was demonstrated to be mainly as a result of the interaction with the excited free carriers at the probe wavelength of 4 μm (free carriers absorption)[40] and confirmed again on another set of separate measurements presented in this work.

### 4.2.2 Time Resolved Measurements of Transmittance and Reflectance Change

To investigate the transient MWIR response of the optically excited np-Si and to gain insight into the nature of the excited carrier relaxation and dynamics, a comprehensive set of experiments simultaneously measuring the time-resolved $\frac{\Delta T}{T_0}(\Delta t)$ and $\frac{\Delta R}{R_0}(\Delta t)$ for the four different probe wavelengths of 3.5, 4, 4.5 and 5 μm were performed. The results are shown in Figure 4.3 where each decay curve corresponds to a different pump fluence ranging between 0.4 and 4.8 mJ/cm$^2$, while the probe fluence for each wavelength was kept slightly below 1 mJ/cm$^2$. The measurements revealed that there is a noticeable difference between the maximum change of the reflectance and transmittance of the samples excited at the same pumping conditions but probed with different wavelengths. For example, the maximum transmittance change for the probe wavelength of 3.5 μm is about 0.7; while for 4 μm it drops to 0.55 and increases again to 0.82 at 5 μm. A similar observation can be made about the reflectance change and the shape of the decay curves, which appear to be wavelength dependant.

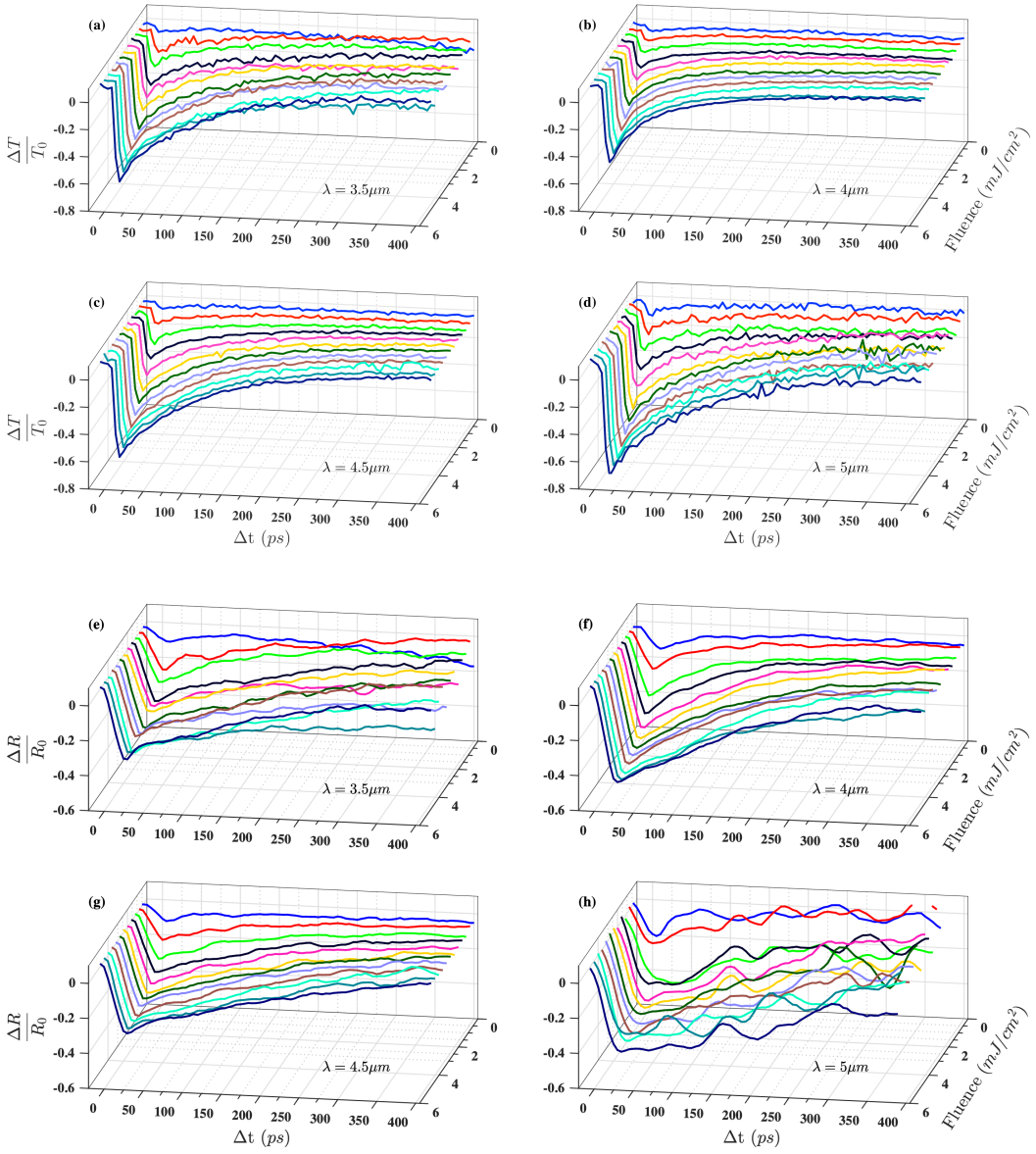


Figure 4.3: (a)-(d) and (e)-(h) are time resolved transmittance, $\frac{\Delta T}{T_0}$, and reflectance change, $\frac{\Delta R}{R_0}$, respectively as a function of the delay time, $\Delta t$, between the pump and probe measured for different pump fluences covering the range between 0.4 and 4.8 mJ/cm$^2$ using 3.5, 4, 4.5 and 5 μm probe wavelength.

The effect of the decay curve dependance on the probe wavelength can be observed

in greater detail in Figure 4.4 which displays a 2D colour map of $\frac{\Delta T}{T_0}(\lambda, \Delta t)$ obtained at the fixed pump fluence of 4 mJ/cm$^2$ as the probe wavelength was scanned with a high resolution. It can be seen that the decay rate is neither uniform nor changes monotonically as a function of the probe wavelength. The main point of this Chapter is to use the data accumulated in the time-resolved experiments for understanding and quantifying the excited carrier's contribution to the change of optical properties, as well as the relaxation and decay mechanisms. For this purpose, an elaborate procedure was developed which uses the data of $\frac{\Delta T}{T_0}(\lambda, \Delta t)$ and $\frac{\Delta R}{R_0}(\lambda, \Delta t)$ to extract the information about the decay channels of the carrier concentration, $N$, and their interaction with the probe beam and medium.

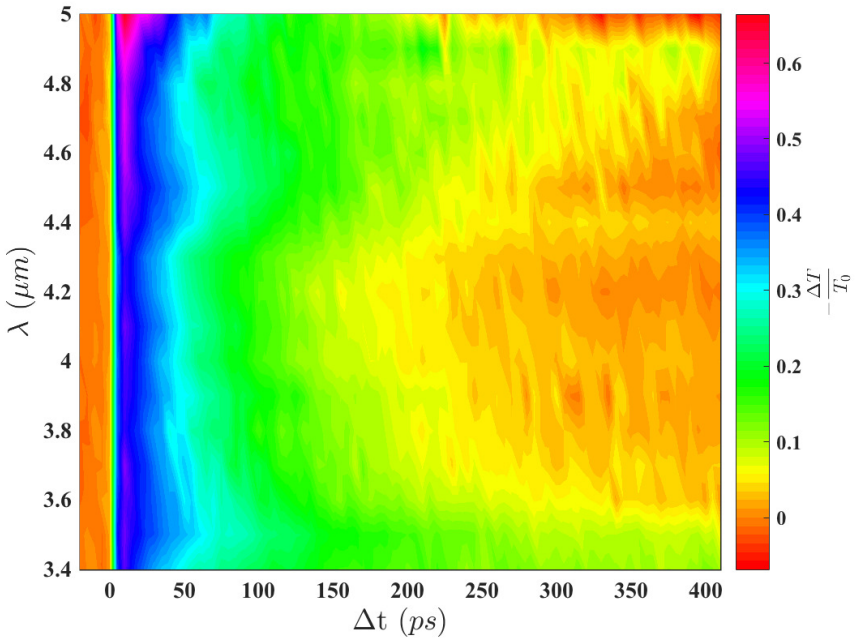


Figure 4.4: 2D colour map of time resolved transmittance change for different wavelength, $\frac{\Delta T}{T_0}(\lambda, t)$, at the fixed pump fluence of 4 mJ/cm$^2$. $\Delta t$ is the delay time between the pump and probe.

### 4.2.3 Optical Model

The main goal of the optical model is to retrieve the carrier density decay curves from the transient measurements of the reflectance and transmittance. np-Si was considered as a homogeneously mixed material[114, 113, 40] comprised of silicon skeleton and air voids. To describe the effective dielectric function of the material, $\epsilon_{\text{eff}}$, the 2D Maxwell-Garnett mixing formula was applied[77, 115]. Although the formula was already introduced in Chapter 2, for the sake of convenience, it was reformatted and presented here again:

$$\epsilon_{eff} = \epsilon_m + 2p\epsilon_m \frac{\epsilon_p - \epsilon_m}{\epsilon_p + \epsilon_m - p(\epsilon_p - \epsilon_m)}, \tag{4.1}$$

where $\epsilon_m$ and $\epsilon_p$ are the dielectric functions of the silicon skeleton and air-filled pores, respectively; $p$ is the volume fraction (71% in this work) of the pores, while the pores were treated as air having dispersionless permittivity of 1. The model approximates the pores as circular holes randomly distributed in the matrix which are dielectrically softer than the host background. The formula satisfies the required limits for vanishing inclusion (air) phase, when $p \to 0$ the effective dielectric function, $\epsilon_{eff}$, approaches that of the silicon matrix, $\epsilon_m$; and, vice versa, for $p \to 1$ it has the value of the air medium, $\epsilon_p$. The use of the formula is justified here as it obeys the requirement of the light field uniformity across a pore as its nanometrical dimension is significantly smaller than the micrometer probe wavelength. It should be noted that in general np-Si can be classified as an uniaxial birefringent material with the optic axis aligned along the pores direction (perpendicular to the sample surface)[35]. However, for $s$-polarised light, there is no electric field component parallel to that axis and the material can be treated as ordinary. Another point to address is water contamination molecules or their derivatives, chemi- or physi-sorbed on the walls of the pores. Although the amount of impurities is much smaller than that of the silicon in np-Si, their absorption coefficient can be at least ten times higher than that of the

free carriers contributed by the dopants [116, 117]. Hence, this has to be included in the calculation of the absolute reflectance, $R_0$, and transmittance, $T_0$. However, it is not necessary for the calculations of the fractional change of these values, $\frac{\Delta T}{T_0}(\Delta t)$ and $\frac{\Delta R}{R_0}(\Delta t)$, because $R_0$ and $T_0$ are known experimentally-determined functions and the fractional change is exclusively caused by the excitation of the free carriers[40].

To include the contribution of the free charges provided by boron dopants and those optically generated by the pump to the material optical response, the intrinsic dielectric function of the silicon skeleton, $\epsilon_{\mathrm{Si}}$, has been modified by adding the Drude term as introduced in Chapter 2:

$$\epsilon_{\mathrm{m}} = \epsilon_{\mathrm{Si}} - \frac{{\omega_{\mathrm{p}}}^2}{\omega^2 + i\omega\gamma}, \tag{4.2}$$

but with a slightly different plasma frequency

$$\omega_p^2 = \frac{e^2}{\epsilon_0}\left(\frac{N_{dop}}{m_h} + \frac{N_{pump}}{m_{eff}}\right) \tag{4.3}$$

which includes the contribution of the dopants due to the silicon substrate is heavily doped. $m_h$ and $m_{eff}$ denote the effective mass of hole when the doping is considered and the electron-hole reduced mass when the contribution of optically excited electron-hole plasma is calculated, respectively. The mass of hole and the reduced mass used in this work were 0.36 and 0.17 of the free electron mass[118, 119]. $e$ denotes the electron charge and $\epsilon_0$ is the vacuum permittivity. $\gamma$ designates the charge-carrier scattering rate, which phenomenologically includes all involved scattering mechanisms, such as scattering from the dopants, carrier-carrier and carrier-phonon collision, and interactions of the carriers with molecular vibrations on the surface of the silicon pores. $N_{dop}$ and $N_{pump}$ are the densities of the carriers provided by the dopants and excited by the pump, respectively. It should be noted that the Drude contributions of the free carriers provided by the dopants and those excited by the pump are additive. By substituting Eq.4.2 and Eq.4.3 into

Eq.4.1, the dependence of the effective dielectric function, $\epsilon_{eff}$, on the probe frequency, $\omega$, scattering rate, $\gamma$, and the free carrier concentration, $N$ are include in the optical model.

In the optical model the free carrier's distribution contributed by the dopants, $N_{dop}$, is assumed to be uniform along the membrane depth. However, the same assumption can not be used for the carriers excited by the pump, $N_{pump}$. It is anticipated that $N_{pump}$ will follow the profile of the pump fluence inside the sample, because the pump beam is linearly absorbed by the membrane, i.e. each pump photon generates only one electron-hole pair, $N_{pump}$, is an exponentially decaying function with the depth coordinate and it has the characteristic decay length inversely proportional to the pump absorption coefficient, $\alpha_{pump}$, which was determined in previous studies[114] to be 217 cm$^{-1}$. Due to the porosity the absorption of the samples is expected to be 300 cm$^{-1}$, assuming the bulk absorption coefficient is 850 cm$^{-1}$. However, the further decrease of the absorption coefficient is possible due to the confinement effect and shift of the band edge to a higher energy by 0.2 eV, as was previously determined[114]. This shift results in the reduction of the density of states available for the pump[120]. Therefore, the initially excited carrier density excited by the pump can be described by $N_{pump}(z, \Delta t = 0) = N^0_{pump}(\Delta t = 0)e^{-\alpha_{pump}z}$, where $z$ designates the coordinate along the sample depth and $\Delta t = 0$ is the time instance of the temporary overlap of the pump and probe on the surface. $N^0_{pump}(\Delta t = 0)$ is the initial density of the excited carriers on the surface. In general, $N^0_{pump}$ could be estimated using the values of the pump fluence and absorption coefficient. However, such an estimate is rarely sufficiently accurate, as it requires the accurate measurement of the fluence at the area of the pump and probe overlap, a very difficult procedure, which is prone to errors. Instead $N^0_{pump}(\Delta t = 0)$ was left as an input parameter for the calculation of the reflectance and transmittance using the optical model. Overall, the total carrier density used in the model is $N = N_{dop} + N_{pump}(z, \Delta t)$ with $N_{dop} = 3 \times 10^{18}$ cm$^{-3}$.

Although it is relatively straightforward to make a good approximation of the initial

function shape of the carrier distribution, $N$, a similar guess about damping rate, $\gamma$, is far from simple. This parameter includes an intricate convolution of different mechanisms introducing frictional damping to a carrier motion under the influence of the probe electric field. In the simplest form, its value provides a probability of collision of a carrier picked at random and moving freely between two subsequent scattering events. This value, which is inversely proportional to the relaxation time, is in general the weakest link in the modern theory of the high-frequency conductivity, and in many cases, treated as a phenomenological parameter without a precise understanding of the cause of carriers' collision and scattering, in particular in such complicated samples as np-Si. Moreover, $\gamma$ has entangled dependence on the carrier temperature, carrier density and the screening of the Coulomb interaction[121]. None of these factors are constant, and they change as a function of depth and time, following the initial excitation by the pump pulse. Consequently, the investigation and discussion of the causes of carrier scattering were left out of the arguments of this work. Instead, $\gamma(z, \Delta t)$ was treated as a phenomenological fitting function for each point of the decay curves shown in Figure 4.3.

To account for the excitation non-uniformity in the optical model for the calculation of the transmittance, $\frac{\Delta T}{T_0}(\lambda, \Delta t)$, and reflectance, $\frac{\Delta R}{R_0}(\lambda, \Delta t)$, Wentzel-Kramers-Brillouin (WKB) method was employed. It assumes a smooth nonuniform decaying dielectric function along $z$-coordinate, $\epsilon_{eff}(z)$, as defined by Eq.4.1. The dependance on the $z$-coordinate is due to the alteration of the excited carrier density and their scattering rate as a function of the membrane depth. By Combining the WKB method with the TMM introduced in Chapter 2, the analytical solution for the transmittance, $T$, and reflectance, $R$ can be obtained:

$$T = \left| \sqrt{\frac{q(0)}{q(d)}} \frac{(1 + r(0)(1 - r(d))}{e^{-i\psi} - r(0)r(d)e^{i\psi}} \right|^2 \tag{4.4}$$

$$R = \left| \frac{r(0)e^{-i\psi} - r(d)e^{i\psi}}{e^{-i\psi} - r(0)r(d)e^{i\psi}} \right|^2 \tag{4.5}$$

Where $r(0)$ and $r(d)$ are the reflection coefficients on the front and rear boundaries of the membrane sample, respectively. $q(z) = \sqrt{\frac{\omega^2}{c^2}\epsilon_{\text{eff}}(z) - k_x^2}$ is the position dependent wavevector of the probe along the sample depth and $k_x = \frac{\omega}{c} sin(\theta)$ is its tangential component which does not change along the propagation. $\theta$ is the incidence angle of the probe. $\psi = \int_0^d dz q(z)$ is the complex phase accumulated by the probe having frequency $\omega$ and propagating through the sample and multiple reflected from the boundaries inside the sample having thickness $d$. The detailed derivation and discussion of the model can be found elsewhere[122, 114].

To apply the model described above for the calculation of $R$ and $T$ at a given delay time, $\Delta t$, one needs initially to assume $N^0_{pump}$ and $\gamma^0_{pump}$ for the calculation of the complex dielectric function $\epsilon^0_{eff}$ on the front surface. Its value is then used to calculate the corresponding Fresnel coefficient, $r(0)$, and and the wavevector $q(0)$. Once $N^0_{pump}$ is set, the value of the carrier density on the back surface, $N^d_{pump}$, is restricted because $N_{pump}(z)$ is known as the exponentially decaying function described above. The scattering rate on the back surface, $\gamma^d_{pump}$, has to be initially guessed and consequently, the dielectric function of the back surface, $\epsilon^d_{eff}$, is calculated to obtain $r(d)$ and $q(d)$. Then $\gamma^0_{pump}$ and $\gamma^d_{pump}$ are connected by an exponentially decaying function to obtain $\gamma(z)$. Having both functions of $N_{pump}(z)$ and $\gamma_{pump}(z)$ available, the complex functions of $\epsilon_{eff}(z)$ and $q(z)$ are calculated by integration to obtain the complex phase $\psi$. This procedure is repeated iteratively to establish the best values of $q(0)$, $q(d)$, $r(0)$ and $r(d)$ for fitting of Eqs. 4-5 to the experimental results. Similarly the procedure can be applied for any delay to find the carrier density decay curves, $N_{pump}(z,t)$, which the best describe the experimental data of the reflectance and transmittance. A schematic representation of the optical model and notation are shown in Figure 4.5.

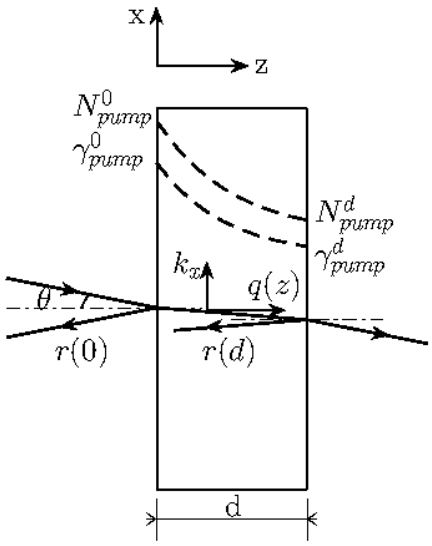


Figure 4.5: Schematic representation of the optical model showing the sample cross-section. The dashed lines illustrates the functions of $N_{pump}(z,t)$ and $\gamma_{pump}(z,t)$ drawn at an arbitrary scale.

Overall, the fitting procedure requires three initial guess parameters $N^0_{pump}$, $\gamma^0_{pump}$ and $\gamma^d_{pump}$ to fit simultaneously the experimental $R$ and $T$ recorded at a given delay time, $\Delta t$. These values are not arbitrary, but restricted by the experimental conditions and limits imposed by the physics. The best fit algorithm was allowed to look for the solutions in the boundaries of $N^0_{pump}(\Delta t)$ which are dictated by the minimum and maximum power absorbed on the surface across the pump beam spot. While $\gamma^0_{pump}(\Delta t)$ and $\gamma^d_{pump}(\Delta t)$ are limited not to deviate from the bounds between $10^{13}$ and $10^{15}$ sec$^{-1}$, a generally accepted range of the excited carrier relaxation rate in semiconductors.

Figure 4.6(a) shows the experimental and fitting results for transmittance and reflectance, $T_e$ and $R_e$, respectively as a function of the pump fluence for different wavelengths. Each point corresponds the maximum change of $\frac{\Delta T}{T_0}(\lambda, \Delta t)$ and $\frac{\Delta R}{R_0}(\lambda, \Delta t)$ around zero delay shown in Figure 4.3. Figure 4.6(b) shows the corresponding carrier

concentration used in the calculations, marking separately those excited by the pump on the surface of the sample, $N^0_{pump}(\Delta t = 0)$, and those provided by the doping, $N_{dop}$. Figure 4.6(c) depicts $\gamma$ used for the calculation of $T_e$ and $R_e$. Unlike the carrier concentration, $\gamma$ has relatively weak dependence on the pump fluence, but, on the other hand, its value varies for different wavelengths. A few additional observations about $\gamma$ can be made at this point. It has the greatest value at the probe wavelength of 3.5 μm suggesting a strong contribution of the vibrational mode of surface impurity Si-OH to the carrier scattering which is active at this frequency. Conversely, the lowest values of $\gamma$ were found for the 4 μm-probe, a wavelength which is not associated with any vibration of the np-Si and which is believed to be influenced by the free carrier-carrier and carrier-dopant collisions[40].

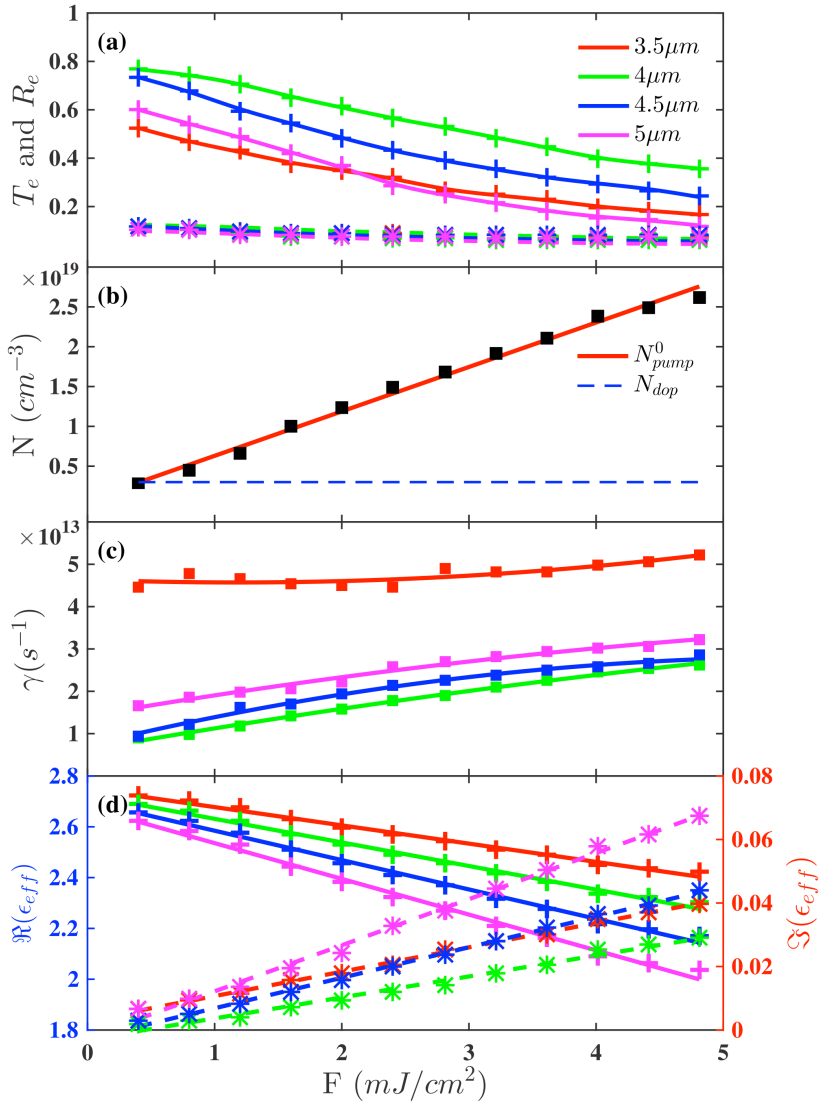


Figure 4.6: (a) Absolute transmittance,T, and reflectance, $R$, for 3.5 (red), 4 (green), 4.5 (blue) and 5 (magenta) μm probe wavelength, respectively. The crosses and stars correspond the experimentally determined transmittance and reflectance shown in Figure 4.3 at around the zero delay, $\Delta t = 0$, between the pump and probe. The lines show theoretical calculations using the optical model. (b) The carrier density used for the calculation of the transmittance, $T$, and reflectance, $R$. $N^0_{pump}$ is the carrier density on the surface of the samples at the zero delay, $N_{dop}$ is the carrier density induced by boron dopants. (c) $\gamma$ is the carrier scattering time on the front surface, for 3.5 - 5 μm probe wavelength, respectively, at around the zero delay time. (d) The corresponding real, $\Re\epsilon_{eff}$, (left axis) and imaginary, $\Im\epsilon_{eff}$, parts of the effective dielectric function, $\epsilon_{eff}$, respectively. The solid lines are shown to guide the eye.

Figure 4.6(d) shows the corresponding real, $\Re(\epsilon_{eff})$, and imaginary, $\Im(\epsilon_{eff})$, parts of the effective dielectric function dependences on the pump fluence. It can be seen that for the all probe wavelengths the fractional change of the real part is smaller than that for the imaginary part. For example, the maximum change of the real part is about 22% for the probe wavelength of 5 μm, while the corresponding change of the imaginary part covers almost an order of magnitude. This is very typical behaviour for the optical Drude response in the relaxation region where $\gamma \ll \omega$ and $\Im(\epsilon_{eff}) \ll \Re(\epsilon_{eff})$[123]. In this region the ratio of the real and imaginary parts change as a function of the fluence (and the carrier density) is given approximately by $\frac{\Delta\Re(\epsilon_{eff})}{\Delta\Im(\epsilon_{eff})} \approx \frac{\omega}{\gamma}$. For the 5 μm probe the ratio $\frac{\Delta\Re(\epsilon_{eff})}{\Delta\Im(\epsilon_{eff})} = 9.7$, while $\frac{\omega}{\gamma} \approx 11.6$, in quite close agreement with each other and where the minor discrepancy can be attributed to the fact that $\gamma$ is not constant, but changes slightly as a function of the carrier density. This observation supports the consistency of the Drude theory use for the description of the optical response in our samples.

### 4.2.4 Free Carrier Absorption

Another way to test the applicability of the optical model is to evaluate the probe absorption coefficient, $\alpha_{probe}$, dependence on the carrier density, $N$. In the relaxation region, the Drude model predicts that the absorption coefficient is governed by the second term of the following equation[123, 124]:

$$\alpha_{probe} = \alpha_0 + \frac{Ne^2}{4\pi^2 m_{eff}\epsilon_0 c^3}\frac{\gamma}{\Re(n_{eff})}\lambda^2 \ , \tag{4.6}$$

where $\alpha_0$ is the absorption coefficient in the absence of the pumping, $\Re(n_{eff})$ is the real part of the refractive index related to the effective dielectric function through the relation $\Re(n_{eff}) = \sqrt{\frac{\sqrt{\Re(\epsilon_{eff})^2 + \Im(\epsilon_{eff})^2} + \Re(\epsilon_{eff})}{2}}$ and $\lambda$ is the wavelength of the probe.

On the other hand, the absorption coefficient in the linear regime can be directly

obtained from the experimental data of the reflectance and transmittance, $R_e$ and $T_e$, respectively, shown in Figure 4.6(a), using the following formula:

$$\alpha_{probe} = \frac{log(\frac{1-R_e}{T_e})}{d} \tag{4.7}$$

Figure 4.7 shows $\alpha_{probe}$ around the zero delay determined from the experimental data and using Eq.4.7. $\alpha_{probe}$ presented as a function of the fluence, $F$, to which the carrier density, $N$, is linearly proportional. The use of Eq.4.7 rather provides the effective absorption coefficient defined by $\alpha_{probe} = 1/d \int_0^d dz \alpha^0_{probe} e^{-\alpha_{pump} z}$, where $\alpha^0_{probe}$ is the probe absorption coefficient on the surface. Alternatively, $\alpha_{probe}$ is calculated using Eq.4.6, using the mean values of $\langle N \rangle$, $\langle \gamma \rangle$ and $\langle n_{eff} \rangle$ found from the corresponding distribution functions of the sample depth.

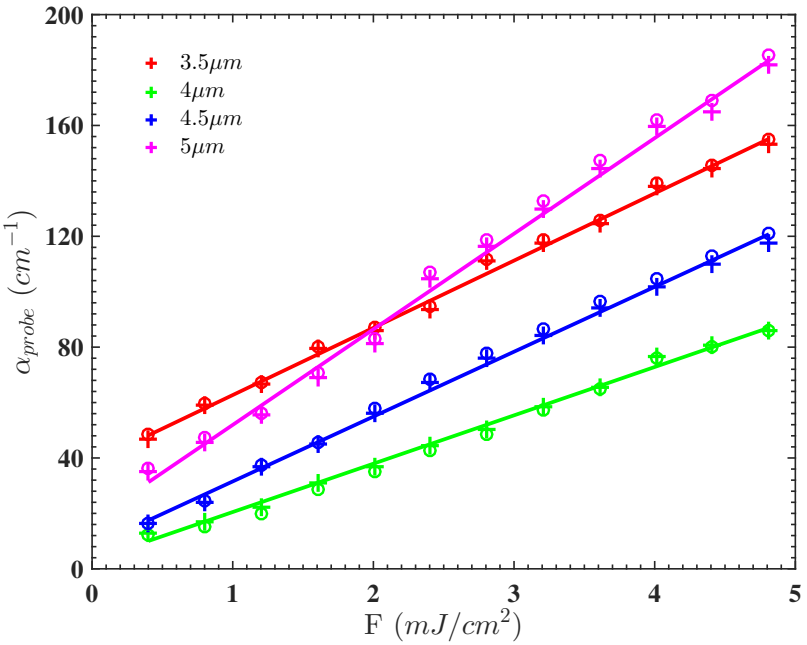


Figure 4.7: The absorption coefficient, $\alpha_{probe}$, of the probe for 3.5 (red), 4 (green), 4.5 (blue) and 5 (magenta) μm probe wavelength, respectively, at the zero delay, $\Delta t = 0$, and as a function of the pump fluence, $F$. The crosses represent the data obtained from the measurements, while the circles produced by the calculation using the optical model. The solid lines are shown to guide the eye.

It can be seen from Figure 4.7 that, for all four wavelengths, $\alpha_{probe}$ closely follows straight lines as, it would be expected for the free carrier absorption when $\gamma$ and $\Re(n_{eff})$ are both constant or their ratio is constant. However, Figure 4.6 suggests that $\gamma$ and $\Re(n_{eff})$ are not constant, but changing as a function of the fluence/carrier density. Nevertheless, their change is relatively small and opposite resulting in a nearly constant ratio of $\frac{\gamma}{\Re(n_{eff})}$ in Eq.4.6.

The intercept with ordinate axis in Figure 4.7 corresponds to the sum of the absorption coefficients of the free carriers contributed by the dopants and the surface impurities, both weighted by their corresponding volume fraction. For example, for the

5 μm probe and in the absence of the pumping, the absorption coefficient of the probe is $\alpha_{probe} = 24$ cm$^{-1}$. It can be approximated as $\alpha_{probe} \approx p_{Si}\alpha_{free} + p_{SiH}\alpha_{SiH}$, where $p_{Si} = 0.29$ is a known fraction of the silicon component and $p_{SiH}$ is an unknown fraction of $SiH$ impurities present on the surface of the pores and IR-active at this wavelength; $\alpha_{free}$ and $\alpha_{SiH}$ are well-documented absorption coefficients of the free electrons contributed by the boron dopants and $SiH$ molecular stretch, respectively. According to the literature $\alpha_{free} = 40$ cm$^{-1}$[117] and $\alpha_{SiH} = 1000$ cm$^{-1}$[125, 126]. Hence, the volume fraction of $SiH$ can be worked as $p_{SiH} = 0.012$. A similar estimate can be obtained for other IR-active vibrational modes of the surface impurities. Although $p_{SiH}$ is a small number, below the influence of the vibration has a crucial impact on free carrier dynamics. One of the reasons is that the impurities are not uniformly distributed over the volume, but located on the surface of the pores. Using the value of the samples' porosity and dimensions of the silicon framework obtained from Figure 4.1, one can estimated that $SiH$ bonds cover about $\sim 30\%$ of the surface pores area.

### 4.2.5 Time Resolved Carrier Density

In general, after the excitation by the pump the evolution of the carrier density function, $N(z,t)$, is governed by two major processes of diffusion and recombination and can be described by the following Eq.4.8 based on Fick's second law:

$$\frac{dN(z,t)}{dt} = D\frac{\partial^2 N(z,t)}{\partial z^2} - \frac{N(z,t)}{\tau_{eff}} \tag{4.8}$$

The first term of Eq.4.8 represents the one-dimensional diffusion along the depth coordinate. The diffusion in other directions can be ignored because the sample morphology which consists of interwoven, nearly unidirectional, quasi-one-dimensional wires arranged

along $z$-coordinate. $D$ is the diffusion coefficient, which is assumed here as a constant. The second term depicts the recombination rate with $\tau_{eff}$ denoting the effective recombination time.

The value of the diffusion coefficient, $D$, is not well-known for np-Si. Assuming that the carriers after the excitation obey Boltzmann distribution, the diffusion coefficient is given by $D = \frac{k_B T}{m_{eff}} \frac{1}{\gamma} \sim 6$ cm$^2$/s ($k_B$ and $T$ is the Boltzmann constant and equilibrium room temperature, respectively) for the highest value of $\gamma$ shown in Figure 4.6. This value is close to that of the bulk silicon observed for the similar carrier and dopant concentrations[127, 128]. However, at this moment it is problematic to corroborate this result relying on the data from the literature on np-Si as, to date, the diffusion process in np-Si remains poorly understood, with the reported values of $D$ scattering between $10^{-6}$ and 40 cm$^2$/s[129, 130, 131]. Such discrepancy may be related to the type and concentration of dopant and the morphology of np-Si.

Nevertheless, it can be shown that the diffusion process contributes insignificantly to the carrier dynamics. The diffusion term in Eq.4.8 has its maximum on the surface immediately after the excitation and can be calculated as $D\frac{\partial^2 N(z,t)}{\partial z^2}\Big|_{z=0,\Delta t=0} = D\alpha_{pump}^2 N_{pump}^0 \approx 7 \times 10^{24}$ 1/cm$^3$s. On the other hand, the observed decay rate is a few orders of magnitude faster. For example, the rate calculated as a slope to the initial concentration decay at the highest pump fluence at 3.5 μm probe in Figure 4.8 is $\frac{dN(z=0,\Delta t=0)}{dt} \approx 4.7 \times 10^{29}$ 1/cm$^3$s. Therefore, diffusion can be safely disregarded in Eq.4.8 and the following analysis of the decay data will be treated as a sum of weighted contributions from various recombination mechanisms presented by Eq.2.28. For convenience, it is presented again:

$$\frac{dN}{dt} = -\frac{N}{\tau_{eff}} = -bN - cN^2 - dN^3 \tag{4.9}$$

Eq.4.9 consists of three terms, where the first term corresponds to Shockley-Read-Hall (SRH) type, the second term is responsible for a radiative or bimolecular and the third

term describes Auger recombinations, respectively[132]. The order of each term denotes the number of free carriers involved in a process. The coefficients $b$, $c$ and $d$ depict the weight or rate constants for each process.

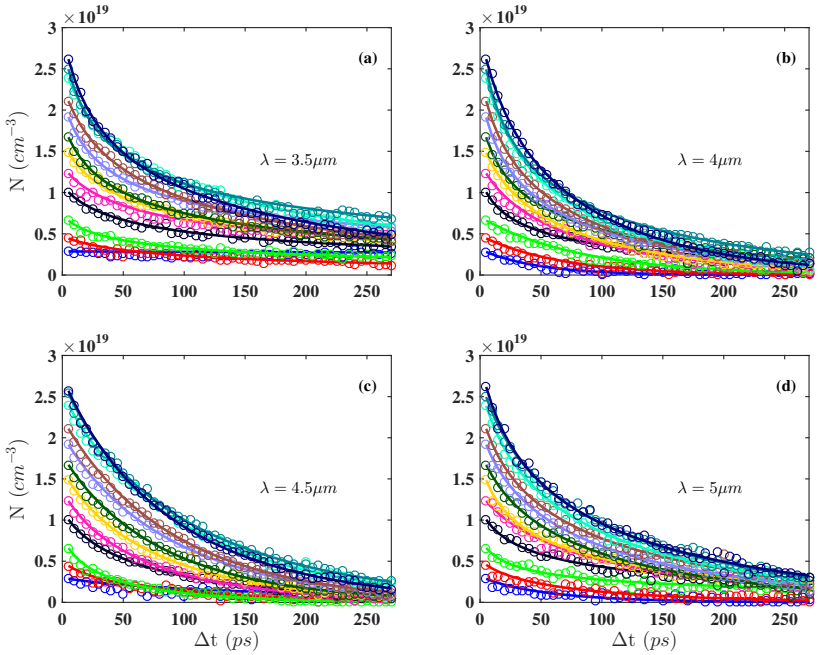


Figure 4.8: The carrier density, $N$, on the surface of the samples as a function of the delay time, $\Delta t$, between the pump and probe. (a), (b), (c) and (d) corresponding to the probe wavelength of 3.5, 4, 4.5 and 5 μm. The curves on each plot relate to a different pump fluence in the range between 0.4 and 4.8 mJ/cm$^2$.

In the SRH process occurring in the bulk material, the magnitude of the corresponding rate constant mostly depends on the density of the ionized boron impurities forming in-gap states and their ability to capture electrons moving in their vicinity[133, 134]. Strictly speaking, the first term describes not only SRH, but the surface recombination as well, which is a type of SRH recombination via surface impurity states. The recombination due to trapping by the states formed in the shell encapsulating the silicon channels is

described by this process as well.

The surface recombination in the bulk silicon is known for playing a significant role in the carrier dynamics as demonstrated by the measurements using the reflectivity pump-probe method[119, 135]. Statistically SRH via midgap and surface states are equivalent and can not be easily separated in a single measurement. Moreover, in np-Si the mean diameter of the silicon channels is comparable to the thermal wavelength of the mobile carriers. In such conditions, any mobile carrier has a wavefunction which extends over the entire cross-section and it nearly equally overlaps with the impurities located in the interior and on the surface of the channels. The time to move from the inside to the surface is essentially zero and the surface velocity cannot be defined. Therefore the relevant capture time corresponds to instances of the carrier trapping when it moves laterally along the wire. For the sake of clarity, this process is noted as SRH, however it includes both the recombination on impurities inside and outside of silicon channels because they are indistinguishable without physical alteration of the composition.

The second term is usually attributed to radiative electron-hole recombination in band-to-band to transition. In np-Si samples used in this work, the radiative process is absent. However, it was proposed that a trap-assisted Auger recombination should also be considered for the evaluation by the second term[136, 137]. The last term is attributed to the ambipolar Auger recombination, where fast-moving electrons develop a potential drop, pulling the holes to proceed in a joint diffusive motion accompanied with the annihilation of the charge carriers.

Eq.4.9 was solved numerically to find the best fit to the data of the carrier density decay, $N(t)$, as a function of time. $N(t)$, shown in Figure 4.8, was calculated from implementing the optical model described in the Section 4.2.3 to each point of the measurements of the time resolved transmittance and reflectance shown in Figure 4.3.

Figure 4.8 shows the obtained time-resolved carrier density on the surface of the sample for the different pump fluences and probe wavelengths. The empty circles represent the data obtained from the optical model. The solid lines show best fit of the solution of Eq.4.9 to the data of the carrier density. The initial carrier density, at the zero-delay time, is the same and independent of the probe wavelength as it relates to the pump fluence only. However, the curves have dissimilar decay shapes for different probes, indicating that the decay rate is wavelength dependant.

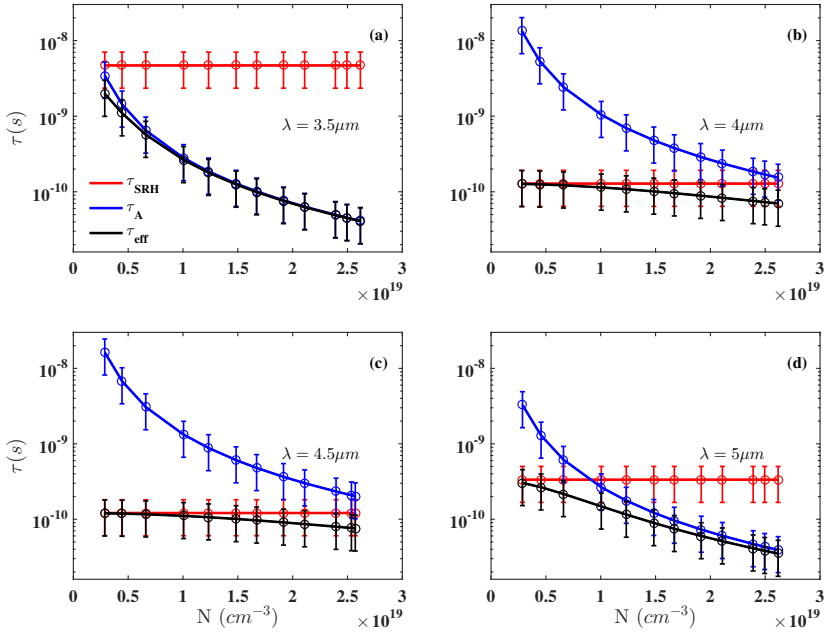


Figure 4.9: Recombination times $\tau_{SRH}$ shown in red and $\tau_A$ shown in blue corresponding Shockley-Read-Hall and Auger processes, respectively, as a function of the initial free carrier density, $N^0(\Delta t = 0)$, on the surface of the np-Si samples. The times were evaluated from the fitting of the solutions of Eq.4.9 to the data shown in Figure 4.8. $1/\tau_{eff} = 1/\tau_{SRH} + 1/\tau_A$ depicted in black is shown for the comparison.

The recombination times obtained from the fitting of Eq.4.9 are shown as a function

of the initial carrier density in Figure 4.9, where $\tau_{SRH} = 1/b$ and $\tau_A = 1/dN^2$. It is found that the bimolecular term in Eq.4.9 has no significant contribution to the decay over the given range of the carrier densities. Moreover, the attempts to fit the data assuming $d = 0$, but considering the involvement of the first two terms only in Eq.4.9 did not produce the satisfactory results. Therefore, the results of the best fitting suggest that SRH and Auger are the main mechanisms contributing to the decay of the excited carriers. The absence of the bimolecular band-to-band transitions bears similarity to the recombination dynamics of bulk Si[138], where a typical value of the rate constant in the bulk material is $c = 9.5 \times 10^{-15}$ cm$^3$/s, which would correspond to a life time of $4 \times 10^{-6}$ s at the highest density of the free carriers and at a rate which is substantially longer than the effective rate observed in this work. Alternatively, an early report on the pump-probe time-resolved measurements of np-Si suggested that the band-to-band transition is a significantly faster process with $c = 9.5 \times 10^{-10}$ cm$^3$/s. However, the samples used in that study are likely to have differed from this work in that the dimensions of their silicon constituent approached the quantum confinement regime which modifies the band structure of silicon to behave as a nearly direct band-gap material[139]. Nevertheless, that observation seems to contradict a later work which performed and analysed a similar set of the experiments, and concluded that recombination dynamics is likely to be influenced mostly by the trap capturing of the excited carriers and at higher intensities by the non-radiative Auger recombination[140], in line with the analysis here. Yet, these studies were limited to the measurements which used a single wavelength only and a very limited range of the pump fluence.

Moreover, Figure 4.9 suggests that the involvement of the SRH and Auger processes is not constant when the density decay is probed with different wavelengths. It can be seen that, at 3.5 μm the recombination is strongly dominated by Auger, while the situation is completely reversed for the probe having wavelengths of 4 and 4.5 μm, where the decay is dominated by SRH. For the probe of 5 μm the picture is more mixed, the recombination

is rather dominated by SRH at the low end of the initial carrier density and it is governed by Auger at the higher concentrations. To investigate the phenomenon of the competition between the Auger and SRH, a more detailed study of the recombination time dependence on the probe wavelength was performed.

### 4.2.6 Carrier Density Decay as a Function of the Probe Wavelength

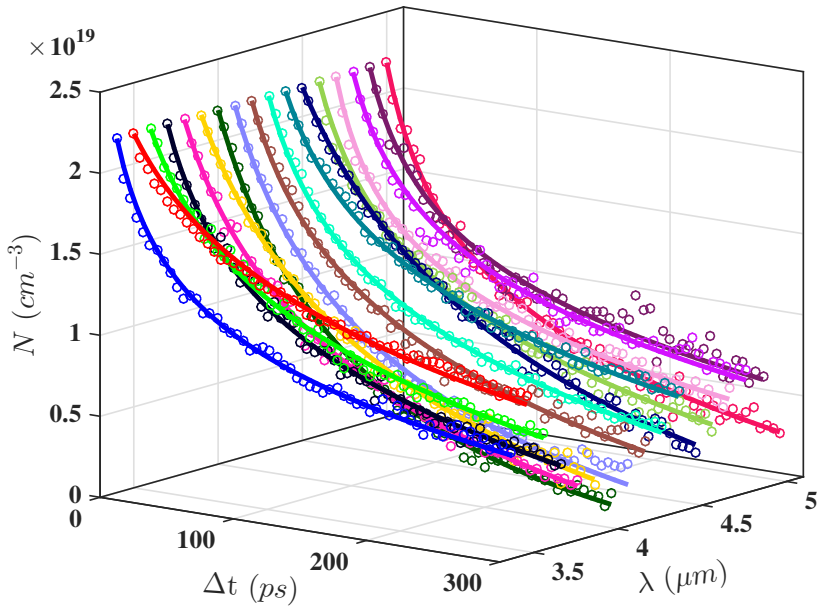


Figure 4.10: The free carrier density, $N$, as a function of the delay time, $\Delta t$, for different probe wavelengths and for a fixed pump fluence of 4 mJ/cm$^2$.

To investigate carrier dynamics as a function of the probe wavelength, a number of time-resolved measurements were performed using 17 probe wavelengths equally dividing the range between 3.4 and 5 µm. The pump fluence was fixed at 4 mJ/cm$^2$, corresponding to the initial carrier density of $2.4 \times 10^{19}$ cm$^{-3}$ on the surface. The measurements of the

correspondent transmittance change are shown in Figure 4.4. Using the optical model, the decay curves were derived for the carrier density and for each probe wavelength. Each curve was fitted with solution of Eq.4.9 and they are shown in Figure 4.10. The decay times obtained from the fitting are shown in Figure 4.11(e) as a function of wavelength .

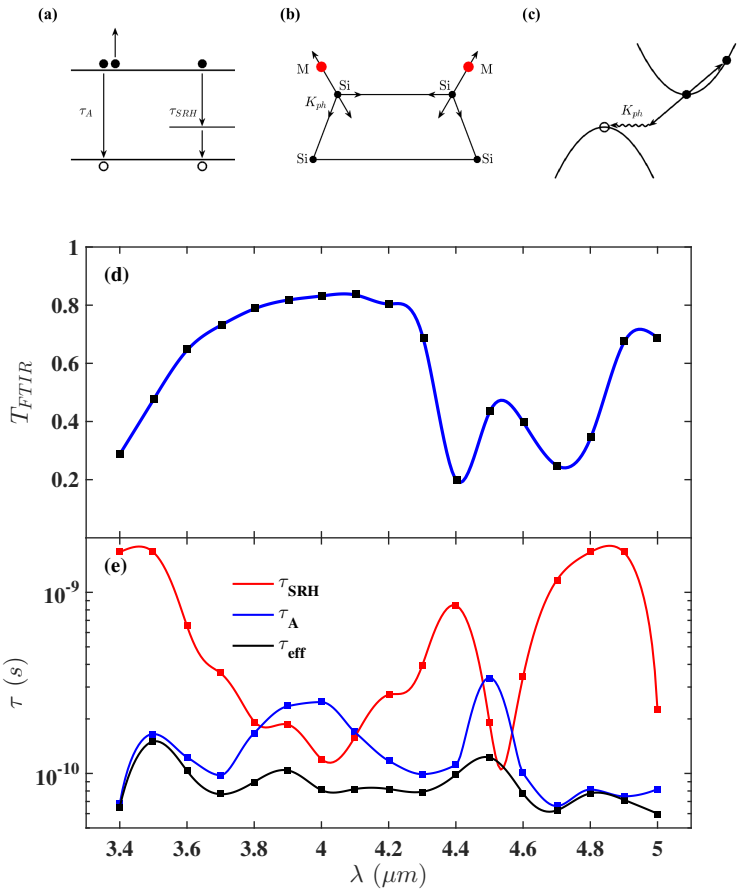


Figure 4.11: (a) Two main competing nonradiative recombination channels in np-Si; (b) a possible coupling mechanism of a stretching mode of surface-adsorbed molecular impurities M to the bulk phonons; (c) phonon-assisted Auger recombination. The correlation between (d) FTIR transmittance and (e) recombination times. In (d), $\tau_{SRH}$, $\tau_A$ and $\tau_{eff}$ are shown in red, blue, and black, respectively. The pump fluence is 4 mJ/cm$^2$ and the carrier density on the samples surface immediately after the excitation is $N(z = 0, \Delta t = 0)$=2.4×10$^{19}$ cm$^{-3}$.

To understand the nature of the factors governing the recombination dynamics, the recombination times' dependence on the wavelength was correlated with the FTIR measurements. The purpose of FTIR is to indicate the vibrational modes of the lattice and impurities active in this spectral range. The FTIR spectrum shown in Figure 4.11(d) is dominated by the stretching modes of $SiOH$ vibration with the central wavelength located at 3 μm and whose tail is observed here between 3.4 and 3.8 μm, $OSiH_3$ at 4.4 μm and $SiH$ at 4.8 μm[141, 142, 125]. These molecular vibrations are known to be present in abundance on the surface of the pores and were also observed in the earlier research into bulk silicon surface impurity states[143]. However, in contrast to bulk silicon, in np-Si, the effective surface is considerably larger and the contribution of these modes pertains not only to the dynamics of the carriers near the samples' surface but to their entire volume.

It can be seen from Figure 4.11 that there is a strong correlation between the spectrum of the vibrational modes and the recombination times. In particular, it can be observed that the contribution of the SRH mechanism is suppressed, as $\tau_{SRH}$ becomes longer, at the wavelength corresponding to the IR active modes, while Auger recombination is enhanced with $\tau_A$ gets shorter. At 3.4 μm, $\tau_{SRH}$ is so slow that the recombination is completely dominated by Auger recombination. This conclusion can also be derived from Figure 4.9(a) at 3.5 μm. However, as the wavelength increases towards 4 μm the situation is nearly reversed - the recombination process is dominated by SRH while Auger is slowed down. This pattern repeats itself at other peaks, with active vibrational modes around 4.4 and 4.8 μm where SRH is subdued but Auger is enhanced.

These findings strongly suggest that the non-radiative Auger process in np-Si, despite some similarities to the bulk material, has its own unique features. First, it is significantly faster than in bulk which has been injected with similar carrier densities. For the bulk silicon, Auger lifetime at the excess carrier density of $10^{19}$ cm$^{-3}$ is a few tens of nanoseconds[144, 145], while the values estimated for samples of this work are

almost three orders of magnitude faster, approaching tens of picoseconds. Second, in the majority of works, Auger recombination in the bulk silicon is assumed to proceed with a restriction of the conservation of both energy and momentum. It was proposed theoretically that the momentum conservation restriction can be circumvented by the involvement of a phonon, which provides the necessary matching conditions to cross the indirect energy-gap in silicon[146]. However, there is insufficient experimental evidence to substantiate such a mechanism in bulk silicon. In contrast, the results in this Chapter point to a recombination mechanism where the Auger process is dominant only when it is assisted by vibrational modes of the surface impurities, otherwise it is controlled by SRH.

It can be argued that the opening of the vibration-assisted Auger recombination channel in np-Si is attributed to its peculiar morphology. In np-Si, the charge carrier is confined to moving along a quasi-one-dimensional wire having a diameter comparable to de Broglie wavelength. In such a confined motion, it interacts strongly: not only with the molecular vibrations excited on the surface by the probe but, as well, with phonons generated in abundance by the deformation of the lattice structure through the coupling to the molecular vibrations located on the pores' surface. For instance, it was recently proposed theoretically that excited Si-H stretching mode ($\sim 0.25$ eV) may decay into a few quanta of the Si-H bending mode ($\sim 0.08$ eV) and the substrate phonon modes (the largest silicon bulk phonon frequency is $\sim 0.07$ eV)[147]. Although, this process might appear as not a very efficient one, it still can have a substantial effect in the experiment because the density the molecular adsorbates on the surface is almost two orders of magnitude higher than the corresponding density of the charge carriers. There are also a growing number of reports of the effective molecular vibrations decay via emission of multiple bulk phonons in silicon and germanium. For example, it was shown that vibrations of oxygen in bulk silicon may decay with emission of three phonons on the time scales of a few tens of picoseconds[148]. In a similar system of hydrogen adsorbed on germanium the decay

of the stretch mode can proceed via emission of three bulk phonons within one hundred picoseconds[149].

On the other hand, the phonon mean free path is significantly larger than the wires diameter [150] and, once generated by the deformation and coupling to the adsorbates vibrations, phonons occupy the entire volume of the wires, scattering charge carriers, and providing the momentum needed to cross the gap and enhance the Auger process.

To justify the observed values of $\tau_{SRH}$, specifically those approaching $10^{-10}$ seconds at 4.5 μm, it should be noted that the corresponding capture cross-section for carriers at room temperature is $\sigma = 1/(vN_{dop}\tau_{SRH}) = 3.3 \times 10^{-16}$ cm$^2$, where $v$ is the thermal velocity. This estimate is somewhat above a typical value for ionized impurities in silicon[151, 152] and large enough to be comparable to the cross-section of the silicon channels. The reason for the cross-section overestimate is because the actual process is more complex and not limited to the capture and collision with impurities only. In addition to the scattering on the dopants, other irregularities such as potential extended and point defects within the silicon skeleton, irregularities of silicon channels and surface impurities are also involved in the process, but not accounted in the estimate. As argued above, the carrier occupies the entire cross-section and its quasi one-dimensional motion can be interrupted by almost any impurity encountered along the way, leading to the observed high rate of recombination. Nevertheless, the SRH process is subdued when the probe wavelength coincides with the vibrational resonances of the surface molecules initiating strongly competing Auger recombination.

In conclusion, the ultrafast pump-probe technique was employed to study the carrier dynamics of np-Si membranes. The time-resolved change of transmittance and reflectance revealed that both the morphology and surface chemistry play important roles during the carrier recombination process. Due to the restriction of electron movement by

the wire-shaped skeleton of np-Si, the probability of carrier-carrier, carrier-phonon and carrier-impurity collision increases, resulting in a drastic enhancement of the recombination rate compared to the bulk silicon. The experimental results show that the recombination rate of np-Si is about three orders of magnitude higher than its bulk counterpart. Further fitting the experimental results with the rate equation revealed that the dominant carrier recombination mechanisms in np-Si are SRH and Auger process. In addition, the wavelength dependence of the recombination rate indicates that the surface chemistry also influences the recombination process. It was found that the enhancement of the Auger recombination rate at specific probe frequencies is associated with the active vibrational mode of the absorbates on the pore surfaces. The vibration of the molecules can couple to the phonon mode of np-Si, which further enhances the Auger recombination and surpasses the SHR process.

# Chapter Five

# Applications of Macro-Porous Silicon in Short- to Mid-Wavelength Infrared Range

**This chapter is a reformatted version of my papers: 1. 'All-Optical Modulation and Ultrafast Switching in MWIR with Sub-Wavelength Structured Silicon', R. Wu, J. Collins, D. Chekulaev and A. Kaplan, Appl. Sci. 2019, 9(9), 1808; 2. 'Demonstration of time-of-flight technique with all-optical modulation and MCT detection in SWIR/MWIR range', R. Wu, J. Collins, C. D. Burgess, R. A. Lamb, A. Kaplan, SPIE Proceedings 1079904 (2018).**

As the most common semiconductor in electronic integrated circuit, silicon has been considered as one of the best candidates for the natural hybrid of photonic and electronic devices[153]. In recent years, various silicon-based devices have been proposed for the generation, modulation and detection of light[154, 155, 156, 157]. The combination of silicon photonics with electronic devices not only brings the advantage of improved bandwidth and fundamental speed, but also shows the potential of massive production with

low fabrication cost in comparison with other semiconductors. Among all the silicon-based photonics units, the optical modulator, as one of the most critical components in optical communication, thermal sensing and imaging systems, has drawn great research interest lately [158].

The conventional approach to optical modulation is based on the first order electro-optical effect (Pockels effect) of materials. That is, by applying an external electric field, the dielectric function of the material alters and results in a modification of the optical response and a change of the reflectance or transmittance of the incident light. However, as a centrosymmetric semiconductor, intrinsic silicon does not have the electro-optical effect, therefore, not an ideal material for implementation in electro-optical modulation[159, 160]. As an alternative method, thermal-optical modulation was investigated by Cocorullo et al., but it is only suitable for low repetition rate applications due to its slow response[161, 162]. Currently, the free carrier plasma dispersion effect, where the material optical response varies with the free carrier density, is the most commonly-investigated modulation mechanism in silicon[163]. The free carrier density can be altered by carrier depletion, accumulation or injection by either electronic or optical means[164]. The latter case is known as all-optical modulation, which has its primary advantage in ultrafast modulation speed, typically in the picosecond range[165]. As early as in 2004, Almeida et al. demonstrated a scheme of ultrafast all-optical modulation with silicon photonic structures at telecommunication wavelengths. A modulation depth of 90% with less than a 500-ps modulation speed was achieved[166]. Soon after, Takasumi's team reported an improved modulation speed of 70 ps by using ion-implanted silicon photonic crystal nanocavities[167]. So far, most of the research interests and achievements in silicon optical modulators (including the examples mentioned above) have explored the range of telecommunication wavelengths. The Mid- to Long-Wavelength Infrared region (MWIR and LWIR, respectively) has so far attracted less attention, despite the enormous potential and high demand on the market[168].

The most demanding applications operating in MWIR, such as thermal imaging, security countermeasures and free space communication, exploit the high transmittance of the Earth's atmosphere in the wavelength range between 3.5 and 5 μm. A longer wavelength assures that there is less scattering compared to the near-infrared and visible light, as well as no active vibrational transitions of $H_2O$ and $CO_2$ molecules, making it suitable for remote sensing and detection with little influence from weather conditions[169]. Despite the importance and maturity of the current MWIR detection and imaging technology, the present applications rely entirely on electronic and mechanical modulators, which limits the modulation speed to a few hundreds of nanoseconds. The development of all-optical modulators aims not only at improving the performance speed, but also at enabling new functionalities, such as ultrafast time-of-flight detection, anti-fluctuation atmosphere 3D imaging and broadband free space communication, based on the current MWIR detection technologies[40].

Range-finding and 3D imaging provides information about the distance to an object in addition to the standard intensity received by detector or camera. Since the first Time-of-Flight (ToF) imager was demonstrated[170], it became apparent that this active measuring technique offers advantages over passive and active triangulation[171, 172]. However, the main development of ToF imaging and distance measurement was reported for the visible and near-IR ranges, similar achievements in far-IR (MWIR and LWIR) have not yet materialised despite clear technological advantages that the ToF technique can offer in this range. One of the problems is the ultrafast gating of the detectors operating in the far-IR, which at their best can achieve a few nanoseconds, more than an order of magnitude slower than their counterparts in the visible range[173]. Therefore, an external optical modulator would be a beneficial choice for the improvement of MWIR ToF resolution, and the advancement of MWIR optical modulator technology will eventually promote the development of range-finding and 3D imaging technology.

It is also worth mentioning that, a reliable detection method is important for the ToF applications. The major players in MWIR imaging industry, such as Leonardo, Raytheon, Sofradir and SCD consider Mercury Cadmium Telluride (MCT) as a semiconducting material with noticeable advantages over other rivals, such as InSb. MCT detectors offer a better range of detection, resolution, device size and performance-to-cost value. MCT is the only known detector material which covers the spectral ranges of short, mid and long wavelength IR (SWIR, MWIR and LWIR). Because of its robust performance, MCT became an integral part in the most demanding applications in the battlefield, as in the Phalanx CIWS shipboard defence system operating in LWIR and DIRCM countermeasure sensors for protecting military aircrafts in MWIR. In addition, MCT has demonstrated the ability to produce clear signal in the scene flooded with photons and where the parasitic reflection can be discriminated from useful ones by gating and filtering photons arriving before or after those reflected from the useful target. Therefore, a natural development would be the integration of MCT detectors into an active measurement and imaging device using the ToF technique.

Due to the crucial role of MWIR optical modulator as mentioned above, the aim of the work in this Chapter is to present the development of an all-optical modulator with high speed and suitability for MWIR applications. Briefly, the core of the modulator is a silicon-based membrane (macro-porous silicon). When an external optical source optically excites the membrane by pumping free electrons, its reflectance and transmittance change due to the alteration of the effective dielectric function by the excited free electrons. Using an external pulsed pump source, it is possible to modulate a synchronous response of the membrane, switching it between the fully transmitted and opaque states. The modulated membrane is positioned in front of the detector and acts as a shutter which can be activated synchronously with a pulse from an external optical source. Such arrangements allow the use of detectors with a slow response as the resolution is determined by the response of the

modulator. The speed of the modulation is limited by the pulse properties of the pump source and the free carrier lifetime. In this work, a 100 femtosecond laser was used as pump source, which defines the rise time of the modulator. The life time of the free carriers is in the range of a few tens of nanoseconds or shorter due to Auger recombination which determines the time required for the modulator to return to its initial transparent state. The recovery time in such a set-up determines the repetition rate at which the modulator can be potentially used. In Section 5.1, the overall performance of the modulator in the frequency and time domains are investigated and the pump fluence required to achieve the optimised modulation are quantified. The results suggest the enhanced modulation depth of the macro-porous silicon (mp-Si) in comparison to the bulk counterpart under the same experimental condition. The temporal response of the modulator was explored and the experimental conditions was specially designed to achieve the ultrafast modulation of 0.55 ps. Furthermore, Section 5.2 demonstrates a ToF set-up based on the optical modulator as introduced in Section 5.1. The speed corresponding to the ToF resolution of a few tens of micrometers is shown which allows to measure subtle effects of a pulse broadening by Group Velocity Dispersion (GVD) in a few centimetre long silica rod. As well, a pulse broadening developed by propagation through the rod and the GVD of silica were estimated from the signal received by the detector.

## 5.1 All-Optical Modulation and Ultrafast Switching with Macro-Porous Silicon

### 5.1.1 Methods and Samples

A femtosecond laser system was used to measure the time-resolved reflectivity of the optically-excited samples. The detailed description of the system can be found in Chapter 3. The wavelength of the pump beam was 800 nm and the probe beam was in the range between 4 and 6 μm. The pump beam was set to be *p*-polarised while the signal beam was *s*-polarised. The incident angles of the signal and pump beam at the sample surface were 20°and 30°, respectively. The reflected MWIR beam was directed to a home-built monochromator, with a resolution of 10 nm, to monitor the spectral response. A Mercury Cadmium Telluride (MCT) detector was placed at the exit of the monochromator equipped with a pre-amplifier and a lock-in amplifier to collect the IR signal with a low signal-to-noise ratio of less than 3%.

The macro-porous silicon membrane was used as the modulator material in this work. The fabrication procedure can be found in Chapter 3 and other literature[174, 175]. In short, an ordered hexagonal 2D array of holes was etched through the bulk silicon membrane. The thickness of the sample was about 15 μm, with 0.5 μm holes spaced 1.5 μm apart, as shown in the insert to Figure 5.1(b). Bulk silicon (similar membranes without holes) was used as a reference to compare the results with the mp-Si membranes.

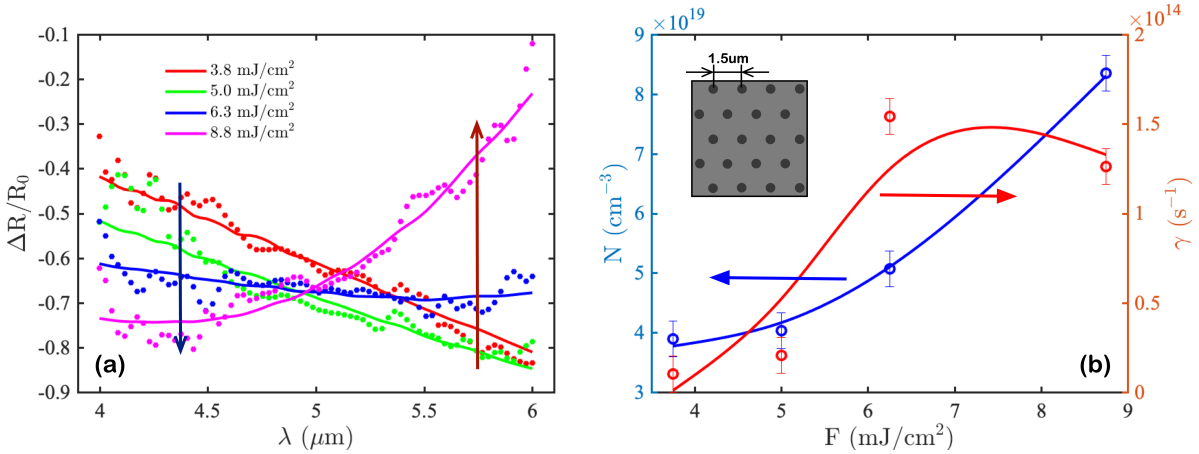


Figure 5.1: (**a**) Change of the reflectance, $\Delta R/R_0$, at the temporal overlap between the pump and signal as a function of signal wavelength $\lambda$ recorded for the pump fluences of 3.8 mJ/cm$^2$ (red), 5.0 mJ/cm$^2$ (green), 6.3 mJ/cm$^2$ (blue) and 8.8 mJ/cm$^2$ (magenta). The dots denote the experimental results, and the solid lines show the model fitting. The arrows indicate the change of reflectance with increasing pump fluence at a given wavelength, on the shorter and longer spectral ends, blue and red, respectively. (**b**) The carrier concentration, $N$, (blue) at the sample surface and its scattering rate, $\gamma$, (red) as a function of the pump fluence. The curves were reconstructed from the experimental data shown in (a). The insert shows the top view of the macro-porous silicon used in this work.

### 5.1.2 Wavelength Dependence and Ultrafast Temporal Response of Optically-Pumped Membranes

Figure 5.1(a) shows the reflectance change, $\Delta R/R_0 = (R_e - R_0)/ R_0$, measured at the temporal overlap between the pump and signal pulses, as a function of the signal wavelength and for the different fluences of the pump, spanning between 3.8 and 8.8 mJ/cm$^2$. $R_e$ and $R_0$ denote the reflectance with and without application of the pump pulse, respectively. The dots and solid lines represent experimental results and optical model fitting, respectively. The corresponding carrier concentration, $N$, used in the calculation of the optical model,

and the scattering rate, $\gamma$, as a function of the pump fluence are shown in Figure 5.1(b). Note that $N$ and $\gamma$ are functions of the fluence only and were not influenced by the probe, as its fluence was too weak and the photon energy too small to alter them. In general, it can be seen that the optical model can be adequately fitted to the experimental results, providing a background to discuss the physics behind the findings and the feasibility to use the membranes for a reflective-type light modulator.

It can be seen that at certain conditions, the modulation efficiency can reach beyond 80%, yet it is not uniform over the entire range of wavelengths. At the lower fluence of about 4 mJ/cm$^2$, the greatest modulation was observed at the longer wavelength of the spectrum around 6 μm, while at the highest fluence, the situation was reversed: it was the shorter wavelength around 4 μm that was the most affected. Such dependence of the reflectance spectra on the pump fluence can be considered for use in tunable spectral filters. At the lower pumping, the membrane acted as a shortwave reflecting filter, i.e., at 3.8 mJ/cm$^2$, almost 70% of the 4 μm probe was reflected back, while for 6 μm, it was only 15%. At the highest fluence, the filter reflectance as a function of the wavelength was flipped over: it behaved as a a long-wavelength reflective filter with 90% of 6 μm and 25% of 4 μm reflected back, respectively. Overall, there are two critical details that need to be explained, which are the sign of the reflectance change as a function of the fluence, F, for a given wavelength $\lambda$, $\frac{\Delta R}{R_0}(F)_\lambda$, indicated by the arrows on Figure 5.1(a), and its absolute value characterising the modulation contrast. It can be seen that $\frac{\Delta R}{R_0}(F)_\lambda$ has the opposite sign: it was negative for the shorter wavelength and reversed to the opposite for the longer wavelength, while its absolute value was greater.

To understand this behaviour, one should examine the evolution of effective dielectric function $\epsilon_{eff}$ as a function of the injected free carrier density, $N$, and relate it to the reflectance. When the carrier density, $N$, increases, the dielectric function, $\epsilon_{eff}$, monotonically drops, yet the reflectance behaviour is more complex than that. At the

lower carrier injection, the contribution of carrier concentration to the dielectric function is less than its intrinsic dielectric function, the increase of $N$ led to the decrease of the reflectance. However, a further increase in the carrier concentration $N$ results in $\epsilon_{eff} \to 1$, where the reflectance reaches its minimum. After that, the reflectance increases with $N$ until it reaches the maximum value at $\epsilon_{eff} = 0$. The change of the sign at $\frac{dR}{d\epsilon}\big|_{\epsilon=1}$ corresponds to the onset of the transition of the optical response from dielectric to metal, also known as the plasma edge. Furthermore, it can be shown that in semiconductors at the conditions around the plasma edge for a given signal wavelength, $\lambda$, the absolute value of reflectance change as a function of the carrier concentration has the relation of $\left|\frac{\Delta R}{R_0}(N)\right|_{\lambda;\ 0<\epsilon_{eff}<1} > \left|\frac{\Delta R}{R_0}(N)\right|_{\lambda;\ \epsilon_{eff}>1}$. This discussion equally applies to $\frac{\Delta R}{R_0}(F)_\lambda$, assuming that $N$ is directionally proportional to $F$. Thus, the opposite sign and the difference of the absolute values of the arrows in Figure 5.1(a) indicated that the system was pumped in the region of dielectric-metal transition, where at the shorter wavelength $\epsilon_{eff} > 1$, while at longer wavelength approaching 6 μm $\epsilon_{eff} < 1$ and at the crossover around 5 μm $\epsilon_{eff} = 1$. It should be noted that, compared to the bulk semiconductor, less pumping was required to achieve this transition with mp-Si membranes, as their dielectric function was lower due to the presence of holes. Therefore, increasing the porosity of the mp-Si membrane will result in a reduction in the required pumping energy (improve efficiency), but at the cost of a reduction in mechanical strength.

Figure 5.1(b) shows the fitting parameters used to calculate $\Delta R/R_0$. To improve the accuracy, a calculation routine that iteratively determines the real and imaginary parts of the effective dielectric function, $\epsilon_{eff}$, from the amplitude and slope of the experimentally measured $\Delta R/R_0$ as a function of $\lambda$ [176] was used. The fitting results suggested that with the carrier concentration above $8 \times 10^{19}$ cm$^{-3}$ and scattering rate of about $1.5 \times 10^{14}$ s$^{-1}$, dielectric-metal transition occurred for signals with $\lambda > 5$ μm. Moreover, it can be seen that $N$ is a non-linear function of $F$; therefore, the initial assumption of the linear

absorption of the pump pulse has to be corrected. In addition, the scattering parameter, $\gamma$, seemed to saturate at the higher fluences. The most likely reason for this is the saturation of the carrier-carrier collisions at the non-equilibrium conditions [177].

To further investigate the optical response and the temporal evolution of the spectra at different pump fluences, ultrafast pump-probe measurements were performed over a few picoseconds delay time between the pump and probe pulses. During this time, the injection of the charge carries reached saturation as the excitation process had been completed, but the recombination had not developed yet to affect the carrier density and optical response. It is noted that the temporal resolution was degraded by the convolution of the ultrafast excitation and longer probe pulse. The results are shown in Figure 5.2(a)-(d) for the pump fluences of 3.8, 5.0, 6.3 and 8.8 mJ/cm$^2$, respectively. These measurements can be viewed as the evolution of the curves shown in Figure 5.1(a) as a function of time (along the horizontal axis). Figure 5.2(a)-(c) show that after the excitation completed, the spectra did not change significantly after 1 ps as a function of the delay time, $\Delta t$. That is, once the equilibrium was achieved, the optical properties remained stable. However, in Figure 5.2(d), a peculiar feature around 6 μm and the delay time of 1 ps was observed, as indicated by the dashed rectangular. Unlike anywhere else, in this region, the signal passed through the minimum before it recovered and stabilised. This curious behaviour is interesting for both understanding the physics behind the process and the possible development of applications. Indeed, such an ultrafast drop and recovery of the reflectance signal at a particular wavelength can be used for the extremely fast reflective-type all-optical switching. In the next Section, this ultrafast temporal variation of the reflected signal and the physics behind it will be discussed in more detail.

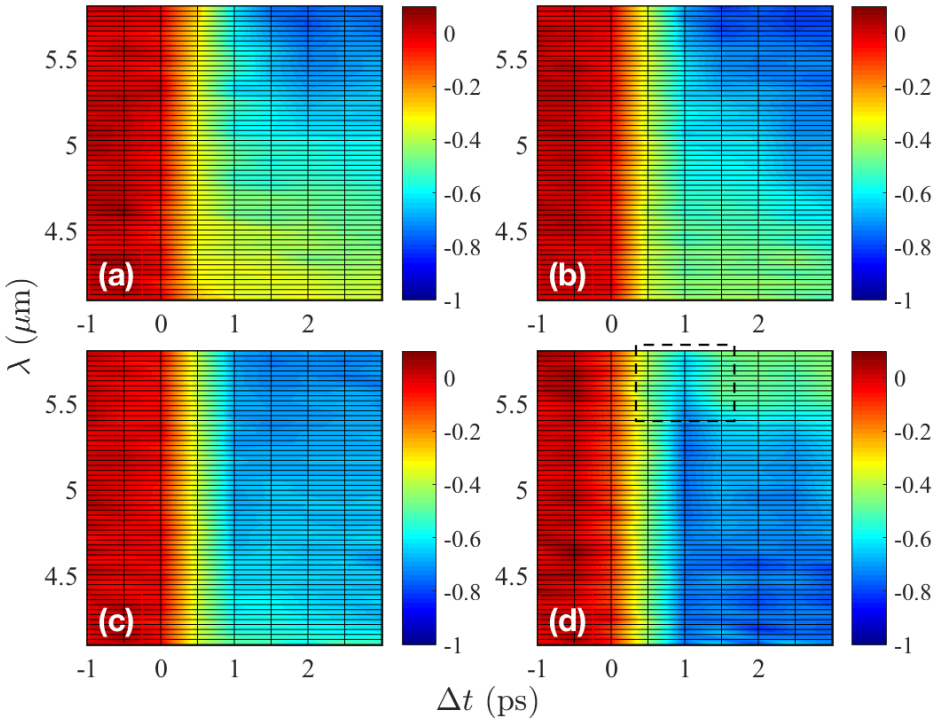


Figure 5.2: The change of the reflectance, $\Delta R/R_0$, as a function of the arrival time difference, $\Delta t$, between the pump and signal pulses, and the signal wavelength $\lambda$ for the pump fluences of 3.8 mJ/cm$^2$ (**a**), 5.0 mJ/cm$^2$ (**b**), 6.3 mJ/cm$^2$ (**c**) and 8.8 mJ/cm$^2$ (**d**). The dashed box in (**d**) shows the region where the reflectance passes through the minimum.

### 5.1.3 Demonstration of the Ultrafast Switching

Using the optical model shown in Chapter 2 and 4, the condition for the demonstration of the ultrafast switching was optimised, which can be operated at a speed far faster than the natural or enhanced decay processes in semiconductors related to trap states, surface recombination and Auger decay [178, 179, 180, 181, 182, 29]. As an example of such a design, the reflective modulation of the signal at 4 μm is shown in Figure 5.3. This wavelength was also chosen because of its importance for imaging and range-finding at MWIR [158].

The performance of the modulator, demonstrating the contrast reaching 30% and

the response time (as defined by the FWHM) of 0.55 ps, is shown in Figure 5.3(a). It surpassed an electro-optical reflective modulator based on a non-linear response of the surface plasmons [183]. It is noted that small oscillations of $\Delta R/R_0$ for $\Delta t > 1$ ps were due the experimental noise and cannot be routinely reproduced. Figure 5.3(b) shows the related temporal development of the real and complex parts of the effective dielectric function, $\Re(\epsilon_{eff})$ and $\Im(\epsilon_{eff})$, following the excitation by the pump pulse. Besides, Figure 5.3(c) shows the density of the carriers, $N$, and their scattering rate, $\gamma$, which transpired from the simulation of the experimentally-determined temporal evolution of $\Delta R/R_0$. The simulation itself is shown in Figure 5.3(a) as the black dashed line.

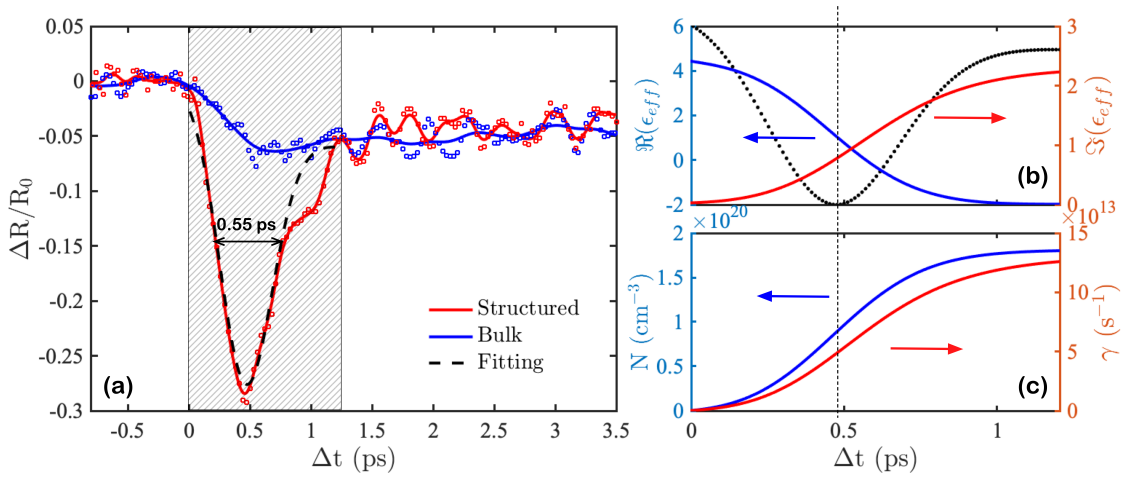


Figure 5.3: (**a**) The change of the reflectance $\Delta R/R_0$ as a function of the arrival time difference, $\Delta t$, between the pump and signal pulses, for a pump fluence of 10 mJ/cm$^2$. The solid blue, red and dashed black lines are the experimental results for the bulk, mp-Si silicon and the best fitting, respectively. (**b**) The evolution of the real (blue) and imaginary (red) part of the dielectric function as a function of $\Delta t$, reconstructed from the experimental data. The black dashed curve reproduces that shown in Panel (a) to assist with the interpretation. (**c**) The variation of the carrier concentration $N$ (blue) (at the sample surface) and scattering rate $\gamma$ (red) as a function of $\Delta t$. The vertical dotted line indicates the condition of $\epsilon \to 1$ when the reflectance reaches its minimum.

Bulk silicon response was measured to compare its performance with that of the mp-Si membrane. In the absence of the pumping, the mp-Si and bulk silicon had reflectances of 0.2 and 0.3, respectively. It was apparent that for identical optical pumping, the response $\Delta R/R_0$ of the bulk silicon and mp-Si was quite different. The bulk material did not show a sharp negative peak, but rather dropped and remained constant. In addition, the modulation contrast was just above 5%. This is because compared with mp-Si, bulk silicon has a higher dielectric constant and requires a higher carrier concentration to shift the plasma edge to 4 $\mu m$, and only near the plasma edge, the reflectance will change drastically.

To explain the sharp peaked response and enhancement in the modulation contrast, it will be helpful to investigate the development of $\Re(\epsilon_{eff})$, $\Im(\epsilon_{eff})$, $N$ and $\gamma$ as a function of time shown in Figure 5.3(b) and (c); Panel (b) also reproduces the reflectance response $\Delta R/R_0(t)$ as the dashed line for the convenience of the discussion. It can be seen that following the pump pulse application, the carrier density increased, causing a decrease of $\Re(\epsilon_{eff})$ and, alternatively, an increase of $\Im(\epsilon_{eff})$. Yet at the earlier times, the main contribution to the reflectance change was from the variation of $\Re(\epsilon_{eff})$, as $\Im(\epsilon_{eff})$ was still too small. Around 0.5 ps, $\Re(\epsilon_{eff}) \to 1$, at which $\Delta R/R_0$ reached the minimum, and its value was set by $\Im(\epsilon_{eff})$ at this time. That is, higher $\Im(\epsilon_{eff})$ resulted in lower contrast of $\Delta R/R_0$. After 0.5 ps, the rate of $\Delta R/R_0$ and its sign were determined by the the combined contribution of $\Re(\epsilon_{eff})$ and $\Im(\epsilon_{eff})$ as they have comparable absolute values. The steady state condition of $\Delta R/R_0$ was reached after 1 ps when both the real and imaginary parts were saturated, on par with $N$ and $\gamma$.

To summarise, initially, the rate of $\Delta R/R_0$ drop was almost exclusively governed by the decrease of $\Re(\epsilon_{eff})$; the minima was achieved when $\Re(\epsilon_{eff}) \to 1$; and the modulation contrast was determined by $\Im(\epsilon_{eff})$. The $\Delta R/R_0$ recovery rate was determined by the combination of the development of both $\Re(\epsilon_{eff})$ and $\Im(\epsilon_{eff})$ as a function of time, and their

values determined the level at which $\Delta R/R_0$ would saturate. It is noted that the carriers did not recombine during this short time period, and therefore, the modulator switching speed did not depend on the recombination process. However, the modulator operation/repetition frequency was limited by the recombination time required for the modulator to return to the unexcited state before the next switching event happened. In Chapter 4, it was found that the complete recombination of the excited carriers occurred on the nanosecond time scale [184].

## 5.2 Demonstration of Time-of-Flight technique with Macro-Porous Silicon

### 5.2.1 Experiment

The experimental set-up is almost identical to that introduced in the Section 5.1.1. However, the probe wavelength covers the range between 2.1 and 3.5 μm instead of 4 — 6 μm. The spectral range in these experiments is limited by the transmission window of the silica rods used for stretching the signal pulse. In particular, at wavelengths shorter than 2.1 μm the signal is absorbed by -OH vibrating groups found in silica, while the cut-off wavelength longer than 3.5 μm is related to IR-active absorption of Si-O bond[185]. In-between those wavelengths the rods are semitransparent for the signal. More detailed information about the system can be found elsewhere[29, 40, 114]. To construct the Time of Flight (ToF) set-up, the arrival times of the 800 nm pump and SWIR/MWIR signal pulses have to be synchronised. The synchronisation of the optical set-up is shown in Figure 5.4.

The diagram shows optical paths of the pump and signal pulses. The red line designates the pump whose arrival time at the mp-Si membrane (3) can be changed by

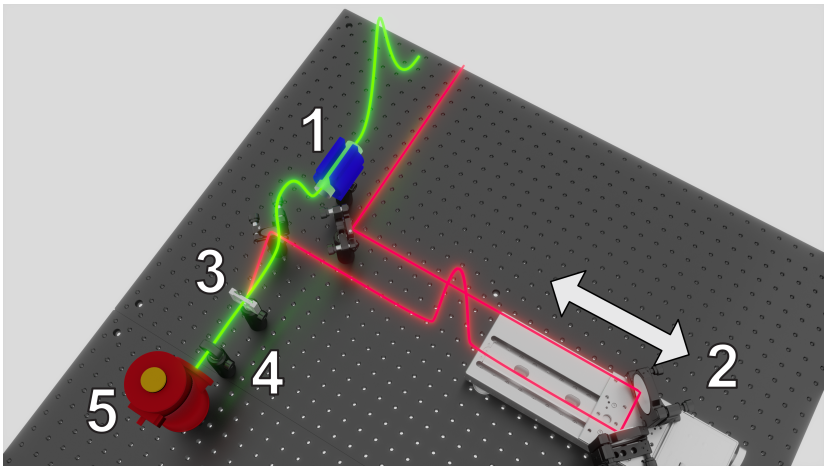


Figure 5.4: ToF feasibility demonstrator. Green and red lines show schematically the optical paths of the signal and pump pulses, respectively. (1) 5 or 10 cm silica rod aimed to stretch the signal pulse delivered by the OPA; (2) retroreflector mounted on a translational stage synchronising the arrival of the pump and signal pulses at the surface of the tunable optical modulator (3); (4) longpass filter blocking the pump; (5) MCT detector.

a retroreflector mounted on a computer-controlled translational stage (2). The green line marks the signal pulse delivered by the OPA. The signal passes through a silica rod (1), which delays and stretches the pulse, before it traverses to the optical modulator (mp-Si). After the modulator, any unabsorbed pump light that is transmitted through the membrane is rejected by a longpass filter (4), allowing only the probe signal to pass through. The signal is detected by a Teledyne Judson J15 photoconductive MCT detector (5) connected to a lock-in amplifier.

### 5.2.2 Results and Discussion

To set-up the ToF measurements, the silica rod was initially removed from the signal's optical path and the position of the retroreflector was adjusted in such a way that the

pump and signal pulses arrive simultaneously on the surface of the mp-Si, that is when the membrane is activated and the transmission of the signal is suppressed. This position can be regarded as the relative zero-distance and it is nearly identical for all wavelengths of the signal, as the dispersion of air is insignificant to change the speed of light and the arrival time of the pulse at the surface of the membrane. After the silica rod was inserted into the path the ToF of the signal is delayed, because the propagation speed slows down inside the rod. The position of the retroreflector was readjusted accordingly to add an additional distance $D$ to the optical path of the pump for compensating the added ToF in the optical path of the signal. At this new position the pump and signal again arrive simultaneously on the surface of the membrane, blocking the passage of the latter. This procedure was repeated for different wavelengths and lengths of the rod. In such way, by scanning the retroreflector position, a ToF delay with respect to the zero position, induced by the rod, can be found as:

$$ToF = (n(\lambda) - 1)\frac{L}{c} = \frac{D}{c}, \tag{5.1}$$

where $n(\lambda)$ is the wavelength-dependent refractive index of the rod, $L$ is the length of silica rod and $c$ is the speed of light in vacuum.

Figure 5.5 summarises the results showing the signal intensity as a function of the distance $D$ added to pump optical path (bottom $x$-axis) and the corresponding ToF (top $x$-axis). The blue dots show the signal travelling along the optical path without passing through the rod. The green and red dots demonstrate the delay of the ToF due to the insertion of 5 and 10 cm long rod, respectively. (It should be noted that silica has very poor transmission beyond the wavelength of 3 µm, thus it was not possible to use the 10 cm silica rod.) It can be seen that the insertion of the 5 cm long rod delays the ToF by about 75 picoseconds (this time depends on the wavelength because of the silica rod dispersion). This time gets longer when the rod length is increased twofold to 10 cm, as

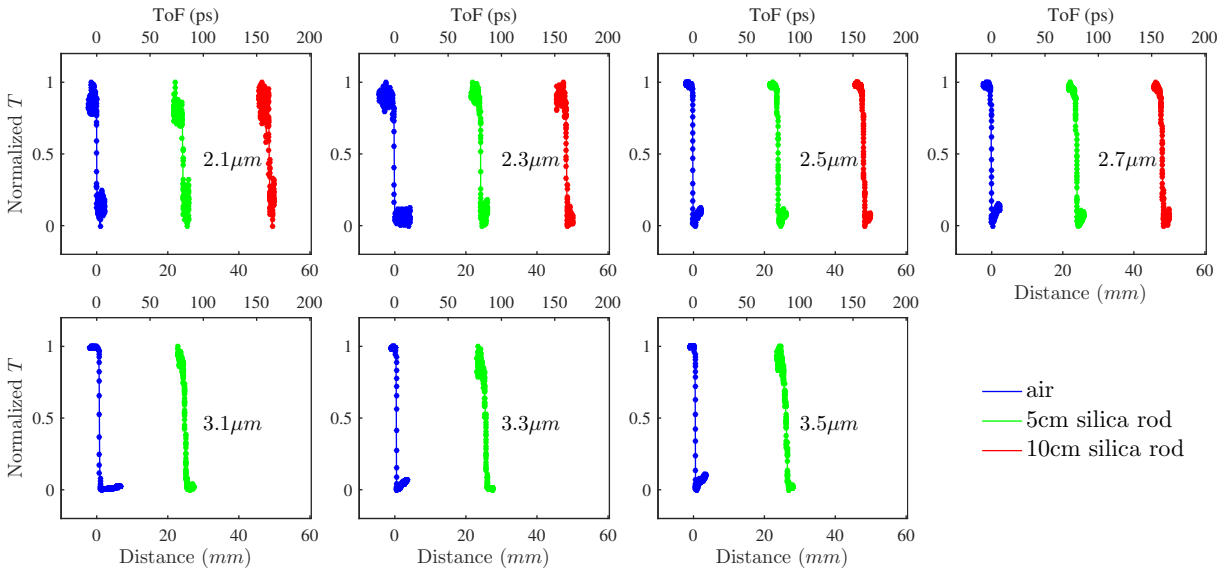


Figure 5.5: Normalised intensity of the transmitted signal at different wavelengths in the range between 2.1 and 3.5 μm. Blue represents the result of the signal passing through free space without a silica rod; green - with a 5 cm rod; red - with a 10 cm rod.

shown by the red dots.

However, the ToF demonstration is not limited to the measurements of the arrival times, it can be further expanded to show that the set-up can be used to measure the GVD of the silica rod from the analysis of the probe waveform. Figure 5.6 shows the normalised intensity of the transmitted probe at selected wavelengths in the range between 2.1 and 3.5 μm as a function of time between the probe and pump. In fact the data can be viewed as similar to that shown in Figure 5.5, but presented at higher resolution and shifted on the time-scale to overlap the dropping edges for easier comparison. The point of such presentation is to show the probe pulse stretching after propagation through the rod in comparison to that passing through free space. The measurements of the probe pulse stretching at each wavelength was preceded by evaluation of the membrane temporal response (shown as blue dots). This was done by recording the signal transmitted by the

membrane as a function of the delay time between the pump and signal pulses without the silica rod in the optical path. The temporal response curve comprises of three regions corresponding to: negative time when the signal arrives before the pump pulse and when the membrane is nearly fully transparent; around zero-delay when the arrival time of both pulses is almost coincident and when the transmittance of the membrane is rapidly suppressed by the pump excitation; positive time when the signal arrives after the pump and when the membrane is not transmitting the signal. The temporal resolution of the ToF is determined by the second region, that is the time during which the transparency of the membrane switched between the two states of transmitting or rejecting the incoming signal. It can be seen from Figure 5.6 that the response time is below 100 femtosecond and nearly independent of the wavelength. Because the response time is set by the speed of the excitation, It can be concluded that the excitation by the pump is an instant process and that the rising edge of the pump pulse governs the speed of the membrane modulation. At the positive times, the membrane's transmittance tends to return to its original state. However, the observation and measurements of the full recovery is not shown in this work as it happens on much longer time scales of a few hundred picosecond, as was reported previously by my earlier work[184].

Figure 5.6 shows that the signal response is stretched from an "instantaneous" to a few picoseconds long response when a silica rod of 5 or 10 cm long, green and red lines, respectively, is inserted into the optical path (see Figure 5.4). The observed broadening of the signal response curve is a result of the dependence of the group velocity on the frequencies traversing through the rod, that is GVD is responsible for stretching the probe pulse emerging from the rod. The duration of the stretched pulse, $\tau$, is related to the original pulse as the following[186]:

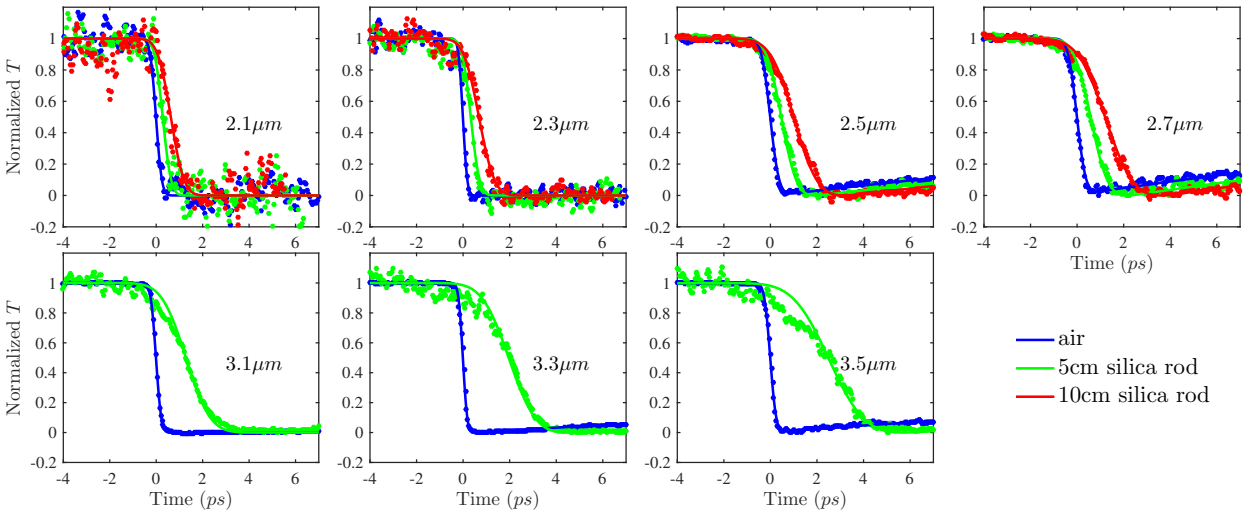


Figure 5.6: Normalised intensity of the transmitted signal at wavelengths ranging from 2.1 to 3.5 μm. The dots represent the raw measurements and the solid lines show their smoothing. Blue colour represents the result of the signal passing through free space without a silica rod; green - with a 5 cm rod; red - with a 10 cm rod.

$$\tau(\omega) = \tau_0 \sqrt{1 + \frac{8a(\omega)Lln2}{\tau_0^2}}, \tag{5.2}$$

where $\tau_0 = 100$ fs is the duration of the pulse before entering the rod; $L$ is the rod's length; $a(\omega) \equiv \frac{1}{2}\frac{d^2k}{d\omega^2}$ is a frequency-dependent parameter related to GVD of the silica rod, where the wave-vector, $k$, depends on a frequency, $\omega$, according to a dispersion relation of silica. The following shows that the parameter $a(\omega)$ can be reconstructed from the ToF measurement shown in Figure 5.6.

The signal recorded by the MCT detector can be presented as a convolution of the system response function $g(\omega; t - t')$ with the signal pulse after the rod $f(\omega; t')$[187]:

$$(f(\omega) * g(\omega))(t) \equiv \int_0^\infty f(\omega; t')g(\omega; t - t'))dt'. \tag{5.3}$$

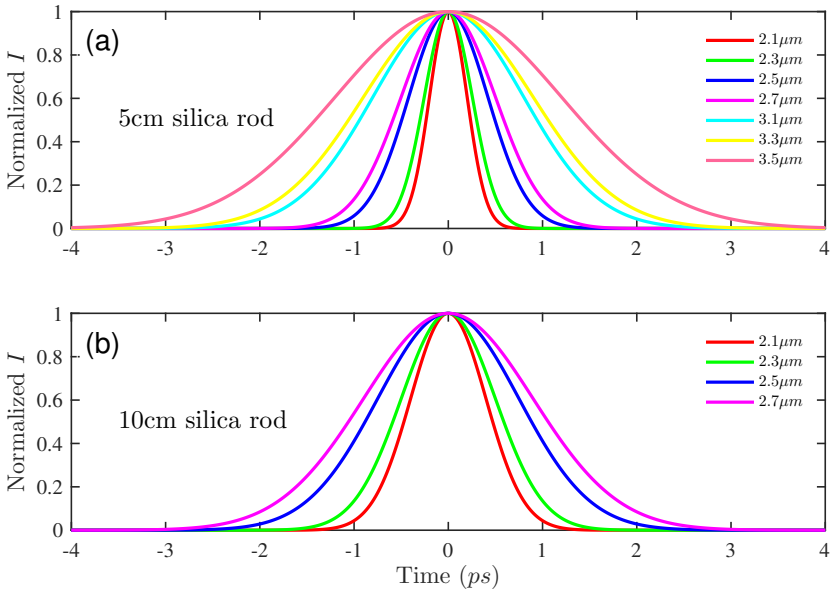


Figure 5.7: The signal pulse after silica rod as reconstructed by the deconvolution procedure. (a) and (b): for 5 and 10 cm long silica rods, respectively.

Because the response function, $g(\omega;t)$, is known (shown as the blue line in Figs. 5.6), the signal pulse emerging from the rod, $f(\omega;t)$ can be reconstructed using a deconvolution procedure[188]. For the deconvolution the smoothed results were used, shown as the solid lines, to avoid problems related to the noise present in the input functions. The reconstructed pulse is shown in Figs. 5.7 for different signal frequencies and rod lengths. It can be seen clearly by comparison of Figure 5.7(a) and (b) that the pulse duration increases as the length of the rod was doubled. As well, the pulse broadens as the wavelength increases as expected for silica, a material with negative chromatic dispersion at this wavelength range[189].

Furthermore, using Eq.5.2 the GVD parameter, $a$, was calculated which is shown in Figure 5.8(b) besides the corresponding pulse duration (Figure 5.8(a)). To confirm the validity of this result it is informative to compare them to the literature. However, the

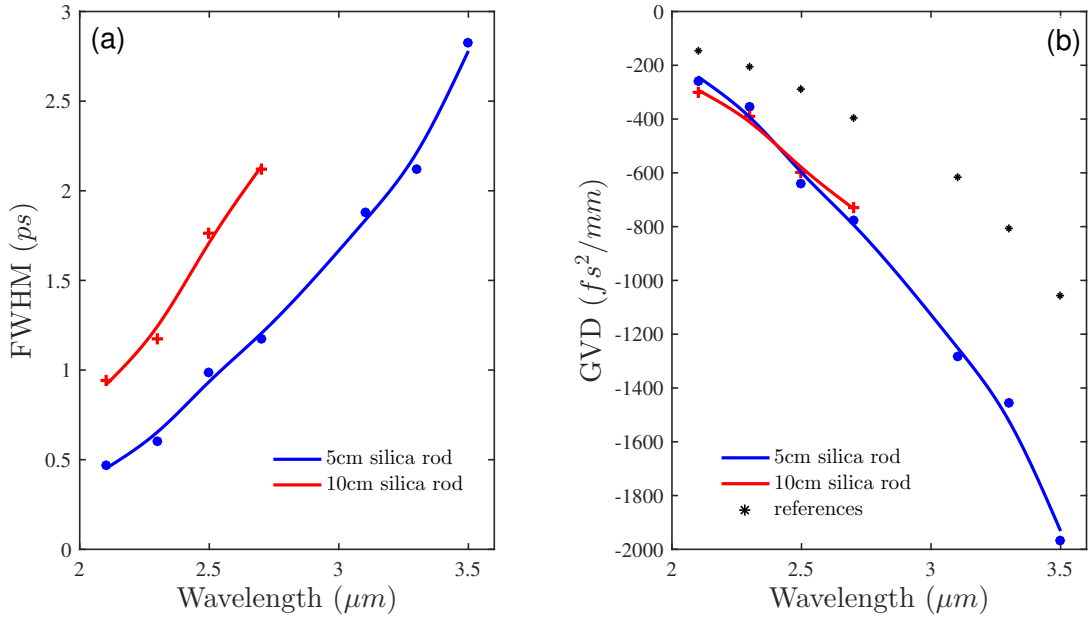


Figure 5.8: (a): the duration of the 100 fs pulse after stretching by the 5 and 10 cm long silica rods, blue and red dots, respectively. (b): The GVD of silica, red and blue dots are measured in this work using ToF method, black - taken from the references[189, 190, 191]. The lines are shown to guide the eye.

published data has very limited information on GVD in the SWIR/MWIR range measured by the ultrafast pulses. Thus, it was restricted to judge the extrated GVD in this work against those made with a Continuous Wave (CW) source published elsewhere[189, 190, 191]. It can be seen that the ToF measurements using the ultrafast light laser reproduce well qualitatively the GVD which tends to increase as a function of the wavelength. However, the values obtained are greater by a factor of $\sim$2.5 in comparison to the CW results. At this stage, it is not clear whether the discrepancy arises from significantly different light sources or dissimilarity of silica materials used in the compared studies.

In summary, this chapter discusses the potential of using mp-Si as the material of an MWIR all-optical modulator and its application in ToF. The pump beam was used to "switch" the modulator between on and off states, while the probe beam was used to detect the changes in the reflectivity of mp-Si. By varying the pump intensity and pump-probe arrival time difference on the mp-Si surface, more than 80% of modulation was achieved. In addition, a fast response scheme was developed by taking advantage of the plasma edge of mp-Si under intense pump illumination. A 30% change of the reflected signal was obtained, and the signal recovers within 0.55 ps. This scheme can benefit applications that require extremely fast switching speed. Based on the understanding gained from these experimental results, a ToF set-up with the all-optical modulator as the core component was constructed. This set-up has a temporal resolution of about 100 fs, sufficient to monitor subtle effects such as pulse broadening due to the group velocity delay in media. To demonstrate this, silica rods with 5 and 10 cm lengths were placed in the probe optical path to stretch the pulse, and the GVD coefficients were extracted from the experimental results. The obtained GVD coefficients are consistent with the literature, which proves the accuracy of the ToF setting.

# Chapter Six

# Gold Nanoplasmonic Particles in Scaffolding of Porous Silicon — Ultrafast Carrier Dynamics and Applications in SERS

**This chapter is a reformatted version of my papers: 1. 'Localized Plasmon Field Effect of Gold Clusters Embedded in Nanoporous Silicon', R. Wu, T. Mathieu, C. J. Storey, Q. Jin, J. Collins, L. T. Canham, A. Kaplan, Advanced Optical Materials, 9(9), 2002119; 2. 'Gold nanoplasmonic particles in tunable porous silicon 3D scaffolds for ultra-low concentration detection by SERS', R. Wu, Q. Jin, C. J. Storey, J. Collins, G. Gomard, U. Lemmer, L. T. Canham, R. Kling and A. Kaplan, Nanoscale Horizons (2021).**

Localised Surface Plasmon (LSP) is a coherent oscillation of electrons at the interface between metallic nanoparticles and the surrounding medium. LSP can be excited by light when its frequency matches that of the oscillations, producing a strong enhancement of the

electromagnetic field in the vicinity of the particles at the conditions of the resonance[192]. The LSP Resonance (LSPR) is distinguished by intense absorption and scattering of light. Its wavelength and intensity are primarily determined by the type of material, size, shape, environment refractive index and the coupling between adjacent nanoparticles [193, 56, 194]. Over the past few decades, extensive studies have been conducted to assess the viability of using LSPR in biological and chemical sensing systems due to its high sensitivity to the surrounding environment[195, 196]. The ability of photon-trapping and strong absorption of LSPR at resonance wavelength have further promoted its implementation in light harvesting devices[57, 197]. Other fields of research and applications extends to metamaterials [198], plasmonic devices[199, 200], diagnosis and treatment of diseases[201, 202, 203].

Different types of LSPR substrates with nanoparticles in colloidal suspension, deposited on the surface and embedded in dielectric matrix have been developed and investigated[204, 205, 206]. The former two types are most commonly used in biological and chemical sensing systems, implementing Surface Enhanced Raman Spectroscopy (SERS), where the analytes are either mixed with colloidal solution or in contact with the substrate surface[207]. The LSPR induced by nanoparticles localises and enhances the electromagnetic field which amplifies the Raman signal of the surrounding molecules[208]. In the latter type, metallic nanoparticles are usually embedded into nonconducting solid state environment, such as silicon oxide or organic polymers[209]. These hybrid composite materials not only preserve the LSPR response of the metal nanoparticle from degradation, but also improve the robustness and responsiveness, thereby further expanding their application range. In particular, the combination of nanoplasmonics with semiconductor technology develops a new class of electro-optical materials that not only have attributes of both components, but promises to exhibit new properties, which would be difficult to achieve using each component separately. Optimized coupling between nanoplasmonics

and semiconducting materials can enhance and complement the efficiency of almost all semiconductor technologies of lasers, solar cells, detectors, sensors, imaging and electronics. It has been demonstrated that introducing the nanoplasmonics local fields into semiconductor devices enhances the light coupling to nanowires[210, 211], increases photocurrent in germanium detectors[212], provides means for terahertz all-optical switching[213], enables sub-gap detection using gold nano-antennas on silicon[214], produces large non-linearity in epsilon-near-zero material[215] and metasurfaces[216].

Despite considerable research interest and technological impact, the tailored fabrication of a composite material, comprised of a semiconductor with *embedded* plasmonic nanoparticles, remains a formidable challenge. The conventional mixing techniques used for combining non-conductive dielectrics with metal particles — such as sol-gel, melt-quenching[217], metal-dielectric co-sputtering[218], metal-ion implantation and pulsed laser deposition, have not been developed to a satisfactory level for semiconductor/metal composites to assure uniformity over metal particles size and density. The lack of the established fabrication techniques hampers the investigation of the plasmon field influence on the charge carrier generation, distribution, decay, and linear and non-linear properties in the semiconductors with embedded clusters supporting the Localised Surface Plasmon (LSP) field.

This Chapter's work attempts to resolve this deficiency by developing a method to fabricate nanoplasmonic-semiconductor composite with the scalability for the production of large quantities of nanoplasmonic-semiconductor composites exhibiting high uniformity. Nano-porous silicon (np-Si) was selected as the semiconductor matrix due to its low manufacturing cost[35], robustly developed fabrication process and in-depth documented optical and electronic properties[29, 219]. Moreover, np-Si provides a natural template for metallic nanoparticle growth inside the interconnected nano-sized pore channels. A method of spontaneous growth of Au nanoparticles (AuNPs) inside np-Si using the immersion

plating technique was developed. Although this method is not new, the vast majority of former works employed it to pin metallic particles to the surface. This study is different in that the optical properties and effects of the LSP excitation were investigated for a composite semiconducting material with metallic particles embedded uniformly across its volume. Embedding particles in the volume allows more degrees of freedom to design applications and provides a more versatile model to investigate mutual LSP-semiconductor interaction. Importantly, the excitation of nanoplasmonic particles distributed over the volume is more efficient than those pinned to the surface, because a higher amount of clusters can be exposed to a given light flux propagating through a slab. Moreover, a composite made of a material with an enormous surface-to-volume ratio, such as nanoporous silicon[35] with gold clusters embedded inside of it presents benefits to Surface Enhanced Raman Spectroscopy. Compared to the more conventional Raman substrates, the number of metal clusters available to enhance the signal will increase by a few orders of magnitude and, in addition to analyte molecules on the surface, there will be an extensive (perhaps even dominant) contribution from those interacting with gold clusters in the pores. Note, that a small fraction of clusters in the pores is unlikely to prevent the diffusion of a solution with analyte over the entire volume of a slab. Nanoporous silicon channels are densely intertwined with a multitude of crossing points where the solution can bypass any passages blocked by clusters.

The impregnation of AuNPs demands precise control of the solution temperature and concentration to ensure uniform growth of Au particles inside the pores, while concurrently minimising unwanted particle clustering on the np-Si facets. Samples with different volume fractions of Au nanoparticles were fabricated and their composition, morphology and uniformity were examined by means of Scanning Electron Microscopy (SEM) and Transmission Electron Microscopy (TEM). The results show that the nanoparticle size and density distribution can be controlled by varying the deposition time and solution

concentration. The presence of the LSPR was observed by Dark-Field Microscope and a VIS-NIR scattering spectrometer. Au/np-Si composites exhibit the LSPR at the red end of the visible spectrum, extending to the near infrared region for the samples with increasing Au nanoparticles volume fractions. The sample with the highest Au volume fraction was used as a SERS substrate to measure the Raman spectrum of Methylene Blue (MB) benchmark compound. An enhancement factor of $\sim 10^9$ was demonstrated under the excitation wavelength of 808 nm in the vicinity of the LSPR. Such an enhancement is suitable for a scenario where single molecule detection is desired[220, 221].

In addition, the linear and non-linear properties of the np-Si/Au composites were investigated by optically pumping the samples at the LSP resonance, and probing the optical response and its evolution in time with Short Wavelength Infra-Red (SWIR), 2.5 μm, light. This is in contrast to many cases where the electro-optical response of the composites is investigated at or near the LSP resonance. This work not only focuses on the resonance excitation, but also combines the simultaneous LSP excitation with electro-optical response that was probed in SWIR, away from the resonance. Such approach is useful to decouple the probe beam from the excitation and help to gain insight into the physics of the LSP-semiconductor interaction, dynamics of the resonance and develop applications. The results show that the off-resonance extinction of SWIR light propagating through the composite depends linearly on the intensity of light exciting the LSP, as well as on the metal volume fraction. A combination of these two parameters allow the freedom to pre-design a thin-film absorber and alter its optical properties on demand by the LSP excitation - an extremely useful quality in the all-optical switching.

The SWIR non-linear response of composites was also investigated and a strongly enhanced nonlinear response by the LSP excitation was revealed. Such unique LSP-induced non-linear properties make the material an excellent candidate for a number of electro-optical applications based on the intrinsic refractive optical bistability. The usefulness

of such materials for displays, spatial light modulators, optical image processors, and optical computational elements are known for the decades, in particular in optical elements based on the non-linear Fabry-Perot filters[222]. The composite of porous silicon with the volume fraction of gold of 0.13 in the presence of the LSP excitation nearly five-fold enhances the non-linear refraction with a comparable decrease of the extinction in the SWIR, paving a way to design the active silicon photonics applications with this new class of materials. It was found that the recovery of the nonlinear response is rather limited by a few femtosecond relaxation time of the LSP excitation as the non-linear excitation closely follows the temporal profile of the pump. The ability to modulate the optical response extremely fast makes the material suitable for all-optical switches/modulators[223, 49] and Semiconductor Saturable Absorber Mirrors (SESAM's) (the recovery time should be faster than the cavity round trip and non-saturable losses should be small) [224, 225].

## 6.1 Sample Preparation and Characterisation

A wet chemical synthesis method was adopted based on the previously reported works[226, 227] which exploring gold ions reduction from a solution of Tetrachloroauric Acid ($HAuCl_4$) with borohydride as a reducing agent. However, in this work, no reducing agent was required. Instead, hydrogen atoms chemisorbed at the pores surface of np-Si act as a reducing agent during AuNPs impregnation. Detailed description of the impregnation method can be found in Chapter 2. Figure 6.1(a) illustrates the main steps of the samples preparation. A 550 nm thick np-Si layer with underlaying silicon substrate was pre-treated with 2% HF solution for 30 s to remove the native oxide from the pores surface and to saturate dangling bonds with hydrogen. After the treatment, the samples were immediately immersed in $HAuCl_4$-ethanol solution, where the gold ions' reduction occurs at the pore channel surfaces accompanied with aggregation and spontaneous growth of AuNP. To

Table 6.1: Parameters and sample information of Gold ions reduction process: $HAuCl_4$ solution concentration, $c$; immersion time, $t$; and Au volume fraction, $f$.

| Sample | c (mM ) | $t(min)$ | $f$ |
|---|---|---|---|
| Au/np-Si 1 | 0.5 | 10 | 0.02 |
| Au/np-Si 2 | 1 | 20 | 0.05 |
| Au/np-Si 3 | 1 | 120 | 0.08 |
| Au/np-Si 4 | 1 | 720 | 0.13 |

facilitate the penetration of the solution into the pores, an ultrasonic bath was used during immersion, which not only enhances the inflow, but also prevents the growth and clustering on the top surface. In addition, the solution concentration and environment temperature play important roles in achieving uniform Au deposition along the depth coordinate. Due to a slow diffusion rate of solution in np-Si ($\sim 10^{-9}$ — $10^{-10}$ $m^2/s$)[35], AuNPs tend to grow in the direction from the top to the bottom of the substrate. Therefore, controlling the reduction rate through concentration and temperature are essential to ensure the solution reaches the bottom before AuNPs grows at the top, blocking the opening of a pore channel. Through iterative experimentation, it was found that at the room temperature, the diffusion and reduction rates are balanced for $HAuCl_4$ concentrations no greater than 1 mM. Samples with different densities and sizes of AuNPs were obtained by varying the $HAuCl_4$ concentration and retention time of np-Si in the solution. Table 6.1 shows the details of the concentration and immersion time of the four samples that were further investigated in this work. The quoted AuNPs volume fractions, $f$, were estimated by modelling the results obtained from angle resolved reflectance measurements. After the immersion plating, the samples were rinsed in pure ethanol and gently air dried on a hotplate at 60 °C.

A layer of processed np-Si was gently fractured into small fragments to examine under

TEM and Energy-Dispersive X-ray (EDX) to verify the presence of AuNPs. Figure 6.1(b) shows the TEM image of an arbitrary segment of the composite. The dark spots are the AuNPs surrounded by the bright sponge of the np-Si matrix. It can be seen that some of the pores are fully occupied by Au, while others remain hollow. Figure 6.1(c) shows the EDX spectrum of np-Si after the Au impregnation. The pronounced Au and silicon peaks are clearly observed at their characterisitic energies of 2.12, 9.71 and 1.74 eV, respectively[228, 229]. It is noted that the carbon and copper peaks are contributed by the supporting TEM grid.

To demonstrate the uniformity of the clusters distribution along the sample depth, the top-view and cross-section SEM images are shown in Figure 6.1(d) and 6.1(e), respectively. These results confirm that there is no aggregation of particles on the top surface, while they are evenly spread along the depth of the 550 nm thick np-Si matrix. Figure 6.1(f) shows the zoomed-in view of the SEM cross-sections for four samples with different AuNPs volume fraction, $f$. It can be seen that both the size and density of AuNP increase with the immersion time (concluded in Table 6.2), while at the longer immersion times the larger clusters tend to grow anisotropically along channels and form rather elliptical shapes. This preferential direction of the growth is imposed by the pore channels walls. By analysing a large number of the SEM cross-section images, the AuNP clusters cross-sectional area distribution was obtained as shown in Figure 6.1(g). In addition, the ellipsoidal quadratic mean radius, $\bar{R}$, as a function of Au volume fraction, $f$, are shown in Figure 6.1(h). These figures indicate a general correlation that the clusters grow larger as Au density increases.

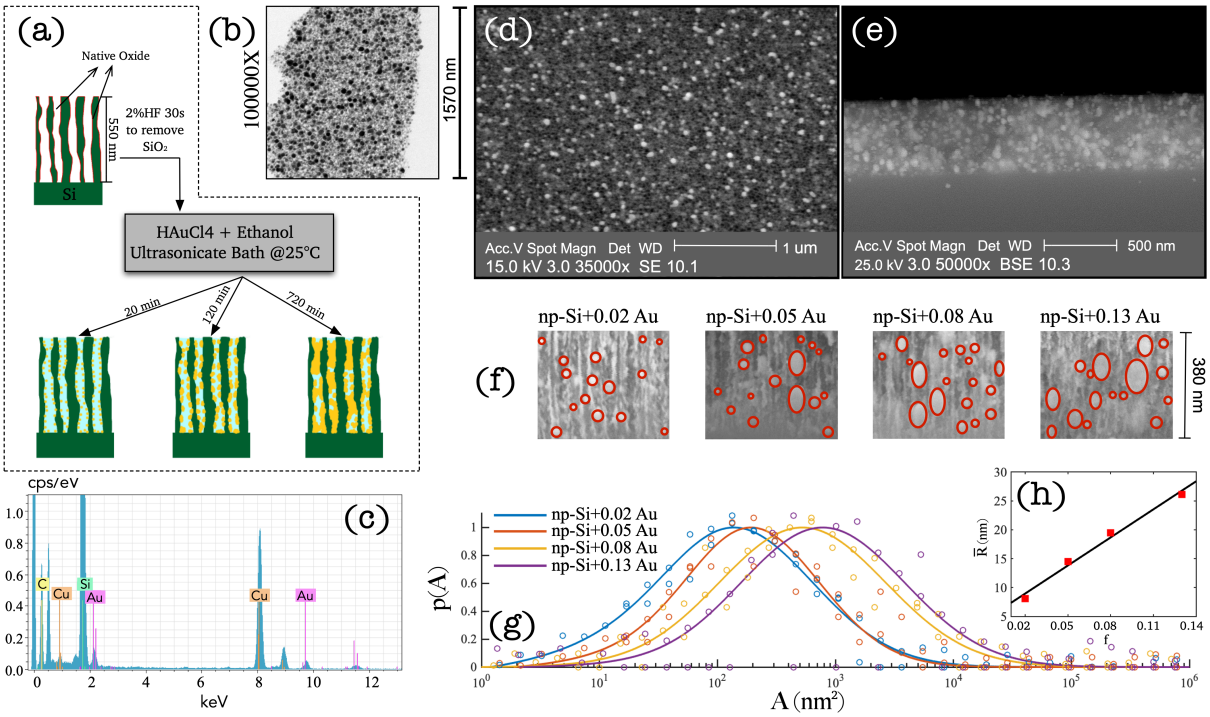


Figure 6.1: (a) Schematical presentation of the fabrication procedure of the Au/np-Si composite material; (b) TEM image of a fragment of Au/np-Si; the dark spots are AuNPs and bright area is np-Si; (c) EDX spectrum of the Au/np-Si composite; (d) top and (e) cross-section views of the reprsentative SEM image; (f) Zoomed-in cross-section of SEM images for samples with different Au volume fraction, $f$; (g) scaled probability distribution of cross-sectional area $A$; (h) ellipsoidal quadratic mean radius, $\bar{R}$, as a function of AuNPs volume fraction, $f$.

### 6.1.1 LSPR Response

To gain further insight into the nature of Au/Si composites, their optical properties were measured and evaluated. The samples were imaged by a real-colour CCD camera through a Dark Field Microscope (DFM) collecting the scattered light. The images are shown in Figure 6.2(a)-(d) where the apparent colour of scattered light is red. This is in contrast to the typical green colour for similar size AuNPs in air[230]. This redshift is attributed to the renormalisation of the LSPR wavelength according to Fröhlich resonance condition[231] for which the Drude dielectric function of gold nanoparticles, $\epsilon_{AuNP}$, matches that of the environment according to $\epsilon_{AuNP} = -2\epsilon_{env}$. For particles in np-Si, the surrounding effective dielectric function, $\epsilon_{env}$, is nearly twice larger than that of air, resulting in the resonance conditions shifted towards longer wavelengths.

In addition to the apparent colour of the scattered light, Figure 6.2(a) to (d) confirms the conclusion inferred from the SEM results in Figure 6.1 that the number of light scatterers increases as the density of nanoparticles increases with the immersion time. Yet, the DFM observation of the scattering has limitations because the CCD camera imposes the cut-off wavelength of 650 nm and integrates the spectrum.

The deficiency was resolved by means of the wavelength-resolved light scattering measurement over an extended VIS-NIR spectral range. Figure 6.2(e) shows the scattering spectra of np-Si without and with different volume fractions of Au. The scattering spectrum of the np-Si sample without AuNPs is almost flat. This is because the roughness parameter of np-Si is governed by the pores dimensions which is much smaller than the wavelengths of the spectrum. Therefore, there are no available scattering centres able to deflect the incoming photons from the original path. However, adding just a minute Au volume fraction of 0.02 to the np-Si results in appearance of the scattering band peaking around 600 nm, attributed to the LSPR. As the Au volume fraction increases, the resonance peak

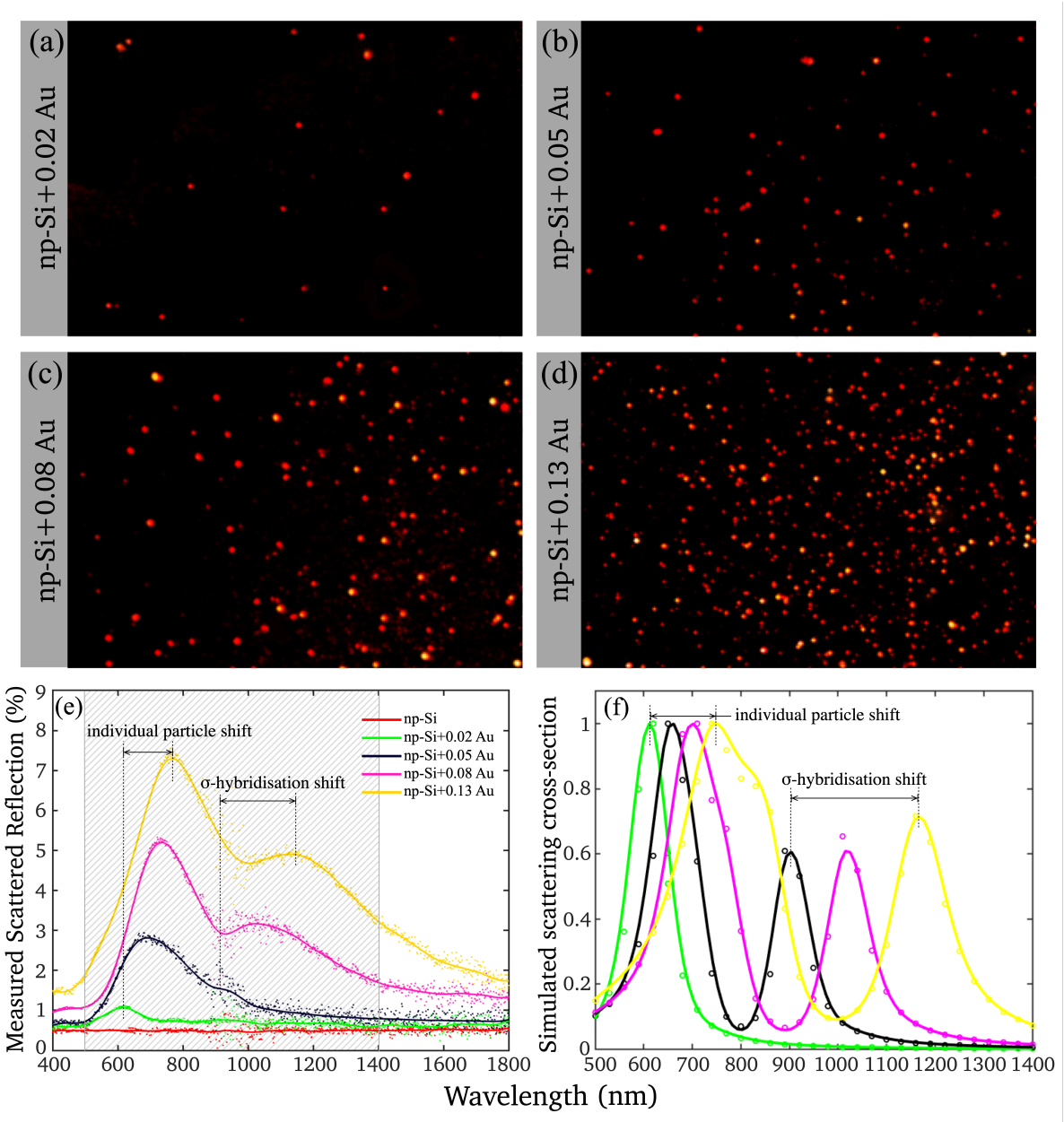


Figure 6.2: (a)-(d) Dark Field Microscope(DFM) images of the four samples with different Au volume fractions; (e) Measured scattered reflection of np-Si samples without and with different volume fraction of Au; (f) Simulated scattering cross-section (normalised) for the fitting parameters listed in Table 6.2.

further shifts to the NIR region, accompanied by the development of the second scattering band, covering the wavelength region between 1000 and 1300 nm. There are two main physical effects that are likely involved in the alteration of the spectrum by increasing the Au fraction in the material.

First, the plasmon resonance shifts towards longer wavelengths as the AuNP size increases. [232] This is very likely attributed to the change of the local environment surrounding individual particles. While a particle grows, it fills the available space expanding simultaneously towards the opposite wall and along the channel. Hence, the size of a particle determines the fractions of silicon and air in its surrounding. The smaller round particles are more exposed to air and less to silicon at the interface between the pore wall and gold. For larger particles the contact area with silicon increases because of their elliptical shape filling the channel. Hence, the larger particles are locally surrounded by the environment with a higher effective dielectric function and their LSPR wavelength shifts to red with respect to the smaller ones.

Second, the plasmon coupling between adjacent AuNPs can cause the split of the plasmon mode[233, 234]. Using the AuNPs density and mean radius, it can be estimated that for the lowest fraction, the mean spacing between adjacent AuNPs is relatively large, $> 10$ nm. Thus, for smaller particles and lower densities the interaction is diminishing, because the plasmon field decays by the factor of $1/e$ within the distance of $< 5$ nm[235]. At these conditions the AuNPs can be treated as isolated clusters surrounded by np-Si environment. However, at the greater Au volume fractions, which yield larger particles, the spacing between particles is smaller than the field extension and the coupling effect can no longer be ignored. At the larger AuNPs densities, the coupling produces an additional plasmon resonance corresponding to the $\sigma$-hybridisation of two individual AuNP particles with collinear and unidirectional fields. [233]. This mode's energy is lower than that of a single particle, because of the attractive nature of plasmon-plasmon interaction, and

it appears in the spectrum at a longer wavelength than that of an individual particle. Since the AuNPs in the matrix have rather distributed sizes and spacings, their scattering spectra are composed of weighted contributions from single and hybridised plasmon modes. It should be noted that although the spectra demonstrate a red shift as the Au volume fraction increases, the clusters' colours remain almost unchanged in the DFM images, because the cut-off wavelength and integration smear the effect.

To gain a quantitative understanding of the observed LSPR spectra, the Finite Element Method was used to simulate the scattering spectra of AuNPs embedded in np-Si environment. The simulation takes the mean radius, $\bar{R}$, and spacing, $\bar{d}$, between gold particles surrounded by np-Si as inputs. $\bar{R}$ and $\bar{d}$ were determined from the SEM images, as outlined above. The dielectric function of gold was used from the literature[236]. The effective dielectric function of np-Si environment (without Au inclusions), $\epsilon_{env}$, was estimated by use of Bruggeman model[237, 238]: $(1-p)\frac{\epsilon_{air}-\epsilon_{env}}{\epsilon_{air}+2\epsilon_{env}} + p\frac{\epsilon_{si}-\epsilon_{env}}{\epsilon_{si}+2\epsilon_{env}} = 0$, where $p$ is the volume fraction of silicon and $\epsilon_{air} = 1$. $p$ is an adjustable parameter, which accounts for the fact that $\epsilon_{env}$ depends on the size of gold particles in the pore channel, as discussed previously.

Three main assumptions were made for the simulation: 1) AuNPs are surrounded by a homogeneous environment with the dielectric function of $\epsilon_{env}$, according to the effective media approximation with adjustable parameter, $p$; 2) The refractive index of AuNPs is the same as that of bulk Au; 3) AuNPs have a spherical shape. Although, the actual shape of the particles is that of a spheroid, they are predominantly oriented with their major axis along the channels and depth coordinate. Hence, at the normal light incidence, light is polarised in the plane of the circular cross-section containing the minor axis.

The simulation results of the normalised scattering cross-section are shown in Figure 6.2(f) and the corresponding parameters of the calculations are listed in Table 6.2.

Table 6.2: Simulation Parameters

| Parameter | np-Si+0.02Au | np-Si+0.05Au | np-Si+0.08Au | np-Si+0.13Au |
|---|---|---|---|---|
| Radius, $\bar{R}$ | 8.1 nm | 14.5 nm | 19.5 nm | 26.1 nm |
| Effective Silicon Fraction | 0.4 | 0.5 | 0.55 | 0.65 |
| Environment $\epsilon$ @ 800 nm | 3.6+0.007i | 4.5+0.011i | 5.7+0.014i | 7.4+0.020i |
| Spacing, $\bar{d}$ | $>$ 10 nm | 1.3 nm | 1.25 nm | 1.05 nm |

It can be seen that the modelling essentially reproduces the spectral locations of the single particle and $\sigma$-hybridisation resonances, as well as the tendency of the former to dominate. The simulation does not include sources of the possible resonance broadening, such as AuNPs size and space distribution, deviation from the perfect spherical shape, dependence of the resonance life time on the particle size and contribution from the multipole interactions. Yet, it supports the assumption that the shift of the higher energy resonance (single particle) is proportional to the dielectric function of the effective np-Si environment. While the lower energy resonance depends on the strength of the coupling of an attractive dipole-dipole interaction as $d^{-3}$.

### 6.1.2 Np-Si/Au Composites as a SERS Substrate

To demonstrate the advantage of the Au/np-Si composites, the sample with the highest Au volume fraction, $f = 0.13$, was employed as the SERS substrate. A laser with 808 nm wavelength was applied to excite off-resonance Raman signal. Methylene Blue (MB) was used as a probe molecule, because its absorption peak is away from the excitation wavelength which minimises the parasitic luminescence background[239]. To validate the effect, the Raman spectra of the three samples consisting of bare np-Si, Au/np-Si composite without MB and Au/np-Si soaked in 1 μM MB was compared in Figure 6.3(a). All the

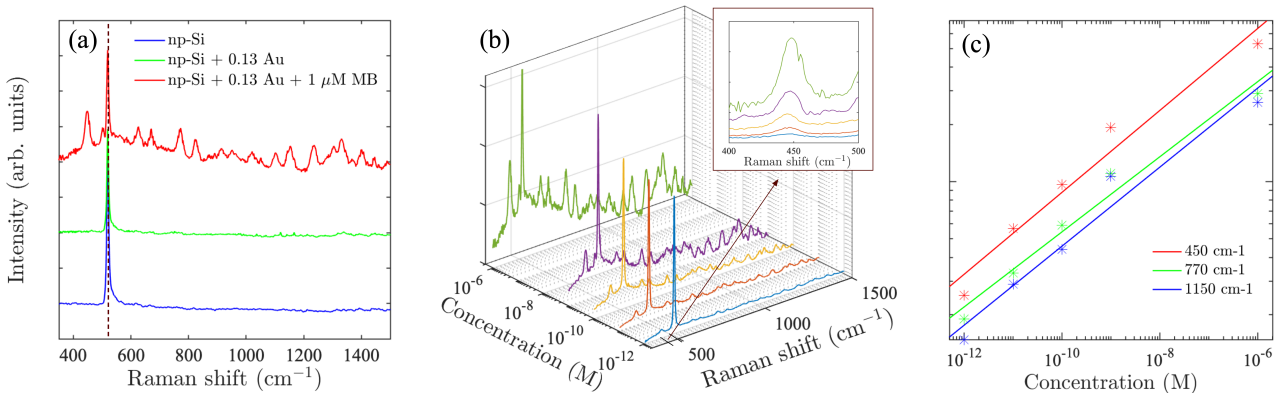


Figure 6.3: (a) Raman spectra of np-Si(blue), Au/np-Si(green) and Au/np-Si with 1 μM MB(red). The peaks marked by the dash line correspond to the TO phonon mode of silicon. The base lines of the spectra are arbitrary located on the ordinate; (b) Raman spectra of Au/np-Si with different concentrations of MB, ranging from 1 pM to 1 μM. Inset: the enlarged view of 450 $cm^{-1}$ peak; (c) Supralinear relationship of concentration and Raman intensity of three Raman peaks at 450(red), 770(green), 1150(blue) $cm^{-1}$, respectively.

samples show a strong and sharp Raman scattering at 520 $cm^{-1}$ corresponding to the intrinsic TO phonon mode of silicon[240, 241]. Besides the phonon line, the background signal for the Au/np-Si is flat and featureless providing favourable conditions to use it as a SERS platform for chemical/biological detection. This is demonstrated by the Raman spectrum of the sample with the pores filled with MB, which is recognised by the typical Raman peaks at 450, 770 and 1150 $cm^{-1}$ known from the literature[242, 243, 244, 245, 246]. It is noted that to improve the presentation, the base lines of the spectra in Figure 6.3(a) are shifted vertically.

To establish the sensitivity of the method, a series of the samples with concentration range between 1 μM and down to the ultra-low 1 pM were measured as shown in Figure 6.3(b) , with the inset of zoomed range between 400 and 500 $cm^{-1}$. It can be seen that even for the concentration as low as 1 pM, the MB scattering peak at 450 $cm^{-1}$ is still

detectable, while a further increase of the concentration makes the MB spectral fingerprints more distinct. Figure 6.3(c) shows the Raman intensity of the three representative peaks at 450, 770 and 1150 $cm^{-1}$ (located at short, middle and long spectrum region, respectively) as a function of MB concentration. It can be seen that the intensity increase for these peaks as a function of the concentration is identical. This suggests that the enhancement effect of AuNP/np-Si composite does not have spectral selectivity.

The Enhancement Factor (EF) is an important criterion to evaluate quantitatively the performance of SERS substrates[220, 221]. As discussed in the literature, there are several ways to determine the EF[247, 248, 249]. In this work, an approach that defines it as $EF = \frac{I_{SERS}/N_{SERS}}{I_{RS}/N_{RS}}$ was adopted[250]. $I_{SERS}$ and $I_{RS}$ are the Raman intensities with and without the surface enhancement; $N_{SERS}$ and $N_{RS}$ are the corresponding number of analyte molecules exposed to the beam. For the reference measurement of $I_{RS}$, a smooth Au film was used as a substrate which was uniformly covered by MB solution with a concentration of 100 mM, corresponding to $2.4\times10^{12}$ MB molecules in the area illuminated by the laser. As for the SERS measurement, there are about 24 molecules exposed to the laser at the lowest MB concentration (1 pM). The obtained SERS spectrum is shown by the blue line in Figure 6.3(b). The reference Raman spectrum was recorded while keeping the power and spot size of the excitation laser the same as in SERS measurement. The intensity $I_{SERS}$ and $I_{RS}$ was obtained by integrating the intensity of the three Raman peaks at 450, 770, and 1150 $cm^{-1}$ which yields 0.196 and 4.063, respectively (abs. unit), and the EF of $4.84\times10^{9}$. This is an ample EF value befitting the single molecule detection by SERS method[251, 220].

Typically, the EF for an isolated Au nanosphere is in the order of $10^2$ — $10^4$[252, 253, 254], which can be further improved to $10^5$ — $10^8$ by changing its shape[255], the inter-particle spacing[256, 252, 257] or distribution on a substrate[258]. The high EF for our SERS substrate can be attributed to the peculiarity of sponge-like morphological structure

of np-Si. Unlike planar substrates used in previous studies, it exhibits an enormous surface for the adsorption of the analyte[259] and to accommodate gold nanoparticles. The analyte is not only detected on a facet surface of the substrate, but, to the greater extent, across the inner surface of np-Si pore walls.

### 6.1.3 Ultrafast Carrier Dynamics

#### Linear optical properties in SWIR

The choice to use the 2.5 μm probe was made because of its applications in industry for the inspection of various products such as food produce, solar cells, electronic boards, surveillance and anti-counterfeiting, in addition to night-vision devices, imaging scenes illuminated by ambient star light. This wavelength has exquisite qualities for probing the semiconducting environment of metal-nanoclusters composites, namely: 1) the absorption and scattering efficiencies by the metal clusters are strongly suppressed because of extremely small cross-section at this wavelength, governed by the ratio of the particle circumference to the wavelength, $2\pi a/\lambda$[260]; 2) it is below a half of most semiconductors' bandgap, therefore linear absoption and Two Photon Absorption (TPA) are nearly non-existent; 3) for a strong contrast, $|\epsilon_c| \gg \epsilon_e$, between the dielectric functions of the gold clusters, $\epsilon_c = -288.7 + i14.8$[261], and np-Si environment, $\epsilon_e = 1.6$[114], the probe field is entirely located in the environment surrounding the metal clusters, while penetration into them is diminishing. Thus, the only interaction of the probe transversing the composite is with the free charge carriers and energetically accessible in-gap states of the np-Si matrix.

The optical constants in the SWIR were evaluated from the reflectance, $R_0$, measured as a function of the incidence angle for the two principal polarisations, as shown in Figure 6.4(a), for a bare silicon, np-Si substrate and np-Si with embedded gold clusters.

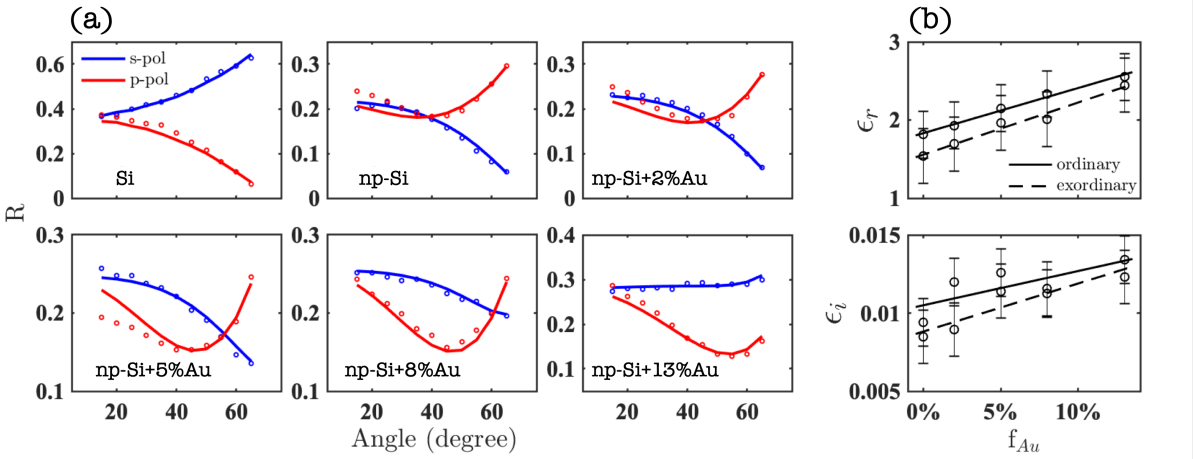


Figure 6.4: (a) the angular dependence of the reflectance, $R$, for $s$- and $p$-polarized light of 2.5 μm measured on bulk silicon (left top) and np-Si with different fraction of Au clusters, the solid lines are the model fit; (b) the effective real and imaginary parts of the dielectric function, $\epsilon_r$ and $\epsilon_i$, at 2.5 μm.

The retrieved real and imaginary parts, $\epsilon_r$ and $\epsilon_i$, of the effective dielectric function of the np-Si/Au composites and their evolution as the clusters' volume fractions increases from 0 to 13% are displayed in Figure 6.4(b). Each part of the dielectric function is contributed by the ordinary and extraordinary components arising from the weak uniaxial birefringence of the np-Si matrix. It can be seen that at the higher cluster densities, the randomness of their distribution seems to negate slightly the birefringence effect. For the evaluation of the optical constants, the Maxwell-Garnett formula was used, where the effective dielectric function of np-Si was represented as a tensor and gold clusters as isotropic inclusions. The fitting used only one free parameter responsible for the clusters' density, while the rest, for the dielectric function of gold, silicon and porous silicon, were taken from the literature[261, 175, 262, 263]. The applicability of the Maxwell-Garnett model for np-Si was tested in my previous works[114]. Figure 6.4(b) suggests that despite very large absolute values of the real and imaginary parts of the bulk gold dielectric function, their effect on the optical response of the composite is only fractional, confirming our assertion of the probe field

redistribution favourable to interact mainly with the np-Si environment and with little penetration into the clusters.

The SWIR probe pulse of $\sim$ 200 fs was used to monitor the reflectance change, $\Delta R/R_0$, as a function of time following excitation by the pump pulse near the plasmon resonance at 790 nm. Here $\Delta R = R(\Delta t) - R_0$ with $R(\Delta t)$ designating the reflectance at time difference $\Delta t$ between the arrivals of the pump and probe on a sample surface. The zero delay time, $\Delta t = 0$, is assigned to the temporary overlap of the pump and probe arrival time and where the maximum absolute change of the reflectance occurs. The evolution of time resolved spectra during the first 2 picoseconds are shown in Figure 6.5(a) for bulk silicon and np-Si with different loads of the clusters for comparison. It can be seen that all samples after the zero delay, with the exception of the bulk silicon, show a negative change. In semiconductors this indicates that the carrier (electron and hole) density increased, but the corresponding plasma frequency is below that of the probe light. The complete recovery of the signal is not shown because the excited carrier decay time is about 100 picoseconds[29], much longer than the time scales investigated here. Therefore, the recombination process and possible alteration of its mechanism affecting the observed initial signal recovery around the zero delay can be eliminated. The investigated time scales are orders of magnitude too short to accommodate sub-nanosecond decay time of the excited charge carriers in semiconductors even when this can be further shortened by the LSP or by presence of the gold particles as additional recombination sites in the matrix.

Comparing the response of the samples with and without gold clusters, excited by 790 nm wavelength located within the range of the plasmon resonance band (Figure 6.5(a)), one notes two striking differences: at a given pump intensity, the reflectance change and the initial recovery time are enhanced for the material containing gold clusters. These effects increase when the density of the gold clusters increases. As opposed to the excitation by a

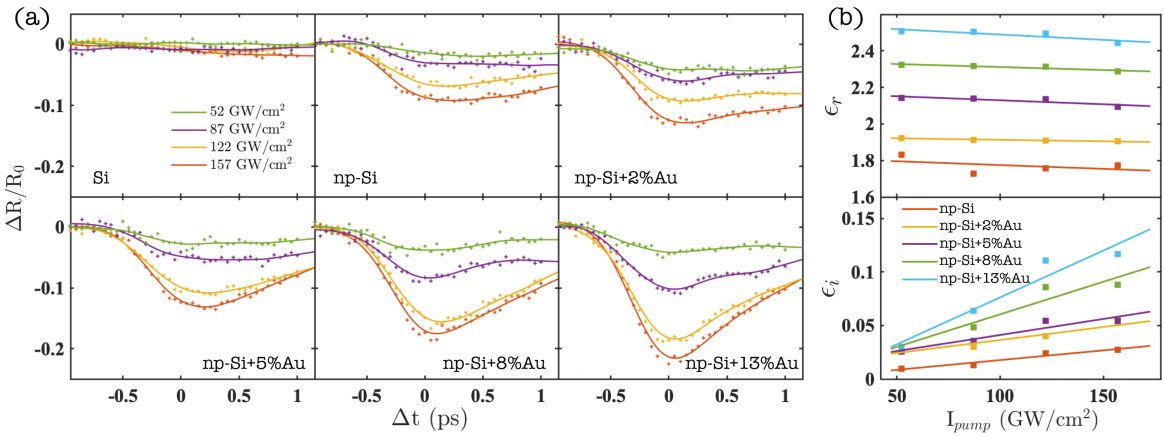


Figure 6.5: (a) time-resolved reflectance change, $\Delta R/R_0$, for the different intensities of the 790 nm pump and 2.5 μm fixed-intensity probe; (b) the dependence of the real and imaginary parts, $\epsilon_r$ and $\epsilon_i$, of the effective dielectric function on the pump intensity, $I$, for np-Si with different density of Au clusters.

wavelength of 1.1 μm, which is outside of the LSP resonance band, and using the same probe, where the dynamics of the optical response is identical for the samples with and without embedded gold nanoparticles, as shown in Figure 6.6.

For a meaningful discussion of these results, the effective real, $\epsilon_r$, and imaginary, $\epsilon_i$, parts of the dielectric function were deducted at the maxima of the absolute reflectance change and plotted in Figure 6.5(b) as a function of the pump fluence. The obtained dependence can be explained within the framework of the Drude model for the specific conditions of the probe frequency being greater than the electron-hole plasma frequency and the free carrier scattering rate, $\omega > \omega_p, 1/\tau$. At these conditions, the model approximates the real and imaginary parts of the dielectric function dependencies as $\epsilon_r - \frac{\omega_p^2}{\omega^2}$ and $\epsilon_i + \frac{\omega_p^2}{\omega^3 \tau}$, respectively[123]. The plasma frequency is given by $\omega_p^2 = \frac{e^2}{\epsilon_0} \frac{N}{m_{eff}}$, where the carrier density, $N$, is determined by the pump intensity, $I_{pump}$, and absorption coefficient of composite, $\alpha_{pump}$, as $N \propto \alpha_{pump} I_{pump}$; $m_{eff}$ is the effective mass of the electron-hole plasma in silicon.

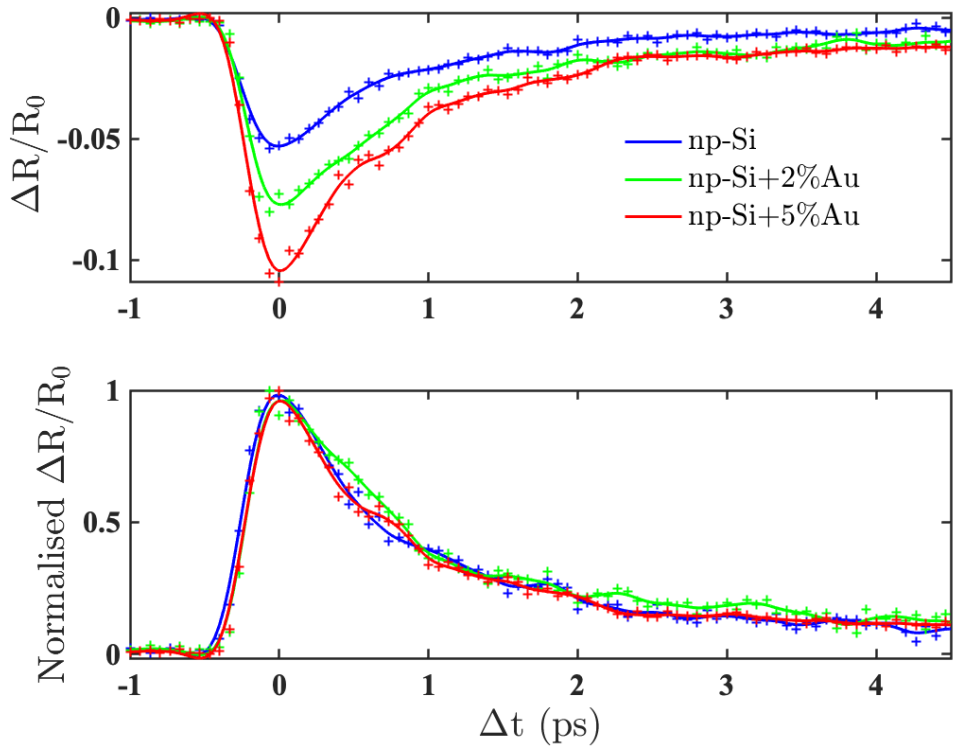


Figure 6.6: Time-resolved reflectance change for the pump wavelength of 1.1 μm and 2.5 μm probe. Top panel shows $\Delta R/R_0$, while the bottom panel shows the same results, but normalised to represent on the unitary scale for easier comparison. The pump intensity was kept at 160 GW/cm$^2$.

It is noted that despite the presence of gold clusters, the contribution of their dielectric function and its change due to the excitation by the pump does not significantly affect the optical response of the composite and does not have to be considered here. Indeed, the probe optical response is governed exclusively by the np-Si environment. This is because for the condition of $|\epsilon_c| \gg \epsilon_e$, the Maxwell-Garnett mixing can be approximated to represent the effective dielectric as $\epsilon_{eff} = \epsilon_r + i\epsilon_i \approx \epsilon_e(1 + 2f)$, where $f$ is a volume fraction of the gold clusters. Moreover, the excitation of the gold clusters by the pump does not considerably change their dielectric function, even at the conditions of the LSP resonance. At sub-picoseconds timescales the change of the dielectric function is governed by the electron density, $N_{noneq}$, driven out of the equilibrium by the pump. This density can be estimated by $N_{noneq} = \tau_{LSP}\alpha_{Au}\frac{I_{pump}}{\hbar\omega_{pump}}$. Using the LSP dephasing time, $\tau_{LSP}$ of 5 fs [264], a gold cluster absorption coefficient of $\alpha_{Au} = 1.5 \times 10^6$ cm$^{-1}$ [265, 266], it can be found that a fraction of 0.03 of the total charge density participate in the LSP excitation at the pump frequency. This fraction is too minor to alter the dielectric function of the gold clusters.

Therefore a simplified expression for $\epsilon_{eff}$, which does not need to involve $\epsilon_c$, can be used to investigate the dependence of $\epsilon_r$ and $\epsilon_i$ on the pump intensity, $I_{pump}$, for a given $f$. It can be seen on Figure 6.5(b) that the slopes of the curves family, $\epsilon_i(I_{pump}; f)$, given by $\frac{e^2}{\epsilon_0}\frac{N}{m_{eff}}\frac{1}{\omega^3\tau}$, tend to increase as the volume fraction of gold clusters, $f$, grows. It is rather tempting to attribute this to the enhancement of the carrier excitation by the pump and increase of $N$ in the samples with greater amount of the clusters. However, there are two arguments against this notion. First, it is not corroborated by the slopes of the $\epsilon_r(I_{pump}; f)$ set given by $-\frac{e^2}{\epsilon_0}\frac{N}{m_{eff}}\frac{1}{\omega^2}$, which have insignificant dependence on the parameter $f$. Second, the time resolved curves shown in Figure 6.5(a) demonstrate the identical tendency to recover to nearly the same value of $\Delta R/R_0$ after 1 picosecond from the extremum, irregardless of the embedded clusters density. This point is confirmed by

another independent set of measurements shown in Figure 6.8(a). Hence, on the average across the sample, the presence of the LSP field around the clusters neither enhances the excitation efficacy of the free carriers average density nor promotes charge transfer from gold to the surrounding silicon to affect the decay rate of the electron-hole pair in np-Si environment.

Thus, the change of the linear optical properties of np-Si in the presence of the gold cluster's LSP excitation is mainly governed by the alteration of the imaginary part of the composite effective dielectric function, $\epsilon_i$, where, as our analysis suggests, the dominant effect is nested in the change of the electron-hole plasma relaxation rate, $1/\tau$. It seems that this rate tends to increase as the gold fraction, $f$, increases and, hence, the contribution of the LSP to this effect, for a given pump power, $I_{pump}$.

This effect was verified by presenting the relaxation rate, $1/\tau$, as a function of the cluster's fraction, $f$, as shown in Figure 6.7(a). It suggests a linear dependence for which the LSP more than threefold enhances the charge carriers' scattering rate for the cluster's fraction of $f = 0.13$. The investigation of the reasons behind the enhancement is beyond the scope of this work, however it is noted that the LSP oscillating field might have broadened the free carriers energy distribution and increased their carrier-carrier collision rate.

There is another revealing point which can be demonstrated from $\Delta R/R_0$ time resolved curves. Deconvoluting the response of the pure np-Si from the curves measured on the composites separates the temporal contribution of the LSP and unveils a symmetric bell-shaped curve, similar to the shape of a slightly broadened pump pulse, as shown in Figure 6.7(b). Hence, the fast recovery of $\Delta R/R_0$ following the extremum is rather governed by the LSP relaxation, while the long tail extending into hundreds of picoseconds is attributed to the decay of the electron-hole plasma in np-Si matrix. It is very likely

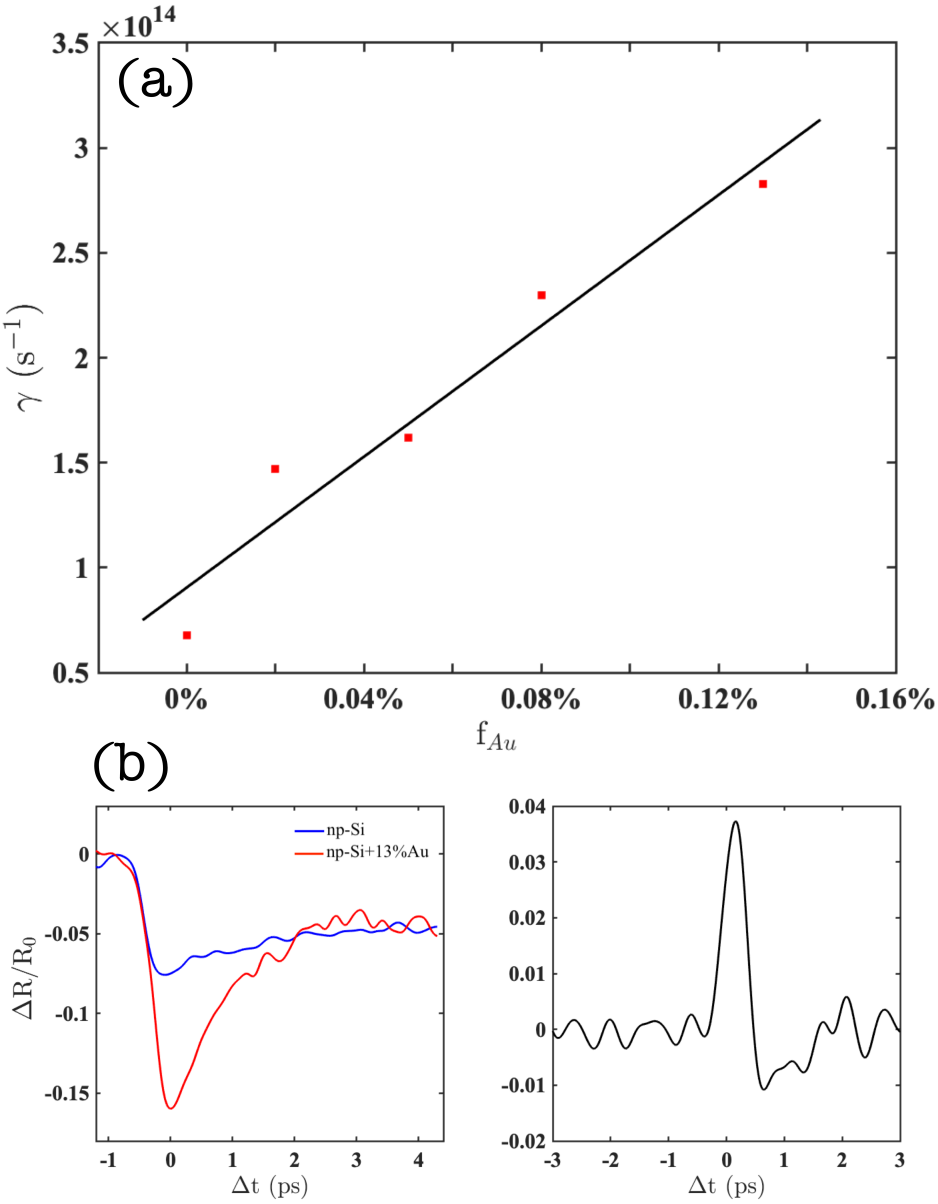


Figure 6.7: (a) Scattering rate $\gamma$, as a function of Au volume fraction $f_{Au}$, at the zero delay between the pump and probe. The pump intensity was kept at 157 GW/cm$^2$. (b) Left panel: the change of reflectance $\Delta R/R_0$ as a function of delay time $\Delta$t for np-Si (blue) and np-Si+13%Au (red); Right panel: the deconvoluted signal using the two curves shown in the left panel.

the LSP is as short lived as a few femtoseconds and it nearly adiabatically follows the excitation pulse.

**Nonlinear response in SWIR**

Furthermore, the dependence of $\tau$ on the external perturbation strongly suggests that the optical response can be significantly non-linear, as, for example, it was shown in the epsilon-near-zero materials[267, 268]. The non-linear response of the composites to the SWIR probe was investigated in the presence of the LSP excitation by the pump. For this series of experiments, the pump intensity was kept at the constant level of 160 GW/cm$^2$, but the probe was tuned in the range between 3.5 and 27 GW/cm$^2$, see Figure 6.8(a). Here, it can be seen that increasing the probe intensity has the opposite effect to that of the pump shown in Figure 6.5(a). That is, the absolute reflectance change, $|\Delta R/R_0|$, instead decreases as a function of the intensity. However, at longer time delays, past the localised surface plasmon decay time, there is no difference in the response between the samples with and without the clusters. Indeed, regardless of the composition, after 2 picoseconds all time resolved curves appear as a nearly identical long tail. On the contrary, the fast component has a substantial dependence of the $|\Delta R/R_0|$ on the gold fraction, $f$, for a given probe intensity around the zero delay time.

This observation confirms the proposal that the distinctive change to the optical response can be observed only during short time period of the LSP excitation. The measurements clearly demonstrate that the probe intensity-dependent response is at a maximum at the time corresponding to the temporal overlap between the pump and probe pulses. It is also very clear that the strongest change occurs in the samples with the highest density of the clusters where more free charges in the matrix are exposed to the LSP field.

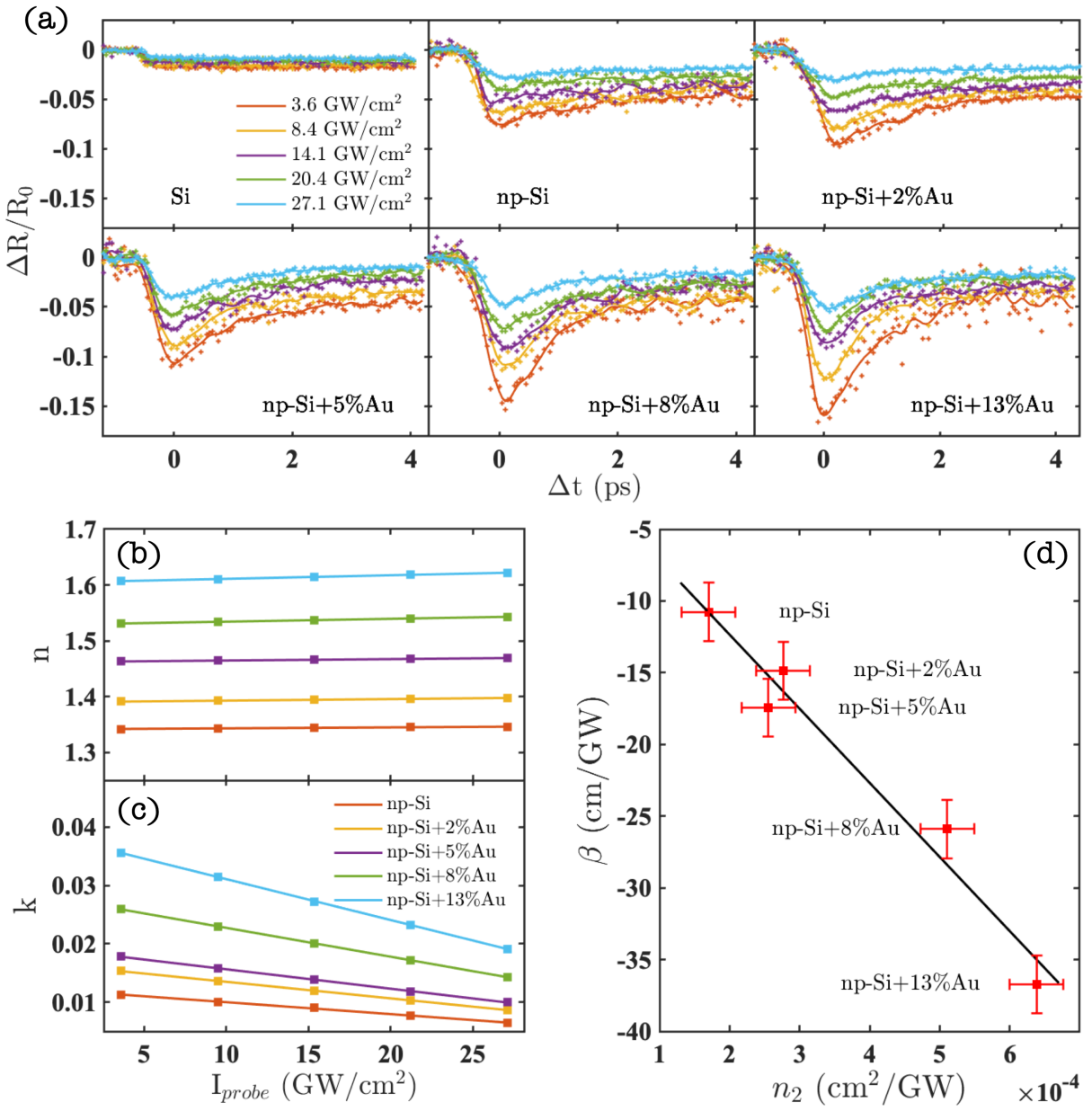


Figure 6.8: (a) time-resolved reflectance change, $\Delta R/R_0$, for the fixed pump intensity of 160 GW/cm$^2$ and different intensities of the probe; (b) the real and (c) the imaginary parts, $n$ and $k$, of the effective refractive index as a function of the 2.5 μm probe intensity; (d) non-linear Kerr and extinction indices, $n_2$ and $\beta$, for np-Si with different densities of Au clusters.

The effective refractive index was evaluated at the maxima of the time-resolved reflectance change and present its real, $n$, and imaginary, $k$, parts as a function of the probe intensity, $I_{probe}$, in Figure 6.8(b)-(c). The slopes are determined by the non-linear indices of $n_2$ and $\beta$[63], the real and imaginary parts of the non-linear refraction, which are shown in Figure 6.8(d). The investigated samples show that $n_2$ is positive, corresponding to Kerr non-linear self-focusing, while a negative $\beta$ is usually associated with the absorption saturation or bleaching. It is noted that the observed non-linearity is exclusively attributed to the free carriers excited by the pump, as without pumping neither material demonstrates significant non-linearity at the investigated probe intensities.

There is no established way to predict the free carriers response in the presence of LSP fields. As well, it is a very complex task to discern the underpinning mechanism of the free carriers' non-linear response in semiconductors, as it may originate from intertwined factors determining the values of the reduced mass, screening and relaxation. The exercise is further hindered when the process occurs in a non-equilibrium state with poorly defined distribution of the carriers. It is known from decades of bulk silicon research that free carrier absorption in a p-type degenerated material consists of two competing components of the more familiar intraband and featured intervalence split-off band free carrier transitions[269]. The former transition is known to saturate at a relatively high pumping level of two-to-three orders of magnitude above this work[270] and it might not be suitable to explain the observation. On the other hand, the intervalence transition is more sensitive as it depends on the product of occupation probabilities in two non-degenerate bands involved in the transition and it is known to saturate rapidly at above $5\times10^{18}$ cm$^{-3}$. np-Si with weak carrier confinement preserves many of the bulk silicon electro-optical properties and the absorption saturation can be recognised from the decrease of the reflectance change as a function of the increasing probe intensity in Figure 6.8(a). This effect is further enhanced when gold clusters are embedded into the np-Si matrix, but it

is only temporarily efficient during the time window of the localised plasmon excitation. It is very likely that the effect of the absorption saturation enhancement is the result of disturbing the free carriers distribution and population probability in a way that fewer states are available for the intervalence split-off band transitions of the free charge carriers.

The nonlinear coefficient of Au/np-Si composites has the same orders of magnitude as typical nonlinear materials such as Carbon Disulfide[271] and is almost an order of magnitude higher than bulk silicon and germanium[272, 273]. Overall the efficiency on the non-linear enhancement of the composites should be judged against the response of the bare porous silicon at the identical conditions. Incorporation of just 0.13 of gold volume fraction not only more than five-fold enhances the non-linear optical response in the presence of the LSP excitation, but also shorten the recovery time by an order of magnitude, allowing implementation of the effect in applications where the high-speed response is essential.

In conclusion, novel plasmonic-semiconducting composites were produced through embedding Au nanoparticles in the pore channels of 500 nm thick np-Si with immersion plating technique. By controlling the immersion time and plating solution concentration, composites with different AuNP sizes and densities were fabricated. SEM, TEM, EDX and darkfield microscopy were employed for the characterisation of the samples. The composites exhibit localised surface plasmon resonance around 800 nm due to the presence of Au clusters. Compared to AuNPs in a gas or liquid environment, the LSPR peak is redshifted due to the increased environment refractive index. Scattering spectroscopy measurements show that the LSPR wavelength is directly related to the size of AuNPs, and the resonance wavelength of the composite material can be controlled by adjusting the immersion plating conditions. In order to demonstrate the potential application of the composite material, the sample with the highest Au concentration was used as the SERS substrate. The obtained Raman spectrum of Methylene Blue suggests that the composite

substrate enhances the Raman signal by $10^9$ orders of magnitude. Therefore, it is suitable to be used as the substrate material for ultra-sensitive Raman detection. In addition, the ultrafast NIR pump-SWIR probe technique was employed to investigate the linear and nonlinear optical properties of the composites. The pump wavelength was set to 790 nm for the LSPR excitation, and the transient change of reflectance was measured by the 2.5 μm probe under different pump and probe intensities. The results show that both the linear and nonlinear responses of np-Si were enhanced by incorporating AuNPs in its pore channels, while the enhancement is a short-lived effect that follows the pump profiles and decays within a few picoseconds.

# Chapter Seven

# Conclusion

This thesis introduces the work on the opto-electronic properties and ultrafast carrier dynamics of nano- and macro-porous silicon. The femtosecond pump-probe technique was employed to measure the excited state properties of the samples. An optical model which combined TMM, Drude model and MGMR was used to retrieve the material properties from the experimental results. Other equipment such as Spectrometer, Dark Field Microscope, FTIR and Ellipsometor were also utilised to characterise the sample response in the different spectral regions. Chapter 1 introduces the state of the art of ultrafast dynamics in silicon-based materials and the importance of this work. The theoretical background detailed description of optical models used in this work was presented in Chapter 2. The equipment employed to obtain the experimental results are illustrated in Chapter 3. While Chapters 4, 5 and 6 show the experimental results and discussions.

In Chapter 4, NIR pump-MWIR probe experiments were conducted to investigate the excited carrier response of np-Si. In contrast to the crystalline silicon, the recombination rate of np-Si is about three orders of magnitude faster, which can benefit applications such as all-optical switching and modulation. The dominant process was found to be the Auger recombination. The fast recombination of np-Si is similar to silicon nanocrystals, though

the dimensionality of the two types of sample is different[274, 275]. It overcomes the SHR recombination, although the np-Si is heavily doped. This study also demonstrated that the diffusion process is suppressed by fast recombination. The possible reason for it is the high scattering rate of the free carriers induced by the phonon and carrier-carrier collisions. Another main finding of this study is the observation of an Auger recombination pathway enabled by the vibrational modes of surface adsorbates attached to the pores of np-Si. This is a new recombination mechanism that has not been known previously.

Chapter 5 focuses on the potential application of mp-Si as an all-optical modulator material operated in the MWIR. The reflection spectrum was measured as a function of the time difference between pump and probe pulses. By varying the pump intensity, the change of reflectance which corresponds to the modulation contrast was evaluated. The phase transition from semiconductor to metal was observed with a high pump intensity. An optimum condition of the fastest response and greatest modulation contrast were estimated from an optical model and confirmed experimentally. The results show a 30% change of the reflected signal within 0.55 ps. Compared to the bulk silicon, mp-Si has a lower effective refractive index which makes it easier to reach the optimum modulation condition where $\epsilon_{eff} \rightarrow 1$. In addition, the all-optical modulator consists of mp-Si was used to construct a high-resolution Time-of-Flight set-up. The results show that the key parameter that determines the ToF resolution is the pump pulse duration which defines the rising time of the modulator's optical response. It was demonstrated that the temporal resolution of the ToF set-up is about 100 femtoseconds which fulfil most of the application requirements. With such high resolution, the pulse broadening effect caused by the group velocity delay of the silica rod was observed. The group velocity delay coefficient was determined by deconvoluting the modulator response with and without the silica rod in the optical path.

A novel composite material consisting of np-Si and Au nanoparticles were fabri-

cated and characterised in Chapter 6. An immersion plating technique was employed to impregnate Au clusters deep into the pore channel of np-Si with a thickness of 550 nm. The distribution of Au nanoparticles and uniformity of the composites are examined by SEM, TEM and EDX and dark field microscopy. The localised surface plasmon resonance peak of the Au clusters in the np-Si environment was characterised by measuring the scattering spectrum with a VIS-NIR spectrometer. In addition, to investigate the potential application of the composites, it was used as a SERS substrate for the measurement of the Methylene Blue Raman spectrum. The results show that the detection limit was in the picomolar range, which corresponds to an enhancement factor of $10^9$. The high amplification provided by this SERS substrate can be assigned to the high density of the Au nanoparticles in the composites. In addition, the linear and non-linear optical properties of the composites were studied with NIR pump-SWIR probe (2.5 μm). The pump excitation wavelength was set to 790 nm to excite the LSPR. The measurements show that the scattering rate of the composites is higher than in the bare np-Si. Besides, an enhancement of optical nonlinearity is also observed in the composite material, making it suitable for applications such as optical switches and laser cavities.

**Outlook:** The experimental results obtained in this work demonstrated that np-Si, mp-Si and AuNP/np-Si composites exhibit controllable carrier dynamics and optical responses owing to their tunable structures. Therefore, it is worthwhile to explore their material properties and potential applications thoroughly. However, there are still some technical difficulties that hinder further research on these structured semiconductors and composite materials. Hence, some suggestions are made for the future work of this project. First, it is necessary to develop a fabrication procedure that can precisely control the porosity and thickness of the porous silicon. These parameters are highly sensitive to the concentration and temperature of the anodisation solvent which varies with time. As a result, it is difficult to obtain two identical samples through different anodising runs. So far,

the porosity and thickness are controlled by varying the current and time of anodisation. As the solvent concentration decreases over time, these parameters need to be adjusted accordingly, which is not ideal for large-scale production. A potential solution may be to add a temperature and concentration feedback loop to the anodisation system that can help keep these parameters constant in real-time. Second, there is a lack of theory and quantitative experiments to determine the reduction rate of Au as a function of plating solution concentration and temperature during the AuNP impregnation process. The fabrication process of composites demonstrated in Chapter 6 is optimised through series of experimental trials. Therefore, the conditions found are empirical without theoretical support. A deeper understanding of the reduction mechanism is essential and will further simplify the optimisation process of the fabrication condition. Last, only gold-based composite materials were investigated in this work. In the future, it will be beneficial to incorporate different metal clusters (platinum, silver, nickel, iron) into np-Si, which may extend the potential applications of the composite materials to wider fields such as catalysis, biotechnology, and magneto-optic devices[276, 277, 278].

# Appendix One

# Transfer Matrix Method and Scattering Matrix Method

## A.1 Basic Transfer Matrix

This section introduce the most basic transfer matrix method and its detailed derivation. According to Maxwell equation(appendix 1), the relation between electric and magnetic field can be expressed as: $\nabla \times \vec{E} = -\frac{\partial \vec{B}}{\partial t}$ (Faraday's law), and $\nabla \times \vec{B} = \frac{1}{c^2}\frac{\partial \vec{E}}{\partial t}$ (Ampere's law, no curremt), for homogeneous, isotropic materials. $\vec{E}$ is the electric field vector, $\vec{B}$ is the magnetic field vector, $c$ is the speed of light in the material which is defined as $c = \frac{1}{\sqrt{\epsilon_0 \epsilon_r \mu_0 \mu_r}}$, where $\epsilon_0 = 8.85^{-12} F/m$ and $\mu_0 = 1.26^{-6} H/m$ is the permittivity and permeability of free space, respectively. $\epsilon_r$ and $\mu_r$ is the permittivity and permeability of material. Note here that all the equations are in SI units and we use negative convention in this section, which means the material dielectric function $\epsilon_r = \epsilon' - i\epsilon''$.

For the sake of convenience, the magnetic field strength $\vec{H}$ is used in transfer matrix instead of $\vec{B}$. The relation between them is $\vec{H} = \frac{1}{\mu_0 \mu_r}\vec{B} - \vec{M}$, $\vec{M}$ is the magnetisation

vector. For material without magnetisation, $\vec{M} = 0$. Therefore,

$$\nabla \times \vec{E} = -\mu_0 \mu_r \frac{\partial \vec{H}}{\partial t} = -i\mu_0 \mu_r \omega \vec{H} = -ik_0 Z_r \vec{H} \tag{A.1}$$

with the impedance of material $Z_r = \sqrt{\frac{\mu_0 \mu_r}{\epsilon_0 \epsilon_r}}$. We can also write the change of magnetic field in the same way as

$$\nabla \times \vec{H} = ik_0 \frac{1}{Z_r} \vec{E} \tag{A.2}$$

We define the $z$ direction as normal to the material surface and assume EM field has $s$ polarisation. According to the boundary condition, the electric field component in $y$ direction (out of plane) and magnetic field component in $x$ direction (in-plane) do not change. Hence, we can obtain the field in supperstrate and substrate if we know how the field propagate inside the material.

At any location, the total electric field $\vec{E_y}$ is the summation of forward and backward travelling field:

$$\vec{E_y} = \vec{E}_{y(right)} e^{-i\vec{k}\cdot\vec{r}} + \vec{E}_{y(left)} e^{i\vec{k}\cdot\vec{r}} \tag{A.3}$$

where $\vec{r}$ is the direction of propagation. $\vec{k}$ is the wavevector in the media $\vec{k} = \vec{k_0} n$ and $n = \sqrt{\epsilon_r}$ is the refractive index of the material. In isotropic materials, $\vec{r}$ and $\vec{k}$ are in the same direction.

We can represent magnetic field with electric field as:

$$\vec{H}_x = \frac{1}{ik_0 Z_r} \frac{\partial \vec{E_y}}{\partial z} = -\frac{cos(\theta)}{Z_r} \vec{E_y} \tag{A.4}$$

here, $\theta$ is the angle between direction of wavevector and normal of the surface. We use notation $Y_r = -\frac{cos(\theta_r)}{Z_r}$ to simplify the equation.

Therefore, the total magnetic field is:

$$\begin{aligned} \vec{H_x} &= \vec{H}_{x(right)} e^{-i\vec{k}\cdot\vec{r}} + \vec{H}_{x(left)} e^{i\vec{k}\cdot\vec{r}} \\ &= Y_r \vec{E}_{y(right)} e^{-i\vec{k}\cdot\vec{r}} - Y_r \vec{E}_{y(left)} e^{i\vec{k}\cdot\vec{r}} \end{aligned} \tag{A.5}$$

Please note here that the electric field direction remains the same while the magnetic field reverse change direction when travelling back (for both s and p polarisation). Therefore, at location $p_1$:

$$\vec{E_y}(p_1) = \vec{E}_{y(right)} e^{-i\vec{k}\cdot\vec{r_1}} + \vec{E}_{y(left)} e^{i\vec{k}\cdot\vec{r_1}} \tag{A.6}$$

$$\vec{H_x}(p_1) = Y_r \vec{E}_{y(right)} e^{-i\vec{k}\cdot\vec{r_1}} - Y_r \vec{E}_{y(left)} e^{i\vec{k}\cdot\vec{r_1}} \tag{A.7}$$

$\theta_r$ is the angle between surface normal and light inside the material. We write them in matrix form:

$$\begin{bmatrix} \vec{E_y}(p_1) \\ \vec{H_x}(p_1) \end{bmatrix} = M_1 \begin{bmatrix} \vec{E}_{y(right)} \\ \vec{E}y_{(left)} \end{bmatrix} \tag{A.8}$$

where

$$M_1 = \begin{bmatrix} e^{-i\vec{k}\cdot\vec{r_1}} & e^{i\vec{k}\cdot\vec{r_1}} \\ Y_r e^{-i\vec{k}\cdot\vec{r_1}} & -Y_r e^{i\vec{k}\cdot\vec{r_1}} \end{bmatrix} \tag{A.9}$$

at location $p_2$ the matrix $M_2$ is

$$M_2 = \begin{bmatrix} e^{-i\vec{k}\cdot\vec{r_2}} & e^{i\vec{k}\cdot\vec{r_2}} \\ Y_r e^{-i\vec{k}\cdot\vec{r_2}} & -Y_r e^{i\vec{k}\cdot\vec{r_2}} \end{bmatrix} \tag{A.10}$$

Therefore,

$$\begin{bmatrix} \vec{E_y}(p_1) \\ \vec{H_x}(p_1) \end{bmatrix} = M_1 M_2^{-1} \begin{bmatrix} \vec{E_y}(p_2) \\ \vec{H_x}(p_2) \end{bmatrix} \tag{A.11}$$

$$\begin{aligned} M_1 M_2^{-1} &= \frac{1}{M_2(1,1)M_2(2,2) - M_2(1,2)M_2(2,1)} \times \\ &\quad \begin{bmatrix} M_1(1,1)M_2(2,2) - M_1(1,2)M_2(2,1) & -M_1(1,1)M_2(1,2) + M_1(1,2)M_2(1,1) \\ M_1(2,1)M_2(2,2) - M_1(2,2)M_2(2,1) & -M_1(2,1)M_2(1,2) + M_1(2,2)M_2(1,1) \end{bmatrix} \\ &= -\frac{1}{2Y_r} \begin{bmatrix} -Y_r(e^{i\vec{k}\cdot\vec{a}} + e^{-i\vec{k}\cdot\vec{a}}) & -e^{i\vec{k}\cdot\vec{a}} + e^{-i\vec{k}\cdot\vec{a}} \\ -Y_r^2(e^{i\vec{k}\cdot\vec{a}} - e^{-i\vec{k}\cdot\vec{a}}) & -Y_r(e^{i\vec{k}\cdot\vec{a}} + e^{-i\vec{k}\cdot\vec{a}}) \end{bmatrix} \end{aligned} \tag{A.12}$$

After simplification, we have the final relation between the field on the left and right hand side:

$$\begin{bmatrix} \vec{E_y}(p_2) \\ \vec{H_x}(p_2) \end{bmatrix} = \begin{bmatrix} cos(\vec{k}\cdot\vec{a}) & i\frac{1}{Y_r}sin(\vec{k}\cdot\vec{a}) \\ iY_r sin(\vec{k}\cdot\vec{a}) & cos(\vec{k}\cdot\vec{a}) \end{bmatrix} \begin{bmatrix} \vec{E_y}(p_1) \\ \vec{H_x}(p_1) \end{bmatrix} \tag{A.13}$$

where $\vec{a} = \vec{r_2} - \vec{r_1}$. If the matrix connect the field on the left and right side of the material, $|a| = dcos(\theta_r)$ and $d$ is the thickness of the layer.

The transfer matrix of a layer represents the linear transformation between incoming and outgoing light passing through the material. When there are multiple layers in an optical system, the transfer matrix of the entire system can be written as the product of the transfer matrix of each layer $M = M_1 \times M_2 \times .....M_n$, where $n$ is the number of layers. The sequence of multiplication is important in matrix operation. It has to follows the light propagation direction.

It is often useful to calculate the reflectance and transmittance of light passing through single or multiple layered optical system. This can be done through the transfer matrix method. The electric field $\vec{E_y}$ on the left of the system is the summation of the incident and reflected field $\vec{E_y} = \vec{E_0} + r\vec{E_0}$, where $r$ is the reflection coefficient. On the right hand side, we have $\vec{E_y} = t\vec{E_0}$. $t$ is the transmission coefficient. $k_s$ and $r_s$ are the wavevector and position in the substrate, respectively. For the magnetic field, we can write: $\vec{H_x} = Y_0\vec{E_0} - rY_0\vec{E_0}$ and $\vec{H_x} = tY_s\vec{E_0}$. Where $Y_{in} = -\frac{cos(\theta_{in})}{Z_{in}}$ and $Y_s = -\frac{cos(\theta_s)}{Z_s}$. $\theta_{in}$, $\theta_s$, $Z_{in}$ and $Z_s$ are incident angle, angle in substrate, impedance of superstrate and substrate, respectively. We write them in matrix form:

$$\begin{bmatrix} \vec{E_0} + r\vec{E_0} \\ Y_{in}\vec{E_0} - rY_{in}\vec{E_0} \end{bmatrix} = M \begin{bmatrix} t\vec{E_0} \\ tY_s\vec{E_0} \end{bmatrix} \tag{A.14}$$

The reflection and transmission coefficient can be extracted from the matrix:

$$r = \frac{Y_{in}M(1,1) + Y_{in}Y_sM(1,2) - M(2,1) - Y_sM(2,2)}{Y_{in}M(1,1) + Y_{in}Y_sM(1,2) + M(2,1) + Y_sM(2,2)} \tag{A.15}$$

$$t = \frac{2Y_{in}}{Y_{in}M(1,1) + Y_{in}Y_sM(1,2) + M(2,1) + Y_sM(2,2)} \tag{A.16}$$

Therefore, we can obtain the reflectance $R = |r|^2$ and transmittance $T = \frac{Y_s}{Y_{in}}|t|^2$ of the multi-layer material.

## A.2 Generalised Transfer Matrix

### A.2.1 Derive the matrix

The basic Transfer Matrix only can be used for linear polarised light which do not have many practical use – Most of the experiments need unpolarised or circular polarised light, such as ellipsometry and spectrometer. In this section, a generalised Transfer Matrix is introduced which is suitable for all polarisation states. Same as the basic transfer matrix method, we start with the Maxwell Equation $\nabla \times \vec{E} = -\frac{\partial \vec{B}}{\partial t}$, $\nabla \times \vec{B} = \frac{1}{c^2}\frac{\partial \vec{E}}{\partial t}$ and $\vec{B} = \frac{1}{\mu_0\mu_r}\vec{H}$, assume there is no magnetisation and current. Note that in this section, we use positive sign convention $\epsilon_r = \epsilon' + i\epsilon''$. By expending the curl operator, we can further write the equation set as:

$$\begin{aligned}
\frac{\partial E_z}{\partial y} - \frac{\partial E_y}{\partial z} &= k_0\mu_r\tilde{H}_x & \frac{\partial \tilde{H}_z}{\partial y} - \frac{\partial \tilde{H}_y}{\partial z} &= k_0\epsilon_r E_x \\
\frac{\partial E_x}{\partial z} - \frac{\partial E_z}{\partial x} &= k_0\mu_r\tilde{H}_y & \frac{\partial \tilde{H}_x}{\partial z} - \frac{\partial \tilde{H}_z}{\partial x} &= k_0\epsilon_r E_y \\
\frac{\partial E_y}{\partial x} - \frac{\partial E_x}{\partial y} &= k_0\mu_r\tilde{H}_z & \frac{\partial \tilde{H}_y}{\partial x} - \frac{\partial \tilde{H}_x}{\partial y} &= k_0\epsilon_r E_z
\end{aligned} \tag{A.17}$$

This equation set represent the relation between electric and magnetic field in medium with permittivity of $\epsilon_r$ and permeability of $\mu_r$, where $\tilde{H}_x = i\eta_0\vec{H}$, $\eta_0 = \sqrt{\frac{\mu_0}{\epsilon_0}}$. For the

wave vector, we have the following relation:

$$\begin{aligned} k_x &= k_0\sqrt{\epsilon_r\mu_r}sin(\theta)cos(\phi) \\ k_y &= k_0\sqrt{\epsilon_r\mu_r}sin(\theta)sin(\phi) \\ k_z &= \sqrt{k_0^2\epsilon_r\mu_r - k_x^2 - k_y^2} \end{aligned} \tag{A.18}$$

When the wave propagation in homogeneous medium, the electric field and magnetic field have the following mathematical form:

$$\begin{aligned} \vec{E}(\vec{r}) &= \vec{E_0}e^{ik\vec{r}} = \vec{E_0}e^{ik_x x}e^{ik_y y}e^{ik_z z} \\ \vec{\tilde{H}}(\vec{r}) &= \vec{\tilde{H}_0}e^{ik\vec{r}} = \vec{\tilde{H}_0}e^{ik_x x}e^{ik_y y}e^{ik_z z} \end{aligned} \tag{A.19}$$

We show an example of derivation on a certain direction:

$$\frac{\partial\vec{E}}{\partial x}(\vec{r}) = \frac{\partial(\vec{E_0}e^{ik_x x}e^{ik_y y}e^{ik_z z})}{\partial x} = ik_x\vec{E}(\vec{r}) \tag{A.20}$$

Therefore, we have $\dfrac{\partial}{\partial x} = ik_x$ and $\dfrac{\partial}{\partial y} = ik_y$. However we do not have the same on z direction because the material might have multilayer.

Therefore, the equation B.15 became:

$$\begin{aligned} ik_yE_z - \frac{\partial E_y}{\partial z} &= k_0\mu_r\tilde{H}_x & ik_y\tilde{H}_z - \frac{\partial\tilde{H}_y}{\partial z} &= k_0\epsilon_r E_x \\ \frac{\partial E_x}{\partial z} - ik_xE_z &= k_0\mu_r\tilde{H}_y & \frac{\partial\tilde{H}_x}{\partial z} - ik_x\tilde{H}_z &= k_0\epsilon_r E_y \\ ik_xE_y - ik_yE_X &= k_0\mu_r\tilde{H}_z & ik_x\tilde{H}_y - ik_y\tilde{H}_x &= k_0\epsilon_r E_z \end{aligned} \tag{A.21}$$

We can further simplify the above equation set by using the normalised term $\tilde{k_{x,y}} = \dfrac{k_{x,y}}{k_0}$ and $z' = zk_0$:

$$\begin{aligned} i\tilde{k_y}E_z - \frac{\partial E_y}{\partial z'} &= \mu_r\tilde{H}_x & i\tilde{k_y}\tilde{H}_z - \frac{\partial\tilde{H}_y}{\partial z'} &= \epsilon_r E_x \\ \frac{\partial E_x}{\partial z'} - i\tilde{k_x}E_z &= \mu_r\tilde{H}_y & \frac{\partial\tilde{H}_x}{\partial z'} - i\tilde{k_x}\tilde{H}_z &= \epsilon_r E_y \\ i\tilde{k_x}E_y - i\tilde{k_y}E_x &= \mu_r\tilde{H}_z & i\tilde{k_x}\tilde{H}_y - i\tilde{k_y}\tilde{H}_x &= \epsilon_r E_z \end{aligned} \tag{A.22}$$

From the last two equation in equation set, we can obtain $\tilde{H_z} = \frac{i}{\mu_r}(i\tilde{k_x}E_y - i\tilde{k_y}E_x)$ and $\tilde{E_z} = \frac{i}{\epsilon_r}(i\tilde{k_x}\tilde{H_y} - i\tilde{k_y}\tilde{H_x})$. We insert them back into the equation set and obtain:

$$\begin{aligned}
\tilde{k_y}^2\tilde{H_x} - \tilde{k_x}\tilde{k_y}\tilde{H_y} - \epsilon_r\frac{\partial E_y}{\partial z'} &= \mu_r\epsilon_r\tilde{H_x} \\
\epsilon_r\frac{\partial E_x}{\partial z'} + \tilde{k_x}^2\tilde{H_y} - \tilde{k_x}\tilde{k_y}\tilde{H_x} &= \mu_r\epsilon_r\tilde{H_y} \\
\tilde{k_y}^2 E_x - \tilde{k_x}\tilde{k_y}E_y - \mu_r\frac{\partial \tilde{H_y}}{\partial z'} &= \mu_r\epsilon_r E_x \\
\mu_r\frac{\partial \tilde{H_x}}{\partial z'} + \tilde{k_x}^2 E_y - \tilde{k_x}\tilde{k_y}E_x &= \mu_r\epsilon_r E_y
\end{aligned} \tag{A.23}$$

After rearranging, we have:

$$\begin{aligned}
\frac{\partial E_x}{\partial z'} &= \frac{\tilde{k_x}\tilde{k_y}}{\epsilon_r}\tilde{H_x} + (\mu_r - \frac{\tilde{k_x}^2}{\epsilon_r})\tilde{H_y} \\
\frac{\partial E_y}{\partial z'} &= (\frac{\tilde{k_y}^2}{\epsilon_r} - \mu_r)\tilde{H_x} - \frac{\tilde{k_x}\tilde{k_y}}{\epsilon_r}\tilde{H_y} \\
\frac{\partial \tilde{H_x}}{\partial z'} &= \frac{\tilde{k_x}\tilde{k_y}}{\mu_r}E_x + (\epsilon_r - \frac{\tilde{k_x}^2}{\mu_r})E_y \\
\frac{\partial \tilde{H_y}}{\partial z'} &= (\frac{\tilde{k_y}^2}{\mu_r} - \epsilon_r)E_x - \frac{\tilde{k_x}\tilde{k_y}}{\mu_r}E_y
\end{aligned} \tag{A.24}$$

Write in matrix form:

$$\frac{\partial}{\partial z'}\begin{bmatrix} E_x \\ E_y \\ \tilde{H_x} \\ \tilde{H_y} \end{bmatrix} = \begin{bmatrix} 0 & 0 & \frac{\tilde{k_x}\tilde{k_y}}{\epsilon_r} & \mu_r - \frac{\tilde{k_x}^2}{\epsilon_r} \\ 0 & 0 & \frac{\tilde{k_y}^2}{\epsilon_r} - \mu_r & -\frac{\tilde{k_x}\tilde{k_y}}{\epsilon_r} \\ \frac{\tilde{k_x}\tilde{k_y}}{\mu_r} & \epsilon_r - \frac{\tilde{k_x}^2}{\mu_r} & 0 & 0 \\ \frac{\tilde{k_y}^2}{\mu_r} - \epsilon_r & -\frac{\tilde{k_x}\tilde{k_y}}{\mu_r} & 0 & 0 \end{bmatrix}\begin{bmatrix} E_x \\ E_y \\ \tilde{H_x} \\ \tilde{H_y} \end{bmatrix} \tag{A.25}$$

If we use $\Phi(z') = \begin{bmatrix} E_x(z') \\ E_y(z') \\ \tilde{H}_x(z') \\ \tilde{H}_y(z') \end{bmatrix}$ and $\Omega$ represents the transfer matrix, we can write the complicated matrix in a single differential equation: $\dfrac{\partial \Phi}{\partial z'} - \Omega\Phi = 0$, which has the solution of $\Phi(z') = e^{\Omega z'}\Phi(0)$. To solve the exponential of matrix $e^{\Omega z'}$, we need to know the eigenvector matrix $W$ and eigenvalue matrix $\lambda$ of $\Omega$. The function of matrix is evaluated through $e^{\Omega z'} = We^{\lambda z'}W^{-1}$. Thus, we have $\Phi(z') = We^{\lambda z'}W^{-1}\Phi(0)$, we can combine $W^{-1}\Phi(0)$ and note it as $c$ so it becomes a column vector. In the end, we have the overall solution $\Phi(z')$ which sums all the modes at plane $z'$, the square matrix $W$ which describe the modes can exist in a material and relative amplitude between $E$ and $H$ field, diagonal matrix $e^{\lambda z'}$ describing how the modes propagate and $c$, column vector containing the amplitude coefficient of each mode. For a isotropic material with $\epsilon_r$ , $\mu_r$ and a wave at normal incidence,

$$\Omega = \begin{bmatrix} 0 & 0 & 0 & \mu_r \\ 0 & 0 & -\mu_r & 0 \\ 0 & \epsilon_r & 0 & 0 \\ -\epsilon_r & 0 & 0 & 0 \end{bmatrix} \tag{A.26}$$

To obtain the eigenvalue matrix $\lambda$, we need to solve the determinant of the eigenequation $|\Omega - \lambda I| = 0$, where $I$ is the identity matrix.

$$|\Omega - \lambda I| = \begin{bmatrix} -\lambda & 0 & 0 & \mu_r \\ 0 & -\lambda & -\mu_r & 0 \\ 0 & \epsilon_r & -\lambda & 0 \\ -\epsilon_r & 0 & 0 & -\lambda \end{bmatrix} \tag{A.27}$$

which results in a characteristic polynomial $(\lambda^2 + \epsilon_r\mu_r)^2 = 0$. The solution of the function

is $\lambda = \pm i\sqrt{\epsilon_r \mu_r}$. Now we put the eigenvalue into the digonal matrix:

$$\lambda = \begin{bmatrix} +i\sqrt{\epsilon_r\mu_r} & 0 & 0 & 0 \\ 0 & -i\sqrt{\epsilon_r\mu_r} & 0 & 0 \\ 0 & 0 & +i\sqrt{\epsilon_r\mu_r} & 0 \\ 0 & 0 & 0 & -i\sqrt{\epsilon_r\mu_r} \end{bmatrix} \tag{A.28}$$

Through the relation of $\Omega W = W\lambda$, we can further solve the enginvector matrix:

$$W = \begin{bmatrix} -\frac{i}{\sqrt{\epsilon_r\mu_r}} & \frac{i}{\sqrt{\epsilon_r\mu_r}} & 0 & 0 \\ 0 & 0 & \frac{i}{\sqrt{\epsilon_r\mu_r}} & -\frac{i}{\sqrt{\epsilon_r\mu_r}} \\ 0 & 0 & 1 & 1 \\ 1 & 1 & 0 & 0 \end{bmatrix} \tag{A.29}$$

Note that this is just one of the eigenvector matrix, there can be other solutions depends on the sequence of eigenvalues in matrix. The eigenmatrices have actual meanings – it describes how the mode propagates in the material. The four columns in $W$ and $\lambda$ are the four modes with direction of $(-H_x, E_y, k_z)$, $(H_x, E_y, -k_z)$, $(H_y, E_x, k_z)$ and $(-H_y, E_x, -k_z)$, respectively. From here we can see that, the electric field does not change direction when reflects back but the magnetic field does, as mentioned in the first section.

After we describe the field inside a single layer material, we can now extend this method to multilayer structure by considering the boundary conditions at the interfaces. Assume a three layer structure with field $\Phi_{i-1}, \Phi_i, \Phi_{i+1}$ (from left to right), we have $\Phi_{i-1}(z'_{end}) = \Phi_i(0)$, due to the continuity of $E_{x,y}$ and $H_{x,y}$ field at the interface. Therefore, $W_{i-1}e^{\lambda z'_{end}}c_{i-1} = W_i c_i$, the same relation applies betwee $(i)_{th}$ and $(i+1)_{th}$ layer. Thus, the relation between column vector $c$ (contains the amplitude coefficient of each mode) of different layers can be expressed as $c_i = W_i^{-1}W_{i-1}e^{\lambda_{i-1}z'_{end}}c_{i-1}$. Hence, the transfer matrix $T_{i-1}$ of $(i-1)_{th}$ layer is $W_i^{-1}W_{i-1}e^{\lambda_{i-1}l_{i-1}}$, $l$ is the thickness of the layer. To connect to the super- and substrate, we write the $c$ on substrate (transmission) side

$c_{sub} = T_{total}c_1$, where $c_1$ is the column vector of first layer. For the field in superstrate , we have $c_{super} = W_{super}^{-1}W_1c_1$, where $c_{super}$ contains the incident and reflected field. By eliminating $c_1$, we obtain $c_{sub} = T_{total}W_1^{-1}W_{super}c_{super}$, where $T_{total}$ is the transfer matrix of the entire media with n layers: $T_{total} = T_n \times T_{n-1} \times ... \times T_1$.

### A.2.2 The instability – mode sorting

Although the generalised transfer matrix is powerful, it has numerical instability. This is due to the fact that the matrix treats all the waves as if they are forward propagating with exponential decay $e^{-\lambda z'}$ or growth $e^{+\lambda z'}$ (it is actually backward wave). When the material has high loss, such as metal, the exponential growth part quickly become unstable. For example, the refractive index of silver at 633 nm is $0.056206 + i4.2776$ [ref], $k = \dfrac{2\pi}{633 \times 10^{-9}} \times (1.4721 + 1.4529i)$, we assume the layer thickness is 10 $\mu m$, for backward propagation wave $exp^{-ikz} = 1.9139 \times 10^{184} + 1.6257 \times 10^{184}i$. This is an abnormal number for phase change, and will results in an enormous field amplitude when connecting to external environment. The situation drastically gets worse when layer thickness increases. Therefore, one possible solution is to slice the thick layer into many thin layers within the numerical stable range. Or, solve it in a more clever way by distinguishing the forward and backward propagation wave in matrix.

As mentioned before, the four columns of eigenvector matrix represents the wave propagating in the direction of forward, backward, forward and backward, respectively. To distinguish the wave propagating in different directions, we need to rearrange the eigenvector and eigenvalue matrix, so that we can group the waves propagating in the same direction together. We swap the second with the third column in the eigenvector

matrix:

$$W = \begin{bmatrix} -\frac{i}{\sqrt{\epsilon_r \mu_r}} & 0 & \frac{i}{\sqrt{\epsilon_r \mu_r}} & 0 \\ 0 & \frac{i}{\sqrt{\epsilon_r \mu_r}} & 0 & -\frac{i}{\sqrt{\epsilon_r \mu_r}} \\ 0 & 1 & 0 & 1 \\ 1 & 0 & 1 & 0 \end{bmatrix} \tag{A.30}$$

We also need to change the eigenvalue matrix so the propagation direction is the same as in the eigenvetor matrix:

$$\lambda = \begin{bmatrix} +i\sqrt{\epsilon_r \mu_r} & 0 & 0 & 0 \\ 0 & +i\sqrt{\epsilon_r \mu_r} & 0 & 0 \\ 0 & 0 & -i\sqrt{\epsilon_r \mu_r} & 0 \\ 0 & 0 & 0 & -i\sqrt{\epsilon_r \mu_r} \end{bmatrix} \tag{A.31}$$

Now the first two columns in the matrices represents forward propagation waves and the last two columns are backward propagation waves, while the four rows represents for the electric field in $x$, $y$, magnetic field in $x$, $y$ direction, respectively. Therefore, we simplify the matrices as:

$$W = \begin{bmatrix} W_E^+ & W_E^- \\ W_H^+ & W_H^- \end{bmatrix} \tag{A.32}$$

$$e^{\lambda z'} = \begin{bmatrix} e^{\lambda^+ z'} & 0 \\ 0 & e^{\lambda^- z'} \end{bmatrix} \tag{A.33}$$

Thus, we can write the field solution:

$$\Phi(z') = \begin{bmatrix} W_E^+ & W_E^- \\ W_H^+ & W_H^- \end{bmatrix} \begin{bmatrix} e^{\lambda^+ z'} & 0 \\ 0 & e^{\lambda^- z'} \end{bmatrix} \begin{bmatrix} c^+ \\ c^- \end{bmatrix} \tag{A.34}$$

And we separated the forward and backward propagating waves.

The amplitude coefficients after connecting to transmission and reflection side become:

$$\begin{bmatrix} c_{trn} \\ 0 \end{bmatrix} = T_{total} \begin{bmatrix} W_{1E}^{+} & W_{1E}^{-} \\ W_{1H}^{+} & W_{1H}^{-} \end{bmatrix}^{-1} \begin{bmatrix} W_{superE}^{+} & W_{superE}- \\ W_{superH}^{+} & W_{superH}^{-} \end{bmatrix} \begin{bmatrix} c_{inc} \\ c_{ref} \end{bmatrix} \tag{A.35}$$

Since we rearranged the matrices, the $c_{inc}, c_{ref}, c_{trn}$ also need to be rearranged. We can rewrite the matrix with rearranged $c$ as follows:

$$\begin{bmatrix} c_{trn} \\ 0 \end{bmatrix} = W_{sub}^{-1} \begin{bmatrix} E_t \\ \tilde{H}_t \\ 0 \\ 0 \end{bmatrix} \qquad \begin{bmatrix} c_{inc} \\ c_{ref} \end{bmatrix} = W_{super}^{-1} \begin{bmatrix} E_{in} \\ \tilde{H_{in}} \\ E_r \\ \tilde{H}_r \end{bmatrix} \tag{A.36}$$

where both the $E$ field and $H$ field includes $x$ and $y$ components. Since the reflectance and transmittance can be derived by electric field, we can ignore the magnetic field input for now, $c$ then becomes

$$c_{inc} = W_{E,super}^{-1} \begin{bmatrix} E_{inx} \\ E_{iny} \end{bmatrix} \qquad c_{ref} = W_{E,super}^{-1} \begin{bmatrix} E_{rx} \\ E_{ry} \end{bmatrix} \qquad c_{trn} = W_{E,sub}^{-1} \begin{bmatrix} E_{tx} \\ E_{ty} \end{bmatrix} \tag{A.37}$$

We note that the transfer matrix does not change though we only have $E$ input. Hence, the reflected and transmitted field can be derived:

$$\begin{bmatrix} E_{rx} \\ E_{ry} \end{bmatrix} = W_{E,super} c_{ref} = -W_{E,super} \frac{C}{D} c_{inc} = -W_{E,super} \frac{C}{D} W_{E,super}^{-1} \begin{bmatrix} E_{inx} \\ E_{iny} \end{bmatrix} \tag{A.38}$$

$$\begin{bmatrix} E_{tx} \\ E_{ty} \end{bmatrix} = W_{E,sub} c_{trn} = W_{E,sub}(A c_{inc} + B c_{ref)} = W_{E,sub}(A - \frac{BC}{D}) W_{E,super}^{-1} \begin{bmatrix} E_{inx} \\ E_{iny} \end{bmatrix} \tag{A.39}$$

where

$$\begin{bmatrix} A & B \\ C & D \end{bmatrix} = T_{total} W_1^{-1} W_{super} \tag{A.40}$$

The reflectance is:

$$R = \frac{|\vec{E}_{ref}|^2}{|\vec{E}_{inc}|^2} = \frac{|E_{rx}|^2 + |E_{ry}|^2 + |E_{rz}|^2}{|E_{inx}|^2 + |E_{iny}|^2 + |E_{inz}|^2} \tag{A.41}$$

The transmittance is:

$$T = Re[\frac{\mu_{super} k_{tz}}{\mu_{sub} k_{inz}}] \frac{|\vec{E}_{trn}|^2}{|\vec{E}_{inc}|^2} = Re[\frac{\mu_{super} k_{tz}}{\mu_{sub} k_{inz}}] \frac{|E_{tx}|^2 + |E_{ty}|^2 + |E_{tz}|^2}{|E_{inx}|^2 + |E_{iny}|^2 + |E_{inz}|^2} \tag{A.42}$$

where $E_z = -\frac{\tilde{k_x} E_x + \tilde{k_y} E_y}{\tilde{k_z}}$, (obtained through solving $\frac{\partial}{\partial x}(E_{0,x} e^{i\vec{k}\vec{r}}) + \frac{\partial}{\partial y}(E_{0,y} e^{i\vec{k}\vec{r}}) + \frac{\partial}{\partial z}(E_{0,z} e^{i\vec{k}\vec{r}}) = 0$. The wavevectors $\tilde{k_x}, \tilde{k_y}, \tilde{k_z}$ have been introduced in equation B18. Since we know the incident $E$ field, we can calculate the $T$ and $R$ from the above equations. If the incident field is circular polarised,

$$\begin{bmatrix} E_{rx} \\ E_{ry} \end{bmatrix} = \frac{1}{\sqrt{2}} \begin{bmatrix} 1 \\ i \end{bmatrix} \tag{A.43}$$

### A.2.3 The instability – solve wave equation

The mode sorting method is a bit confusing and difficult to understand physically. In this section, we solve wave equations to obtain the stable matrix. Compare to last section which solves the first order differential equation, here we solve the second-order differential equation, the mode calculated is one way. For the forward and backward waves, we need to repeat the equations twice with different sign. To derive the wave equation, we can look back to the matrix B.25 and write $E$ and $H$ field separately:

$$\frac{d}{dz'} \begin{bmatrix} E_x \\ E_y \end{bmatrix} = P \begin{bmatrix} \tilde{H_x} \\ \tilde{H_y} \end{bmatrix} \qquad \frac{d}{dz'} \begin{bmatrix} \tilde{H_x} \\ \tilde{H_y} \end{bmatrix} = Q \begin{bmatrix} \tilde{H_x} \\ \tilde{H_y} \end{bmatrix} \tag{A.44}$$

where

$$P = \frac{1}{\epsilon_r} \begin{bmatrix} \tilde{k_x}\tilde{k_y} & \mu_r\epsilon_r - \tilde{k_x}^2 \\ \tilde{k_y}^2 - \mu_r\epsilon_r & -\tilde{k_x}\tilde{k_y} \end{bmatrix} \qquad Q = \frac{1}{\mu_r} \begin{bmatrix} \tilde{k_x}\tilde{k_y} & \mu_r\epsilon_r - \tilde{k_x}^2 \\ \tilde{k_y}^2 - \mu_r\epsilon_r & -\tilde{k_x}\tilde{k_y} \end{bmatrix} \tag{A.45}$$

Now we can derive a matrix wave equation:

$$\frac{d}{dz'}\frac{d}{dz'}\begin{bmatrix}E_x\\E_y\end{bmatrix} = P\begin{bmatrix}\tilde{H}_x\\\tilde{H}_y\end{bmatrix} \tag{A.46}$$

which results in

$$\frac{d^2}{dz'^2}\begin{bmatrix}E_x\\E_y\end{bmatrix} = PQ\begin{bmatrix}E_x\\E_y\end{bmatrix} \tag{A.47}$$

So we can solve the following matrix:

$$\frac{d^2}{dz'^2}\begin{bmatrix}E_x\\E_y\end{bmatrix} - \Omega^2\begin{bmatrix}E_x\\E_y\end{bmatrix} = \begin{bmatrix}0\\0\end{bmatrix} \tag{A.48}$$

, where $\Omega^2 = PQ$ The general solution to this matrix equation is:

$$\begin{bmatrix}E_x(z')\\E_y(z')\end{bmatrix} = e^{\Omega z'}a^+ + e^{-\Omega z'}a^- \tag{A.49}$$

with the propagation constants$a^+$ and $a^-$. The same as we did in last section, $e^{\Omega z'} = We^{\lambda z'}W^{-1}$. Therefore,

$$\begin{bmatrix}E_x(z')\\E_y(z')\end{bmatrix} = We^{\lambda z'}c^+ + We^{-\lambda z'}c^- \tag{A.50}$$

where $c^+ = W^{-1}a^+$ and $c^- = W^{-1}a^-$. The magnetic field solution can be derived as well:

$$\begin{bmatrix}\tilde{H_x}(z')\\\tilde{H_y}(z')\end{bmatrix} = Ve^{\lambda z'}c^+ - Ve^{-\lambda z'}c^- \tag{A.51}$$

The eigenvector matrix $V$ can be obtained through the relation between $H$ and $E$ field:

$$\frac{d}{dz'}\begin{bmatrix}\tilde{H_x}(z')\\\tilde{H_y}(z')\end{bmatrix} = Q\begin{bmatrix}E_x(z')\\E_y(z')\end{bmatrix} \tag{A.52}$$

so that $V\lambda e^{\lambda z'}c^+ + V\lambda e^{-\lambda z'}c^- = Q(We^{\lambda z'}c^+ + We^{-\lambda z'}c^-)$. Hence, we obtain $V = QW\lambda^{-1}$.

In the end we have field at $z'$:

$$\Phi(z') = \begin{bmatrix} E_x(z') \\ E_y(z') \\ \tilde{H_x}(z') \\ \tilde{H_y}(z') \end{bmatrix} = \begin{bmatrix} W & W \\ V & -V \end{bmatrix} \begin{bmatrix} e^{\lambda z'} & 0 \\ 0 & e^{-\lambda z'} \end{bmatrix} \begin{bmatrix} c^+ \\ c^- \end{bmatrix} \tag{A.53}$$

This is very similar to the one we obtained in equation B.34. They are essentially equivalent.

## A.3 Scattering Transfer Matrix

In this section, we rearrange the matrix obtained in B.53 to form the scattering matrix. The difference between scattering matrix method (SMM)and transfer matrix method (TMM) is that: the relation in TMM is:

$$\begin{bmatrix} E_{trn} \\ 0 \end{bmatrix} = M \begin{bmatrix} E_{inc} \\ E_{ref} \end{bmatrix} \tag{A.54}$$

the different rows represents opposite propagation direction. While the relation in SMM is:

$$\begin{bmatrix} E_{ref} \\ E_{trn} \end{bmatrix} = M \begin{bmatrix} E_{inc} \\ 0 \end{bmatrix} \tag{A.55}$$

The advantage of the scattering method is that, each matrix elements have its own meaning. For example, $M(1,1)$ corresponds to reflection process, while $M(2,1)$ corresponds to transmission relation. In addition, SMM is more memory efficient. For systems only have one input (incident beam), only $M(1,1)$ and $M(2,1)$ are needed, therefore it further saves the computational memory.

From the previous section, we have obtained the relation of:

$$\begin{bmatrix} W_{i+1} & W_{i+1} \\ V_{i+1} & -V_{i+1} \end{bmatrix} \begin{bmatrix} c_{i+1}^{+} \\ c_{i+1}^{-} \end{bmatrix} = \begin{bmatrix} W_i & W_i \\ V_i & -V_i \end{bmatrix} \begin{bmatrix} e^{\lambda_i z_i'} & 0 \\ 0 & e^{-\lambda_i z_i'} \end{bmatrix} \begin{bmatrix} c_i^{+} \\ c_i^{-} \end{bmatrix} \tag{A.56}$$

And the relation at the first interface:

$$\begin{bmatrix} W_i & W_i \\ V_i & -V_i \end{bmatrix} \begin{bmatrix} c_i^{+} \\ c_i^{-} \end{bmatrix} = \begin{bmatrix} W_{i-1} & W_{i-1} \\ V_{i-1} & -V_{i-1} \end{bmatrix} \begin{bmatrix} c_{i-1}(z')^{+} \\ c_{i-1}(z')^{-} \end{bmatrix} \tag{A.57}$$

here, $c_{i-1}(z')$ represents the field at the end of $i-1$ layer. Therefore, the matrix connecting the input and output ports is:

$$\begin{bmatrix} A_{i,i-1} & B_{i,i-1} \\ B_{i,i-1} & A_{i,i-1} \end{bmatrix} \begin{bmatrix} c_{i-1}(z')^{+} \\ c_{i-1}(z')^{-} \end{bmatrix} = \begin{bmatrix} e^{\lambda_i z_i'} & 0 \\ 0 & e^{-\lambda_i z_i'} \end{bmatrix}^{-1} \begin{bmatrix} A_{i,i+1} & B_{i,i+1} \\ B_{i,i+1} & A_{i,i+1} \end{bmatrix} \begin{bmatrix} c_{i+1}^{+} \\ c_{i+1}^{-} \end{bmatrix} \tag{A.58}$$

where $A_{mn} = W_m^{-1}W_n + V_m^{-1}V_n$, $B_{mn} = W_m^{-1}W_n - V_m^{-1}V_n$.

After rearrange the matrix in B.58, we obtain the scattering matrix:

$$\begin{bmatrix} c_{i-1}(z')^{-} \\ c_{i+1}^{+} \end{bmatrix} = \begin{bmatrix} S_{11}^{(i)} & S_{12}^{(i)} \\ S_{21}^{(i)} & S_{22}^{(i)} \end{bmatrix} \begin{bmatrix} c_{i-1}(z')^{+} \\ c_{i+1}^{-} \end{bmatrix} \tag{A.59}$$

with $X_i = e^{\lambda_i k_0 L_i}$, $L_i$ is the $i_{th}$ layer thickness, and:

$$\begin{aligned} S_{11}^{(i)} &= (A_{i,i-1} - X_i B_{i,i+1} A_{i,i+1}^{-1} X_i B_{i,i-1})^{-1}(X_i B_{i,i+1} A_{i,i+1}^{-1} X_i A_{i,i-1} - B_{i,i-1}) \\ S_{12}^{(i)} &= (A_{i,i-1} - X_i B_{i,i+1} A_{i,i+1}^{-1} X_i B_{i,i-1})^{-1} X_i (A_{i,i+1} - B_{i,i+1} A_{i,i+1}^{-1} - B_{i,i+1}) \\ S_{21}^{(i)} &= (A_{i,i+1} - X_i B_{i,i-1} A_{i,i-1}^{-1} X_i B_{i,i+1})^{-1} X_i (A_{i,i-1} - B_{i,i-1} A_{i,i-1}^{-1} - B_{i,i-1}) \\ S_{22}^{(i)} &= (A_{i,i+1} - X_i B_{i,i-1} A_{i,i-1}^{-1} X_i B_{i,i+1})^{-1}(X_i B_{i,i-1} A_{i,i-1}^{-1} X_i A_{i,i+1} - B_{i,i+1}) \end{aligned} \tag{A.60}$$

For the scattering matrix of the entire periodic material, we need to connect the scattering matrix of each layer in sequence. This is done by using Redheffer's star product,

instead of matrix multiplication in TMM. This is due to we rearranged the lefthand and righthand field in one column vector.

The combined matrix is:

$$S^{(i,i+1)} = S^{(i)} \otimes S^{(i+1)} = \begin{bmatrix} S_{11}^{(i,i+1)} & S_{12}^{(i,i+1)} \\ S_{21}^{(i,i+1)} & S_{22}^{(i,i+1)} \end{bmatrix} \tag{A.61}$$

$$\begin{aligned} S_{11}^{(i,i+1)} &= S_{11}^{(i)} + S_{12}^{(i)}[I - S_{11}^{(i+1)} S_{22}^{(i)}]^{-1} S_{11}^{(i+1)} S_{21}^{(i)} \\ S_{12}^{(i,i+1)} &= S_{12}^{(i)}[I - S_{11}^{(i+1)} S_{22}^{(i)}]^{-1} S_{12}^{(i+1)} \\ S_{21}^{(i,i+1)} &= S_{21}^{(i+1)}[I - S_{22}^{(i)} S_{11}^{(i+1)}]^{-1} S_{21}^{(i)} \\ S_{22}^{(i,i+1)} &= S_{22}^{(i+1)} + S_{21}^{(i+1)}[I - S_{22}^{(i)} S_{11}^{(i+1)}]^{-1} S_{22}^{(i)} S_{12}^{(i+1)} \end{aligned} \tag{A.62}$$

Therefore, the global matrix is $S_{global} = S^{super} \otimes S^{(1)} \otimes S^{(2)} \otimes ... \otimes S^{(N)} \otimes S^{(sub)}$ Since we have the relation of:

$$\begin{bmatrix} W_{super} & W_{super} \\ V_{super} & -V_{super} \end{bmatrix} \begin{bmatrix} c_{super}^{+} \\ c_{super}^{-} \end{bmatrix} = \begin{bmatrix} W_1 & W_1 \\ V_1 & -V_1 \end{bmatrix} \begin{bmatrix} c_1^{+} \\ c_1^{-} \end{bmatrix} \tag{A.63}$$

We can obtain the scattering matrix at the material lefthand side $S_{11}^{(super)} = -A_{super}^{-1} B_{super}$, $S_{12}^{(super)} = 2A_{super}^{-1}$, $S_{21}^{(super)} = 0.5(A_{super} - B_{super} A_{super}^{-1} B_{super})$ and $S_{22}^{(super)} = B_{super} A_{super}^{-1}$, where $A_{super} = W_1^{-1} W_{super} + V_1^{-1} V_{super}$ and $B_{super} = W_1^{-1} W_{super} - V_1^{-1} V_{super}$. For the material right hand side, we can obtain the similar relation of $S_{11}^{(sub)} = B_{sub} A_{sub}^{-1}$, $S_{12}^{(sub)} = 0.5(A_{sub} - B_{sub} A_{sub}^{-1} B_{sub})$, $S_{21}^{(sub)} = 2A_{sub}^{-1}$ and $S_{22}^{(sub)} = -A_{sub}^{-1} B_{sub}$, where $A_{sub} = W_n^{-1} W_{sub} + V_n^{-1} V_{sub}$ and $B_{sub} = W_n^{-1} W_{sub} - V_n^{-1} V_{sub}$, $n$ is the layer number.

We know the relation:

$$\begin{bmatrix} E_x^{ref} \\ E_y^{ref} \end{bmatrix} = W_{super} c_{ref} = W_{super} S_{11}^{(global)} c_{inc} = W_{super} S_{11}^{(global)} W_{ref}^{-1} \begin{bmatrix} E_x^{inc} \\ E_y^{inc} \end{bmatrix} \tag{A.64}$$

$$\begin{bmatrix} E_x^{trn} \\ E_y^{trn} \end{bmatrix} = W_{sub} c_{trn} = W_{sub} S_{21}^{(global)} c_{inc} = W_{sub} S_{21}^{(global)} W_{super}^{-1} \begin{bmatrix} E_x^{inc} \\ E_y^{inc} \end{bmatrix} \tag{A.65}$$

The same as introduced in B.41 and B.42, the reflectance and transmittance through the multilayer material can be then calculated.

# Appendix Two

# Third Order Nonlinearity in Nano-Porous Silicon

**This chapter is a reformatted version of my paper 'The Influence of Quantum Confinement on Third-Order Nonlinearities in Porous Silicon Thin Films', R. Wu, J. Collins, L.T. Canham, and A. Kaplan, Applied Sciences, 8(10), 1810 (2018).**

The following work aims to investigate the optical nonlinearity of nano-porous Silicon (np-Si) and compare it to crystalline Silicon (c-Si). The np-Si that has been used in the following experiments are a free-standing membrane with thickness of 15 $\mu m$ and porosity of 68%. Z-scan method was employed to investigate the nonlinearity of np-Si and c-Si. The Z-scan method was first proposed by Sheikh-Bahae and co-workers[279] in 1990s for identifying the third order nonlinearities of materials. As shown in Figure B.1, the sample is placed on a translational stage after a focusing lens, and two photodiodes (one with aperture in front for closed aperture measurements and one without aperture for open aperture measurements) are used to record the transmittance at each sample position while it is translating through the focus of a Gaussian beam. The subfigures under the setup illustrate the typical results obtained from the z-scan method: left one for

the closed aperture detection and right one for the open aperture detection. As shown in the figure, Z-scan technique gives distinguishable features on closed and open aperture transmittance, which corresponds to the nonlinear refraction and two photon absorption (TPA) processes, respectively. For nonlinearly refractive materials, a higher intensity in the centre of Gaussian beam, in comparison to its surroundings, results in a variation of the refractive index along the beam cross-section. Therefore, samples behave as a focusing or defocusing lens depending on the sign of the nonlinear refractive index, $n_2$. This effect can be observed by recording only the centre intensity of the transmitted light, which is normally accomplished by placing an aperture before a detector. In contrast, the total transmitted intensity (without aperture) carries the information about nonlinear absorption, as it records a change of the total beam intensity, which is commonly governed by the TPA.

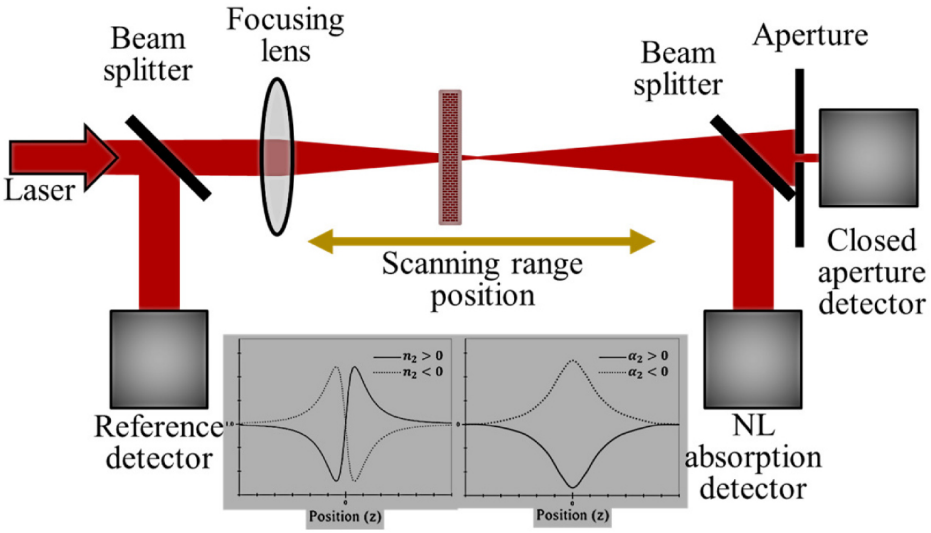


Figure B.1: Z-scan set-up. The detector with an aperture in front is for nonlinear refractive index analysis and the detector without aperture is for TPA analysis. The reference detector is used to reduce the noise and increase the precision of results[280].

The normalised transmittance, $T(z)/T_0$, was measured, where $T(z)$ is the measured

transmittance at a sample position $z$, relative to the location of the beam focus and $T_0$ is the linear transmittance. The acquired experimental data were used to retrieve the nonlinear refractive index, $n_2$, and TPA coefficient, $\beta$ of the samples.

By applying the Gaussian decomposition method, the total time-integrated transmission, $T_{open}$, for the open aperture can be expressed as[281, 282, 283]:

$$T_{open}(z) = 1 - \frac{1}{2\sqrt{2}} \frac{\beta I_0 L_{eff}}{1 + (\frac{z}{z_0})^2} \quad , \tag{B.1}$$

where $I_0$ is the on-axis peak intensity and $L_{eff} = \dfrac{1 - e^{-\alpha d}}{\alpha}$ is the effective optical length of the sample with thickness $d$ and linear absorption coefficient $\alpha$. $z$ is the sample position relative to the beam focal point, and $z_0 = 2\pi\omega_0^2/\lambda$ is the confocal parameter of the beam with waist $\omega_0$ and wavelength $\lambda$.

For the closed aperture, the transmittance is given by:

$$T_{close}(z) = 1 + \frac{4(\frac{z}{z_0})\Delta\Phi}{(1 + (\frac{z}{z_0})^2)(9 + (\frac{z}{z_0})^2)} - \frac{\beta I_0 L_{eff}}{2\sqrt{2}} \frac{(3 - (\frac{z}{z_0})^2)}{(1 + (\frac{z}{z_0})^2)(9 + (\frac{z}{z_0})^2)} \quad ; \tag{B.2}$$

here, $\Delta\Phi$ is the time-averaged phase change induced by the nonlinear refraction, which can be approximated as:

$$\Delta\Phi = \frac{2\pi}{\sqrt{2}\lambda}(1 - S)^{0.25} n_2 I_0 L_{eff} \quad , \tag{B.3}$$

where $S$ is the transmissivity of the aperture.

Figure B.2(a) and (b) show the measurements taken with the closed and open aperture, respectively, of Z-scan transmittance of the 9 $\mu$m-thick c-Si thin film, using incident fluences of 40, 54, 68 and 82 nJ. The experimental results were fitted with Eq.B.1

and Eq.B.2 to extract the TPA coefficient, $\beta$, and nonlinear refractive index, $n_2$. The fitting results suggest that $\beta = 2.9 \pm 0.9$ cm/GW, while $n_2 = 7 \pm 2 \times 10^{-6}$ cm$^2$/GW, which are comparable to those previously published elsewhere[281, 282]. The main reason for the observed uncertainties was due to the experimental error of the beam fluence determination. The fluence of the incident light did not exceed the nano-Joule range, and it was difficult to measure its exact value. The error involved in the measurements of the fluence was up to 30%. However, this should not lead to a severe numerical error and deviation from the acceptable standards for these types of experiments.

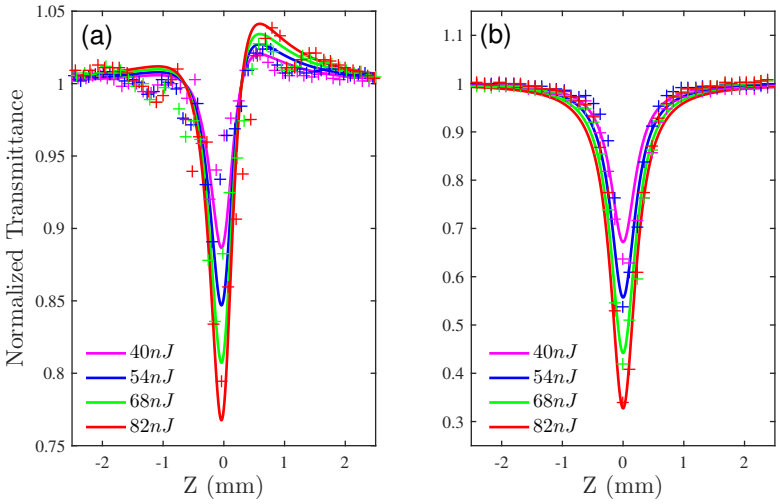


Figure B.2: The experimental (dots) and fitting (solid lines) results of the Z-scan measurements for the 9 $\mu$m-thick-c-Si sample at 800 nm, using incident fluence of 40 (magenta), 54 (blue), 68 (green) and 82 nJ (red), respectively. (a) Closed aperture Z-scan (normalised transmittance with a 500-$\mu$m aperture). (b) Open aperture Z-scan (normalised transmittance without aperture).

The experimental procedure was repeated to measure the non-linear response of a 15 $\mu$m-thick free-standing np-Si thin film, and the results are shown in Figure B.3. It is noted that the incident fluence covered a slightly different range than that used for the

c-Si's measurements. This was due to the difficulties in controlling the fluence level in such a low pulse energy range. The analysis revealed the TPA coefficient $\beta = 1.0 \pm 0.3$ cm/GW and nonlinear refractive index $n_2 = -9 \pm 3 \times 10^{-5}$ cm$^2$/GW. In comparison with that of c-Si, the TPA appeared to be slightly suppressed. However, the nonlinear refraction was greatly enhanced. Remarkably, the sign of $n_2$ was reversed to the negative in comparison to the positive value of c-Si. These findings agree with Lettieri's work[284] on np-Si, despite the fact that samples with different doping and porosity were used.

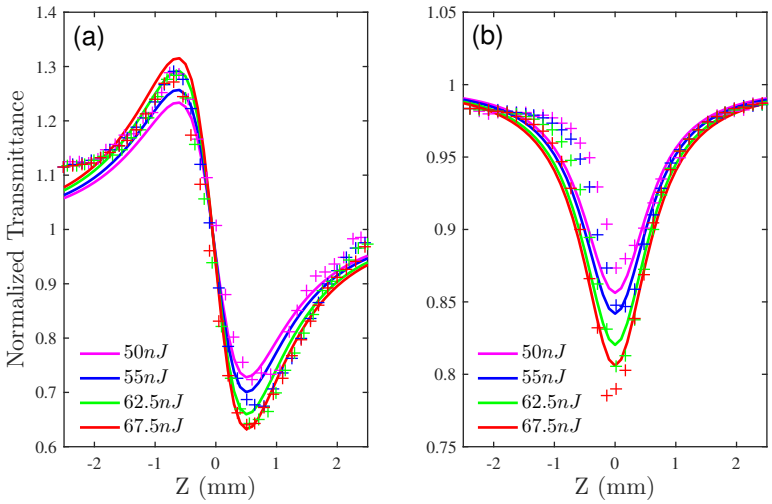


Figure B.3: The experimental (dots) and fitting (solid lines) results of the Z-scan measurements for the 15 $\mu$m-thick np-Si sample at 800 nm, using incident fluence of 50 (magenta), 55 (blue), 62.5 (green) and 67.5 nJ (red), respectively. (a) Closed aperture Z-scan (normalised transmittance with a 500-$\mu$m aperture). (b) Open aperture Z-scan (normalised transmittance without aperture).

To further compare the nonlinear refraction process between c-Si and np-Si, the nonlinear phase shift $\Delta\Phi$ for different incident fluences is plotted in Figure B.4. The squares represent the experimental values $\Delta\Phi = \Delta T_{peak-valley}$, and the solid lines are calculated from Eq.B.3 with the values of $n_2$ obtained from the Z-scan measurements. It

can be seen that the phase shift for np-Si was at least four-times higher and changed faster as a function of the fluence than that of the c-Si, which further confirmed the enhancement of the nonlinear refraction.

The nano-porous silicon used in this work consists of quasi-one-dimensional wires with a mean diameter of 10 nm. Therefore, the motion of the charged carriers is moderately confined. As a result of the confinement effect, the optical matrix element, defining the third order-nonlinear susceptibility ($\chi^3$), increases. S. Lettieri et al.[284] proposed a computational model to calculate $\chi^3$ as a function of quantum wire radius. It was suggested that for a quantum wire with a 2–3.5-nm radius, the real part of $\chi^3$ is about four orders of magnitude greater than in the bulk. From the experimental results, $\Re(\chi^3) = \frac{4}{3} n_2 n_0^2 \epsilon_0 c = 1.2 \times 10^{-19}$ m$^2$/V$^2$ for np-Si was obtained, which is an order of magnitude greater than $3.37 \times 10^{-20}$ m$^2$/V$^2$ for c-Si. The difference of this result as compared to Lettieri's work might be the weaker confinement in the samples.

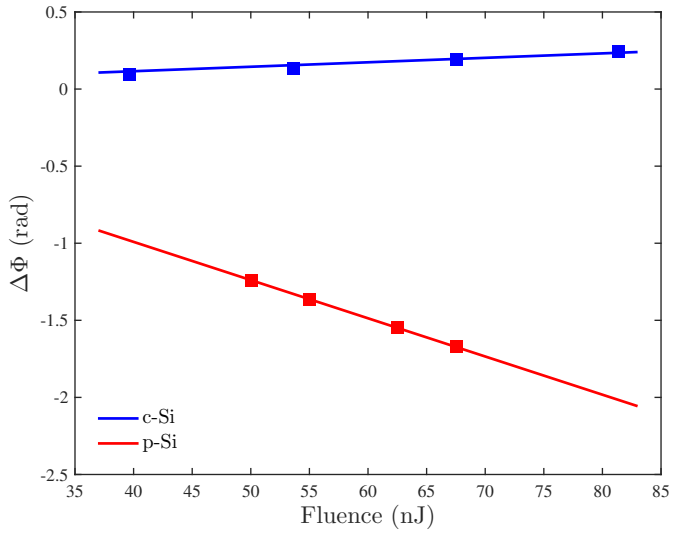


Figure B.4: Nonlinear phase shift, $\Delta\Phi$, as a function of the incident fluence for c-Si (blue) and np-Si (red). The squares represent the experimental results, and the solid lines are calculated with $n_2$ obtained from the fitting results.

Moreover, in addition to the confinement, the optical Stark effect plays an important role in low-dimensional systems and can cause the sign reversal of $n_2$ (proportional to $\Re(\chi^3)$) in np-Si. To demonstrate this effect, D. Cotter et al. employed the sum-over-states method for the calculation of $\chi^3$ of a sphere in a quantum confinement regime as a function of the sphere radius[285]. The results demonstrated that $\Re(\chi^3)$ is always negative with positive values of $\Im(\chi^3)$. This behaviour is different from the bulk materials, which exhibit negative values $\Re(\chi^3)$ only for photon frequencies very close to the absorption edge.

The experimental results also show a suppression of the TPA process for an 800-nm photon wavelength and smaller $\beta$ in np-Si with respect to c-Si. However, it should be noted that the TPA coefficient evaluated in this work is an effective value of np-Si. Due to the dilution of silicon with air, the effective $\beta$ is smaller than that of the silicon constituent, despite possible enhancement by the quantum confinement effect.

# Bibliography


[1] S. Sundaram and E. Mazur. "Inducing and probing non-thermal transitions in semiconductors using femtosecond laser pulses". In: *Nature Materials* 1.4 (2002), pp. 217–224.

[2] M. Bertolotti. *The history of the laser*. CRC press, 2004.

[3] J. Hecht. "A short history of laser development". In: *Applied Optics* 49.25 (2010), F99–F122.

[4] J. Fleck Jr. "Ultrashort-pulse generation by Q-switched lasers". In: *Physical Review B* 1.1 (1970), p. 84.

[5] G. Steinmeyer et al. "Frontiers in ultrashort pulse generation: pushing the limits in linear and nonlinear optics". In: *Science* 286.5444 (1999), pp. 1507–1512.

[6] M. Maiuri, M. Garavelli, and G. Cerullo. "Ultrafast spectroscopy: State of the art and open challenges". In: *Journal of the American Chemical Society* 142.1 (2019), pp. 3–15.

[7] H. Abraham and J. Lemoine. "Disparition instantanée du phénomène de Kerr". In: *Comptes Rendus Hebdomadaires des Seances de Academie des Sciences D* 129 (1899), pp. 206–208.

[8] M. Chergui and J. M. Thomas. *From structure to structural dynamics: Ahmed Zewail's legacy*. 2017.

[9] E. Archbold, D. Harper, and T. Hughes. "Time-resolved spectroscopy of laser-generated microplasmas". In: *British Journal of Applied Physics* 15.11 (1964), p. 1321.

[10] C. Shank, E. Ippen, and R. Bersohn. "Time-resolved spectroscopy of hemoglobin and its complexes with subpicosecond optical pulses". In: *Science* 193.4247 (1976), pp. 50–51.

[11] I. Inoue et al. "Observation of femtosecond X-ray interactions with matter using an X-ray–X-ray pump–probe scheme". In: *Proceedings of the National Academy of Sciences* 113.6 (2016), pp. 1492–1497.

[12] K. Lui and F. Hegmann. "Ultrafast carrier relaxation in radiation-damaged silicon on sapphire studied by optical-pump–terahertz-probe experiments". In: *Applied Physics Letters* 78.22 (2001), pp. 3478–3480.

[13] S.-H. Shim and M. T. Zanni. "How to turn your pump–probe instrument into a multidimensional spectrometer: 2D IR and Vis spectroscopies via pulse shaping". In: *Physical Chemistry Chemical Physics* 11.5 (2009), pp. 748–761.

[14] S. Rapp et al. "Ultrafast pump-probe ellipsometry setup for the measurement of transient optical properties during laser ablation". In: *Optics Express* 24.16 (2016), pp. 17572–17592.

[15] M. C. Fischer et al. "Invited review article: pump-probe microscopy". In: *Review of Scientific Instruments* 87.3 (2016), p. 031101.

[16] D. P. Millar. "Time-resolved fluorescence spectroscopy". In: *Current Opinion in Structural Biology* 6.5 (1996), pp. 637–642.

[17] M. Lanir and K. J. Riley. "Performance of PV HgCdTe arrays for 1-14-$\mu$m applications". In: *IEEE Transactions on Electron Devices* 29.2 (1982), pp. 274–279.

[18] E. Fitzgerald and L. Kimerling. “Silicon-based microphotonics and integrated optoelectronics”. In: *MRS Bulletin* 23.4 (1998), pp. 39–47.

[19] B. Jalali and S. Fathpour. “Silicon photonics”. In: *Journal of Lightwave Technology* 24.12 (2006), pp. 4600–4615.

[20] M. E. Weeks. “The discovery of the elements. XII. Other elements isolated with the aid of potassium and sodium: Beryllium, boron, silicon, and aluminum”. In: *Journal of Chemical Education* 9.8 (1932), p. 1386.

[21] E. Sirtl. “Milestones in Silicon Semiconductor Technology”. In: *Methods and Materials in Microelectronic Technology*. Springer, 1984, pp. 19–35.

[22] R. G. Arns. “The other transistor: early history of the metal-oxide semiconductor field-effect transistor”. In: *Engineering Science & Education Journal* 7.5 (1998), pp. 233–240.

[23] M. J. Heck et al. “Hybrid silicon photonic integrated circuit technology”. In: *IEEE Journal of Selected Topics in Quantum Electronics* 19.4 (2012), pp. 6100117–6100117.

[24] A. J. Nozik. “Nanoscience and nanostructures for photovoltaics and solar fuels”. In: *Nano Letters* 10.8 (2010), pp. 2735–2741.

[25] F. Priolo et al. “Silicon nanostructures for photonics and photovoltaics”. In: *Nature Nanotechnology* 9.1 (2014), pp. 19–32.

[26] C. Smith and D. Binks. “Multiple exciton generation in colloidal nanocrystals”. In: *Nanomaterials* 4.1 (2014), pp. 19–45.

[27] K.-G. Gan et al. “Ultrafast valence intersubband hole relaxation in InGaN multiple-quantum-well laser diodes”. In: *Applied Physics Letters* 84.23 (2004), pp. 4675–4677.

[28] K. W. Williams et al. "Ultrafast and band-selective Auger recombination in InGaN quantum wells". In: *Applied Physics Letters* 108.14 (2016), p. 141105.

[29] A. Zakar et al. "Carrier dynamics and surface vibration-assisted Auger recombination in porous silicon". In: *Physical Review B* 97.15 (2018), p. 155203.

[30] A. Aydinli et al. "Induced absorption in silicon under intense laser excitation: evidence for a self-confined plasma". In: *Physical Review Letters* 46.25 (1981), p. 1640.

[31] J. Liu, H. Kurz, and N. Bloembergen. "Picosecond time-resolved plasma and temperature-induced changes of reflectivity and transmission in silicon". In: *Applied Physics Letters* 41.7 (1982), pp. 643–646.

[32] T. Tiedje. "Time-resolved charge transport in hydrogenated amorphous silicon". In: *The Physics of Hydrogenated Amorphous Silicon II* (1984), pp. 261–300.

[33] C. H. Wang, K. Misiakos, and A. Neugroschel. "Minority-carrier transport parameters in n-type silicon". In: *IEEE Transactions on Electron Devices* 37.5 (1990), pp. 1314–1322.

[34] L. T. Canham. "Silicon quantum wire array fabrication by electrochemical and chemical dissolution of wafers". In: *Applied Physics Letters* 57.10 (1990), pp. 1046–1048.

[35] L. Canham. *Handbook of porous silicon*. Springer, 2014.

[36] W. Sun et al. "A Three-Dimensional Porous Silicon p–n Diode for Betavoltaics and Photovoltaics". In: *Advanced Materials* 17.10 (2005), pp. 1230–1233.

[37] V. Aroutiounian, K. Martirosyan, and P. Soukiassian. "Almost zero reflectance of a silicon oxynitride/porous silicon double layer antireflection coating for silicon photovoltaic cells". In: *Journal of Physics D: Applied Physics* 39.8 (2006), p. 1623.

[38] M. Wolkin et al. "Electronic states and luminescence in porous silicon quantum dots: the role of oxygen". In: *Physical Review Letters* 82.1 (1999), p. 197.

[39] A. Cullis, L. T. Canham, and P. Calcott. "The structural and luminescence properties of porous silicon". In: *Journal of Applied Physics* 82.3 (1997), pp. 909–965.

[40] S. J. Park et al. "All-optical modulation in mid-wavelength infrared using porous si membranes". In: *Scientific Reports* 6.1 (2016), pp. 1–8.

[41] L. Khriachtchev. *Silicon Nanophotonics: Basic Principles, Present Status, and Perspectives*. CRC Press, 2016.

[42] V. Agarwal, M. E. Mora-Ramos, and B. Alvarado-Tenorio. "Optical properties of multilayered Period-Doubling and Rudin-Shapiro porous silicon dielectric heterostructures". In: *Photonics and Nanostructures-Fundamentals and Applications* 7.2 (2009), pp. 63–68.

[43] K. Kim and T. E. Murphy. "Porous silicon integrated Mach-Zehnder interferometer waveguide for biological and chemical sensing". In: *Optics Express* 21.17 (2013), pp. 19488–19497.

[44] P. Lalanne and G. M. Morris. "Design, fabrication, and characterization of subwavelength periodic structures for semiconductor antireflection coating in the visible domain". In: *Developments in Optical Component Coatings*. Vol. 2776. International Society for Optics and Photonics. 1996, pp. 300–309.

[45] H. Ouyang, C. C. Striemer, and P. M. Fauchet. "Quantitative analysis of the sensitivity of porous silicon optical biosensors". In: *Applied Physics Letters* 88.16 (2006), p. 163108.

[46] G. Smestad, M. Kunst, and C. Vial. "Photovoltaic response in electrochemically prepared photoluminescent porous silicon". In: *Solar Energy Materials and Solar Cells* 26.4 (1992), pp. 277–283.

[47] I. Mihalcescu, J. Vial, and R. Romestain. "Carrier localization in porous silicon investigated by time-resolved luminescence analysis". In: *Journal of Applied Physics* 80.4 (1996), pp. 2404–2411.

[48] Y. Fang et al. "Mid-infrared photonics using 2D materials: status and challenges". In: *Laser & Photonics Reviews* 14.1 (2020), p. 1900098.

[49] R. Wu et al. "Demonstration of time-of-flight technique with all-optical modulation and MCT detection in SWIR/MWIR range". In: *Emerging Imaging and Sensing Technologies for Security and Defence III; and Unmanned Sensors, Systems, and Countermeasures*. Vol. 10799. International Society for Optics and Photonics. 2018, p. 1079904.

[50] S. Aggarwal. "Principles of remote sensing". In: *Satellite remote sensing and GIS applications in agricultural meteorology* 23 (2004), pp. 23–28.

[51] A. Begum, A. Hussain, and A. Rahman. "Effect of deposition temperature on the structural and optical properties of chemically prepared nanocrystalline lead selenide thin films". In: *Beilstein Journal of Nanotechnology* 3.1 (2012), pp. 438–443.

[52] R. Carter III, N. Lindsay, and D. Beduhn. "A solution to baseline uncertainty due to MCT detector nonlinearity in FT-IR". In: *Applied Spectroscopy* 44.7 (1990), pp. 1147–1151.

[53] J. Zhou et al. "Room-temperature long-wave infrared detector with thin double layers of amorphous germanium and amorphous silicon". In: *Optics Express* 27.25 (2019), pp. 37056–37064.

[54] A. M. Ahmed and A. Mehaney. "Ultra-high sensitive 1D porous silicon photonic crystal sensor based on the coupling of Tamm/Fano resonances in the mid-infrared region". In: *Scientific Reports* 9.1 (2019), pp. 1–9.

[55] B. King and M. J. Sailor. "Medium-wavelength infrared gas sensing with electrochemically fabricated porous silicon optical rugate filters". In: *Journal of Nanophotonics* 5.1 (2011), p. 051510.

[56] H. Yu et al. "Plasmon-enhanced light–matter interactions and applications". In: *npj Computational Materials* 5.1 (2019), pp. 1–14.

[57] N. Zhou et al. "Plasmon-enhanced light harvesting: applications in enhanced photocatalysis, photodynamic therapy and photovoltaics". In: *RSC Advances* 5.37 (2015), pp. 29076–29097.

[58] Z. Yin and F. Smith. "Optical dielectric function and infrared absorption of hydrogenated amorphous silicon nitride films: Experimental results and effective-medium-approximation analysis". In: *Physical Review B* 42.6 (1990), p. 3666.

[59] F. Smith. "Optical constants of a hydrogenated amorphous carbon film". In: *Journal of Applied Physics* 55.3 (1984), pp. 764–771.

[60] E. Hecht. *Optics*. Addison-Wesley World Student Series. Addison-Wesley, 1998.

[61] M. Born and E. Wolf. *Principal of optics*. Pergamon Press, Oxford, 1968.

[62] L. Wang and S. Rokhlin. "Stable reformulation of transfer matrix method for wave propagation in layered anisotropic media". In: *Ultrasonics* 39.6 (2001), pp. 413–424.

[63] R. W. Boyd. *Nonlinear Optics*. Elsevier, 2008.

[64] C. Baune et al. "Strongly squeezed states at 532 nm based on frequency up-conversion". In: *Optics Express* 23.12 (2015), pp. 16035–16041.

[65] A. Borne. "Triple photons through third-order nonlinear optics". PhD thesis. Grenoble, 2014.

[66] K. Y. Spasibko et al. "Multiphoton effects enhanced due to ultrafast photon-number fluctuations". In: *Physical Review Letters* 119.22 (2017), p. 223603.

[67] M. Cazzanelli and J. Schilling. "Second order optical nonlinearity in silicon by symmetry breaking". In: *Applied Physics Reviews* 3.1 (2016), p. 011104.

[68] D. Ninno, P. Maddalena, and G. Di Francia. "Nonlinear optical properties of porous silicon". In: *Structural and Optical Properties of Porous Silicon Nanostructures*. Gordon & Breach Netherlands, 1997, pp. 111–131.

[69] W. S. Martins et al. "Two-beam nonlinear Kerr effect to stabilize laser frequency with sub-Doppler resolution". In: *Applied Optics* 51.21 (2012), pp. 5080–5084.

[70] M. Massicotte et al. "Hot carriers in graphene–fundamentals and applications". In: *Nanoscale* 13.18 (2021), pp. 8376–8411.

[71] M. Van Exter and D. Grischkowsky. "Carrier dynamics of electrons and holes in moderately doped silicon". In: *Physical Review B* 41.17 (1990), p. 12140.

[72] S. Mathias et al. "Ultrafast element-specific magnetization dynamics of complex magnetic materials on a table-top". In: *Journal of Electron Spectroscopy and Related Phenomena* 189 (2013), pp. 164–170.

[73] T. C. Choy. *Effective medium theory: principles and applications*. Vol. 165. Oxford University Press, 2015.

[74] S. Das et al. "Physics of electrostatic resonance with negative permittivity and imaginary index of refraction for illuminated plasmoid in the experimental set up for microwave near field applicator". In: *Fundamental Journal of Modern Physics* 5.2 (2013), pp. 19–46.

[75] M. S. Rogalski and S. B. Palmer. *Solid State Physics*. CRC Press, 2000.

[76] B. Felderhof, G. Ford, and E. Cohen. "The Clausius-Mossotti formula and its nonlocal generalization for a dielectric suspension of spherical inclusions". In: *Journal of Statistical Physics* 33.2 (1983), pp. 241–260.

[77] A. H. Sihvola. *Electromagnetic mixing formulas and applications*. 47. Iet, 1999.

[78] Y. Lee et al. "Engineering Electronic Band Structure of Indium-doped $Cd_{1-x}Mg_xO$ Alloys for Solar Power Conversion Applications". In: *Energy Technology* 6.1 (2018), pp. 122–126.

[79] D. Oka et al. "Anion-Substitution-Induced Non-Rigid Variation of Band Structure in $SrNbO_{3-x}N_x$ Epitaxial Thin Films". In: *ACS Applied Materials & Interfaces* (2018).

[80] T. Heilpern et al. "Determination of hot carrier energy distributions from inversion of ultrafast pump-probe reflectivity measurements". In: *Nature Communications* 9.1 (2018), p. 1853.

[81] J.-C. Diels and W. Rudolph. *Ultrashort laser pulse phenomena*. Elsevier, 2006.

[82] O. Svelto and D. C. Hanna. *Principles of lasers*. Vol. 4. Springer, 1998.

[83] W. Rapoport and C. P. Khattak. "Titanium sapphire laser characteristics". In: *Applied Optics* 27.13 (1988), pp. 2677–2684.

[84] H. A. Haus. "Mode-locking of lasers". In: *IEEE Journal of Selected Topics in Quantum Electronics* 6.6 (2000), pp. 1173–1185.

[85] J. Jin. "Dimensional metrology using the optical comb of a mode-locked laser". In: *Measurement Science and Technology* 27.2 (2015), p. 022001.

[86] D. Hanna, B. Luther-Davies, and R. Smith. "Active Q switching technique for producing high laser power in a single longitudinal mode". In: *Electronics Letters* 8.15 (1972), pp. 369–370.

[87] Coherent. *Legend elite user manual*. 2012.

[88] X. Zhang et al. "Optimization of Cr-doped saturable-absorber Q-switched lasers". In: *IEEE Journal of Quantum Electronics* 33.12 (1997), pp. 2286–2294.

[89] G. Cerullo and S. De Silvestri. "Ultrafast optical parametric amplifiers". In: *Review of Scientific Instruments* 74.1 (2003), pp. 1–18.

[90] C. Manzoni and G. Cerullo. "Design criteria for ultrafast optical parametric amplifiers". In: *Journal of Optics* 18.10 (2016), p. 103501.

[91] G. Cerullo et al. "Time-resolved methods in biophysics. 4. Broadband pump–probe spectroscopy system with sub-20 fs temporal resolution for the study of energy transfer processes in photosynthesis". In: *Photochemical & Photobiological Sciences* 6.2 (2007), pp. 135–144.

[92] P. Makuła, M. Pacia, and W. Macyk. *How to correctly determine the band gap energy of modified semiconductor photocatalysts based on UV–Vis spectra*. 2018.

[93] R. Chang. *Surface enhanced Raman scattering*. Springer Science & Business Media, 2013.

[94] S.-Y. Ding et al. "Electromagnetic theories of surface-enhanced Raman spectroscopy". In: *Chemical Society Reviews* 46.13 (2017), pp. 4042–4076.

[95] H. Dridi, L. Haji, and A. Moadhen. "Rough SERS substrate based on gold coated porous silicon layer prepared on the silicon backside surface". In: *Superlattices and Microstructures* 104 (2017), pp. 266–270.

[96] L. Zhang. "Self-assembly Ag nanoparticle monolayer film as SERS Substrate for pesticide detection". In: *Applied Surface Science* 270 (2013), pp. 292–294.

[97] M. Balucani et al. "Porous silicon solar cells". In: *Nanotechnology (IEEE-NANO), 2015 IEEE 15th International Conference on*. IEEE. 2015, pp. 724–727.

[98] R. Smith and S. Collins. "Porous silicon formation mechanisms". In: *Journal of Applied Physics* 71.8 (1992), R1–R22.

[99] M. De la Mora et al. "Porous Silicon Biosensors". In: *State of the Art in Biosensors-General Aspects*. InTech, 2013.

[100] P. V. Antonov, M. R. Zuiddam, and J. W. Frenken. "Fabrication of high-aspect ratio silicon nanopillars for tribological experiments". In: *Journal of Micro/Nanolithography, MEMS, and MOEMS* 14.4 (2015), p. 044506.

[101] V. U. Desai, J. G. Hartley, and N. C. Cady. "Electron beam lithography patterned hydrogen silsesquioxane resist as a mandrel for self-aligned double patterning application". In: *Journal of Vacuum Science & Technology B, Nanotechnology and Microelectronics: Materials, Processing, Measurement, and Phenomena* 34.6 (2016), p. 061601.

[102] S. Dhanekar and S. Jain. "Porous silicon biosensor: Current status". In: *Biosensors and Bioelectronics* 41 (2013), pp. 54–64.

[103] E. Muñoz et al. "Photoelectrochemical reduction of nitrate ions on porous silicon and different silicon modified electrodes". In: *Journal of the Chilean Chemical Society* 56.3 (2011), pp. 781–785.

[104] U. Bockelmann and G. Bastard. "Phonon scattering and energy relaxation in two-, one-, and zero-dimensional electron gases". In: *Physical Review B* 42.14 (1990), p. 8947.

[105] P. Han and G. Bester. "Carrier relaxation in colloidal nanocrystals: Bridging large electronic energy gaps by low-energy vibrations". In: *Physical Review B* 91.8 (2015), p. 085305.

[106] S. Xu et al. "Hole intraband relaxation in strongly confined quantum dots: Revisiting the phonon bottleneck problem". In: *Physical Review B* 65.4 (2002), p. 045319.

[107] A. Sa'Ar et al. "Resonant coupling between surface vibrations and electronic states in silicon nanocrystals at the strong confinement regime". In: *Nano Letters* 5.12 (2005), pp. 2443–2447.

[108] A. Saar. "Photoluminescence from silicon nanostructures: the mutual role of quantum confinement and surface chemistry". In: *Journal of Nanophotonics* 3.1 (2009), pp. 032501–032501.

[109] A. Sa'Ar et al. "The role of quantum confinement and surface chemistry in silicon nanocrystals at the strong confinement regime". In: *Physica Status Solidi A* 204.5 (2007), pp. 1491–1496.

[110] M. Mahdouani, R. Bourguiga, and S. Jaziri. "Polaronic states in Si nanocrystals embedded in $SiO_2$ matrix". In: *Physica E: Low-dimensional Systems and Nanostructures* 41.2 (2008), pp. 228–234.

[111] O. Bisi, S. Ossicini, and L. Pavesi. "Porous silicon: a quantum sponge structure for silicon based optoelectronics". In: *Surface Science Reports* 38.1 (2000), pp. 1–126.

[112] J. Joo et al. "Enhanced quantum yield of photoluminescent porous silicon prepared by supercritical drying". In: *Applied Physics Letters* 108.15 (2016), p. 153111.

[113] A. Campos, J. Torres, and J. Giraldo. "Porous silicon dielectric function modeling from effective medium theories". In: *Surface Review and Letters* 9 (2002), pp. 1631–1635.

[114] W. He et al. "Determination of excitation profile and dielectric function spatial nonuniformity in porous silicon by using WKB approach". In: *Optics Express* 22.22 (2014), pp. 27123–27135.

[115] M. Y. Koledintseva, R. E. DuBroff, and R. W. Schwartz. "A Maxwell Garnett model for dielectric mixtures containing conducting particles at optical frequencies". In: *Progress In Electromagnetics Research* 63 (2006), pp. 223–242.

[116] G. M. Hale and Querry. "Optical constants of water in the 200-nm to 200-$\mu$m wavelength region". In: *Applied Optics* 12 (1973), pp. 555–563.

[117] W. Spitzer and H. Fan. "Determination of optical constants and carrier effective mass of semiconductors". In: *Physical Review* 106.5 (1957), p. 882.

[118] W. He et al. "High-frequency conductivity of optically excited charge carriers in hydrogenated nanocrystalline silicon investigated by spectroscopic femtosecond pump–probe reflectivity measurements". In: *Thin Solid Films* 592 (2015), pp. 287–291.

[119] A. J. Sabbah and D. M. Riffe. "Measurement of silicon surface recombination velocity using ultrafast pump–probe reflectivity in the near infrared". In: *Journal of Applied Physics* 88.11 (2000), p. 6954.

[120] B. G. Lee et al. "Quasi-Direct Optical Transitions in Silicon Nanocrystals with Intensity Exceeding the Bulk". In: *Nano Letters* 16.3 (2016), pp. 1583–1589.

[121] M. Combescot and R. Combescot. "Conductivity relaxation time due to electron-hole collisions in optically excited semiconductors". In: *Physical Review B* 35.15 (May 1987), p. 7986.

[122] J. J. Sakurai. *Modern Quantum Mechanics*. Addison-Wesley, 1993.

[123] J. M. Ziman. *Principles of the Theory of Solids*. Cambridge University Press, 1972.

[124] R. A. Soref and B. R. Bennett. "Electrooptical Effects in Silicon". In: *IEEE Journal of Quantum Electronics* QE-23.1 (1987), p. 123.

[125] S. Oguz, D. A. Anderson, and W. Paul. "Reversible changes in the oscillator strengths of Si-H vibrations in a-Si:H induced by $He^+$-ion bombardment". In: *Physical Review B* 22.2 (July 1980), p. 880.

[126] M. Brodsky, M. Cardona, and J. Cuomo. "Infrared and Raman spectra of the silicon-hydrogen bonds in amorphous silicon prepared by glow discharge and sputtering". In: *Physical Review B* 16.8 (1977), p. 3556.

[127] H. Eichler et al. "Laser-induced free-carrier and temperature gratings in silicon". In: *Physical Review B* 36.6 (1987), p. 3247.

[128] J. Linnros and V. Grivickas. "Carrier-diffusion measuremnts in silicon with a Fourier-tramsient-grating method". In: *Physical Review B* 50.23 (1994), p. 16943.

[129] R. Tomasiunas et al. "Carrier diffusion in porous silicon studied by transient laser-induced grating spectroscopy". In: *Journal of Applied Physics* 79.5 (1996), pp. 2481–2486.

[130] R. Schwarz et al. "Photocarrier grating technique in mesoporous silicon". In: *Thin Solid Films* 255.1 (1995), pp. 23–26.

[131] V. Mizeikis et al. "Contactless characterization of porous silicon structures by four-wave mixing and microwave techniques". In: *Journal of Porous Materials* 7.1-3 (2000), pp. 303–306.

[132] M. Capizzi et al. "Electron-hole plasma in direct-gap $Ga_{1-x}Al_x$ As and $k$-selection rule". In: *Physical Review B* 29.4 (Feb. 1984), pp. 2028–2035.

[133] W. Shockley and W. Read Jr. "Statistics of the recombinations of holes and electrons". In: *Physical Review* 87.5 (1952), p. 835.

[134] R. Hall. "Recombination processes in semiconductors". In: *Proceedings of the IEE-Part B: Electronic and Communication Engineering* 106.17 (1959), pp. 923–931.

[135] A. J. Sabbah and D. M. Riffe. "Femtosecond pump-probe reflectivity study of silicon carrier dynamics". In: *Physical Review B* 66 (2002), p. 165217.

[136] P. T. Landsberg. "Trap-Auger recombination in silicon of low carrier densities". In: *Applied Physics Letters* 50 (1987), p. 745.

[137] W. He et al. "Determination of recombination coefficients for nanocrystalline silicon embedded in hydrogenated amorphous silicon". In: *Optics Letters* 40.16 (Aug. 2015), pp. 3889–3892.

[138] E. Yablonovitch and T. Gmitter. "Auger recombination in silicon at low carrier densities". In: *Applied Physics Letters* 49.10 (1986), pp. 587–589.

[139] P. Maly et al. "Transmission study of picosecond photocarrier dynamics in free-standing porous silicon". In: *Solid State Communications* 89.8 (1994), pp. 709–712.

[140] J. von Behren et al. "The femtosecond optical response of porous, amorphous and crystalline silicon". In: *Journal of Non-Crystalline Solids* 198-200 (1996), pp. 957–960.

[141] D. B. Mawhinney, J. A. Glass, and J. T. Yates. "FTIR study of the oxidation of porous silicon". In: *The Journal of Physical Chemistry B* 101 (1997), pp. 1202–1206.

[142] V. Dubin, F. Ozanam, and J.-N. Chazalviel. "In situ luminescence and IR study of porous silicon during and after anodic oxidation". In: *Thin Solid Films* 255 (1995), pp. 87–91.

[143] Y. J. Chabai and S. B. Christman. "Evidence of dissociation of water on the Si(100)2×1 surface". In: *Physical Review B* 29 (1984), pp. 6974–6976.

[144] J. Dziewior and W. Schmid. "Auger coefficients for highly doped and highly excited silicon". In: *Applied Physics Letters* 31.5 (1977), pp. 346–348.

[145] M. J. Kerr and A. Cuevas. "General parameterization of Auger recombination in crystalline silicon". In: *Journal of Applied Physics* 91.4 (2002), p. 2473.

[146] D. B. Laks, G. F. Neumark, and S. T. Pantelides. "Accurate interband-Auger-recombination rates in silicon". In: *Physical Review B* 42.8 (1990), p. 5176.

[147] I. Andrianov and P. Saalfrank. "Theoretical study of vibration-phonon coupling of H adsorbed on a Si(100) surface". In: *The Journal of Chemical Physics* 124 (2006), p. 034710.

[148] G. Davies et al. "Three phonon decay mode of the 1136cm$^1$ $\nu_3$ vibration of oxygen in silicon". In: *Physical Review B* 81 (2010), p. 033201.

[149] K. W. Jobson et al. "Relaxation processes of the $Ge-H$ stretch modes in hydrogenated amorphous germanium". In: *Physical Review B* 73 (15 Apr. 2006), p. 155202.

[150] R. Gereth and K. Hubner. "Phonon Mean Free Path in Silicon Between 77 and 250 K". In: *Physical Review* 134.1A (1964), A231.

[151] D. Sands, K. M. Brunson, and M. H. Tayarani-Najaran. "Measured intrinsic defect density throughout the entire band gap at the <100> $Si/SiO_2$ interface". In: *Semiconductor Science and Technology* 7.8 (1992), pp. 1091–1096.

[152] P. M. Lenahan, N. A. Bohna, and J. P. Campbell. "Radiation-induced interface traps in MOS devices: capture cross section and density of states of $P_{b1}$ silicon dangling bond centers". In: *IEEE Transactions on Nuclear Science* 49.6 (2002), pp. 2708–2712.

[153] S. F. Preble et al. "Ultrafast all-optical modulation on a silicon chip". In: *Optics Letters* 30.21 (2005), pp. 2891–2893.

[154] H. Rong et al. "A continuous-wave Raman silicon laser". In: *Nature* 433.7027 (2005), p. 725.

[155] B. R. Koch et al. "Integrated silicon photonic laser sources for telecom and datacom". In: *National Fiber Optic Engineers Conference*. Optical Society of America. 2013, PDP5C–8.

[156] A. Liu et al. "A high-speed silicon optical modulator based on a metal–oxide–semiconductor capacitor". In: *Nature* 427.6975 (2004), p. 615.

[157] S. Luryi, A. Kastalsky, and J. C. Bean. "New infrared detector on a silicon chip". In: *IEEE Transactions on Electron Devices* 31.9 (1984), pp. 1135–1139.

[158] R. Wu et al. "Demonstration of time-of-flight technique with all-optical modulation and MCT detection in SWIR/MWIR range". In: *Proc. SPIE 10799, Emerging Imaging and Sensing Technologies for Security and Defence III*. Vol. 10799. 2018.

[159] G. T. Reed and A. P. Knights. *Silicon photonics: an introduction*. John Wiley & Sons, 2004.

[160] R. Soref and B. Bennett. "Electrooptical effects in silicon". In: *IEEE Journal of Quantum Electronics* 23.1 (1987), pp. 123–129.

[161] G. Cocorullo and I. Rendina. "Thermo-optical modulation at 1.5 $\mu$m in silicon etalon". In: *Electronics Letters* 28.1 (1992), pp. 83–85.

[162] D. Martın-Sánchez et al. "Thermo-Optic Coefficient of Porous Silicon in the Infrared Region and Oxidation Process at Low Temperatures". In: *Journal of The Electrochemical Society* 166 (2019), B355–B359.

[163] D. Thomson et al. "Optical detection and modulation at 2 $\mu$m-2.5 $\mu$m in silicon". In: *Optics Express* 22.9 (2014), pp. 10825–10830.

[164] G. T. Reed et al. "Silicon optical modulators". In: *Nature Photonics* 4.8 (2010), p. 518.

[165] V. R. Almeida, Q. Xu, and M. Lipson. "Ultrafast integrated semiconductor optical modulator based on the plasma-dispersion effect". In: *Optics Letters* 30.18 (2005), pp. 2403–2405.

[166] V. R. Almeida et al. "All-optical control of light on a silicon chip". In: *Nature* 431.7012 (2004), p. 1081.

[167] T. Tanabe et al. "Fast all-optical switching using ion-implanted silicon photonic crystal nanocavities". In: *Applied Physics Letters* 90.3 (2007), p. 031115.

[168] R. Soref. "Mid-infrared photonics in silicon and germanium". In: *Nature Photonics* 4.8 (2010), p. 495.

[169] A. Hoffman and C. Gmachl. "Extending opportunities". In: *Nature Photonics* 6 (2012), p. 407.

[170] R. Lange and P. Seitz. "Solid-state time-of-flight range camera". In: *IEEE Journal of Quantum Electronics* 37.3 (Mar. 2001), pp. 390–397. ISSN: 0018-9197.

[171] P. Besl. "Active optical range imaging sensors". In: *Machine Vision and Applications* 1.2 (1988), pp. 127–152.

[172] R. G. Dorsch, G. Hausler, and J. M. Herrmann. "Laser triangulation: Fundamental uncertainty in distance measurement". In: *Applied Optics* 33 (1994), pp. 1306–1314.

[173] J. F. Andersen, J. Busck, and H. Heiselberg. "Applications of high resolution laser radar for 3-D multispectral imaging". In: *Proceedings of SPIE* 6214 (2006), p. 28.

[174] J. Schilling et al. "A model system for two-dimensional and three-dimensional photonic crystals: macroporous silicon". In: *Journal of Optics A: Pure and Applied Optics* 3.6 (2001), S121.

[175] R. Wu et al. "The Influence of Quantum Confinement on Third-Order Nonlinearities in Porous Silicon Thin Films". In: *Applied Sciences* 8.10 (2018), p. 1810.

[176] T. Moss, T. Hawkins, and G. Burrell. "Use of plasma edge reflection measurements in the study of semiconductors". In: *Journal of Physics C: Solid State Physics* 1.5 (1968), p. 1435.

[177] T. Roger et al. "Enhanced carrier-carrier interaction in optically pumped hydrogenated nanocrystalline silicon". In: *Applied Physics Letters* 101.14 (Oct. 2012), p. 141904.

[178] Y. Fang et al. "Ultrafast all-optical modulation in Fe-doped GaN at 1.31 and 1.55 $\mu$m with high contrast and ultralow power". In: *Applied Physics Letters* 110.16 (2017), p. 161902.

[179] J. Hynecek. *Method and apparatus for using surface trap recombination in solid state imaging devices*. US Patent 4,679,212. 1987.

[180] A. Bazin et al. "Ultrafast all-optical switching and error-free 10 Gbit/s wavelength conversion in hybrid InP-silicon on insulator nanocavities using surface quantum wells". In: *Applied Physics Letters* 104.1 (2014), p. 011102.

[181] K. Nozaki et al. "Sub-femtojoule all-optical switching using a photonic-crystal nanocavity". In: *Nature Photonics* 4.7 (2010), p. 477.

[182] J. Barreto, T. Roger, and A. Kaplan. "Resolving the ultrafast dynamics of charge carriers in nanocomposites". In: *Applied Physics Letters* 100.24 (2012), p. 241906.

[183] C. Jung, S. Yee, and K. Kuhn. "Electro-optic modulator based on surface plasmon resonance". In: *Applied Optics* 34 (1995), p. 946.

[184] A. Zakar et al. "MWIR optical modulation using structured silicon membranes". In: *Emerging Imaging and Sensing Technologies*. Vol. 9992. International Society for Optics and Photonics. 2016, p. 999203.

[185] J. B. Heaney, K. P. Stewart, and G. Hass. "Transmittance and reflectance of crystalline quartz and high- and low-water content fused silica from 2 $\mu$m to 1 mm". In: *Applied Optics* 22.24 (1983), pp. 4069–4072.

[186] A. Yariv and P. Yeh. *Photonics*. 6th. Oxford University Press, 2007.

[187] J. D. Irwin. *The Industrial Electronics Handbook*. 1st. CRC Press, 1997.

[188] T. C. O'Haver. *A Pragmatic Introduction to Signal Processing: with applications in scientific measurement*. 2nd. CreateSpace Independent Publishing Platform, 2016.

[189] I. H. Malitson. "Interspecimen Comparison of the Refractive Index of Fused Silica". In: *Journal of the Optical Society of America* 55.10 (Oct. 1965), pp. 1205–1209.

[190] C. Z. Tan. "Determination of refractive index of silica glass for infrared wavelengths by IR spectroscopy". In: *Journal of Non-Crystalline Solids* 223.1 (1998), pp. 158–163.

[191] T. Radhakrishnan. "Further Studies on the Temperature Variation of the Refractive Index of Crystals". In: *Proceedings of the Indian Academy of Sciences* 31 (1951), pp. 22–34.

[192] V. G. Kravets et al. "Plasmonic surface lattice resonances: a review of properties and applications". In: *Chemical Reviews* 118.12 (2018), pp. 5912–5951.

[193] K. E. Fong and L.-Y. L. Yung. "Localized surface plasmon resonance: a unique property of plasmonic nanoparticles for nucleic acid detection". In: *Nanoscale* 5.24 (2013), pp. 12043–12071.

[194] H. Chen et al. "Shape-and size-dependent refractive index sensitivity of gold nanoparticles". In: *Langmuir* 24.10 (2008), pp. 5233–5237.

[195] S. Zeng et al. "Nanomaterials enhanced surface plasmon resonance for biological and chemical sensing applications". In: *Chemical Society Reviews* 43.10 (2014), pp. 3426–3452.

[196] J.-F. Masson. "Portable and field-deployed surface plasmon resonance and plasmonic sensors". In: *Analyst* 145 (2020), pp. 3776–3800.

[197] A. Aubry et al. "Plasmonic light-harvesting devices over the whole visible spectrum". In: *Nano Letters* 10.7 (2010), pp. 2574–2579.

[198] Y. Y. Lee et al. "Plasmonic metamaterials for chiral sensing applications". In: *Nanoscale* 12.1 (2020), pp. 58–66.

[199] W. P. Hall et al. "A calcium-modulated plasmonic switch". In: *Journal of the American Chemical Society* 130.18 (2008), pp. 5836–5837.

[200] Y. Leroux et al. "Active plasmonic devices with anisotropic optical response: a step toward active polarizer". In: *Nano Letters* 9.5 (2009), pp. 2144–2148.

[201] J. Ki et al. "Sensitive plasmonic detection of miR-10b in biological samples using enzyme-assisted target recycling and developed LSPR probe". In: *ACS Applied Materials & Interfaces* 11.21 (2019), pp. 18923–18929.

[202] A. J. Haes et al. "Detection of a biomarker for Alzheimer's disease from synthetic and clinical samples using a nanoscale optical biosensor". In: *Journal of the American Chemical Society* 127.7 (2005), pp. 2264–2271.

[203] D. Furtado et al. "Overcoming the blood–brain barrier: the role of nanomaterials in treating neurological diseases". In: *Advanced Materials* 30.46 (2018), p. 1801362.

[204] M. J. Natan et al. *SERS substrates formed by hydroxylamine seeding of colloidal metal nanoparticle monolayers*. US Patent 6,624,886. Sept. 2003.

[205] T. R. Jensen et al. "Nanosphere lithography: tunable localized surface plasmon resonance spectra of silver nanoparticles". In: *The Journal of Physical Chemistry B* 104.45 (2000), pp. 10549–10556.

[206] F.-C. Chen et al. "Plasmonic-enhanced polymer photovoltaic devices incorporating solution-processable metal nanoparticles". In: *Applied Physics Letters* 95.1 (2009), p. 182.

[207] M. Kahraman et al. "Fundamentals and applications of SERS-based bioanalytical sensing". In: *Nanophotonics* 6.5 (2017), pp. 831–852.

[208] G. Demirel et al. "Surface-enhanced Raman spectroscopy (SERS): an adventure from plasmonic metals to organic semiconductors as SERS platforms". In: *Journal of Materials Chemistry C* 6.20 (2018), pp. 5314–5335.

[209] I. Pastoriza-Santos et al. "Plasmonic polymer nanocomposites". In: *Nature Reviews Materials* 3.10 (2018), pp. 375–391.

[210] S. Mokkapati et al. "Polarization tunable, multicolor emission from core–shell photonic III–V semiconductor nanowires". In: *Nano Letters* 12.12 (2012), pp. 6428–6431.

[211] A. Casadei et al. "Photonic–plasmonic coupling of GaAs single nanowires to optical nanoantennas". In: *Nano Letters* 14.5 (2014), pp. 2271–2278.

[212] L. Tang et al. "Nanometre-scale germanium photodetector enhanced by a near-infrared dipole antenna". In: *Nature Photonics* 2.4 (2008), pp. 226–229.

[213] M. Ren et al. "Nanostructured plasmonic medium for terahertz bandwidth all-optical switching". In: *Advanced Materials* 23.46 (2011), pp. 5540–5544.

[214] M. W. Knight et al. "Photodetection with active optical antennas". In: *Science* 332.6030 (2011), pp. 702–704.

[215] M. Z. Alam et al. "Large optical nonlinearity of nanoantennas coupled to an epsilon-near-zero material". In: *Nature Photonics* 12.2 (2018), pp. 79–83.

[216] M. Ren, W. Cai, and J. Xu. "Tailorable dynamics in nonlinear optical metasurfaces". In: *Advanced Materials* 32.3 (2020), p. 1806317.

[217] J. Sasai and K. Hirao. "Relaxation behavior of nonlinear optical response in borate glasses containing gold nanoparticles". In: *Journal of Applied Physics* 89.8 (2001), pp. 4548–4553.

[218] N. Pinçon et al. "Third-order nonlinear optical response of Au: SiO 2 thin films: Influence of gold nanoparticle concentration and morphologic parameters". In: *European Physical Journal D* 19.3 (2002), pp. 395–402.

[219] W. He et al. "Reconstructing charge-carrier dynamics in porous silicon membranes from time-resolved interferometric measurements". In: *Scientific Reports* 8.1 (2018), pp. 1–7.

[220] E. Le Ru et al. "Surface enhanced Raman scattering enhancement factors: a comprehensive study". In: *The Journal of Physical Chemistry C* 111.37 (2007), pp. 13794–13803.

[221] P. Mao et al. "Broadband single molecule SERS detection designed by warped optical spaces". In: *Nature Communications* 9.1 (2018), pp. 1–8.

[222] B. S. Wherrett and S. D. Smith. In: *Physica Scripta* T13 (1986), p. 189.

[223] C. Koos et al. "All-optical high-speed signal processing with silicon–organic hybrid slot waveguides". In: *Nature Photonics* 3.4 (2009), pp. 216–219.

[224] U. Keller et al. "Semiconductor saturable absorber mirrors (SESAM's) for femtosecond to nanosecond pulse generation in solid-state lasers". In: *IEEE Journal of Selected Topics in Quantum Electronics* 2.3 (1996), pp. 435–453.

[225] H. A. Haus. "Theory of mode locking with a fast saturable absorber". In: *Journal of Applied Physics* 46.7 (1975), pp. 3049–3058.

[226] N. R. Jana, L. Gearheart, and C. J. Murphy. "Wet chemical synthesis of high aspect ratio cylindrical gold nanorods". In: *The Journal of Physical Chemistry B* 105.19 (2001), pp. 4065–4067.

[227] M. Grzelczak et al. "Shape control in gold nanoparticle synthesis". In: *Chemical Society Reviews* 37.9 (2008), pp. 1783–1791.

[228] D. E. Newbury. "Mistakes encountered during automatic peak identification of minor and trace constituents in electron-excited energy dispersive X-ray microanalysis". In: *Scanning: The Journal of Scanning Microscopies* 31.3 (2009), pp. 91–101.

[229] K. Minami et al. "High resolution projection X-ray microscope equipped with fluorescent X-ray analyzer and its applications". In: *Journal of Physics: Conference Series*. Vol. 186. 1. IOP Publishing. 2009, p. 012010.

[230] G.-C. Li, Y.-L. Zhang, and D. Y. Lei. "Hybrid plasmonic gap modes in metal film-coupled dimers and their physical origins revealed by polarization resolved dark field spectroscopy". In: *Nanoscale* 8.13 (2016), pp. 7119–7126.

[231] H. Frohlich. *Theory of Dielectrics. 2nd.* Vol. 57. 1958, pp. 592–601.

[232] S. Nath et al. "Silver organosol: synthesis, characterisation and localised surface plasmon resonance study". In: *New Journal of Chemistry* 29.12 (2005), pp. 1527–1534.

[233] P. Nordlander et al. "Plasmon hybridization in nanoparticle dimers". In: *Nano Letters* 4.5 (2004), pp. 899–903.

[234] W. Rechberger et al. "Optical properties of two interacting gold nanoparticles". In: *Optics Communications* 220.1-3 (2003), pp. 137–141.

[235] R. Wu et al. "Localised plasmon field effect of gold clusters embedded in nanoporous silicon". In: *Advanced Optical Materials* 0.2002119 (2021).

[236] P. B. Johnson and R.-W. Christy. "Optical constants of the noble metals". In: *Physical Review B* 6.12 (1972), p. 4370.

[237] D. Bruggeman. "Effective medium model for the optical properties of composite materials". In: *Annals of Physics* 24 (1935), p. 636.

[238] M. Khardani, M. Bouaıcha, and B. Bessaıs. "Bruggeman effective medium approach for modelling optical properties of porous silicon: comparison with experiment". In: *Physica Status Solidi C* 4.6 (2007), pp. 1986–1990.

[239] G.-N. Xiao and S.-Q. Man. "Surface-enhanced Raman scattering of methylene blue adsorbed on cap-shaped silver nanoparticles". In: *Chemical Physics Letters* 447.4-6 (2007), pp. 305–309.

[240] A. Kaminska et al. "Chemically bound gold nanoparticle arrays on silicon: assembly, properties and SERS study of protein interactions". In: *Physical Chemistry Chemical Physics* 10.28 (2008), pp. 4172–4180.

[241] P. Spizzirri et al. "Nano-Raman spectroscopy of silicon surfaces". In: *arXiv preprint arXiv:1002.2692* (2010).

[242] C. Li et al. "Analysis of trace methylene blue in fish muscles using ultra-sensitive surface-enhanced Raman spectroscopy". In: *Food Control* 65 (2016), pp. 99–105.

[243] C. Srichan et al. "Highly-sensitive surface-enhanced Raman spectroscopy (SERS)-based chemical sensor using 3D graphene foam decorated with silver nanoparticles as SERS substrate". In: *Scientific Reports* 6 (2016), p. 23733.

[244] S. D. Roy et al. "Charge transfer mechanism and the adsorptive stance of methylene blue on gold nanocolloids: a vis-à-vis aftermath". In: *Journal of Raman Spectroscopy* 48.1 (2017), pp. 38–45.

[245] R. R. Naujok, R. V. Duevel, and R. M. Corn. "Fluorescence and Fourier transform surface-enhanced Raman scattering measurements of methylene blue adsorbed onto a sulfur-modified gold electrode". In: *Langmuir* 9.7 (1993), pp. 1771–1774.

[246] K.-D. Shim and E.-S. Jang. "SERS Signal Enhancement of Methylene Blue-embedded Agglomerated Gold Nanorod@ SiO2 Core@ Shell Composites". In: *Bulletin of the Korean Chemical Society* 39.8 (2018), pp. 936–940.

[247] Y. Wang et al. "Surface enhanced Raman scattering of p-aminothiophenol self-assembled monolayers in sandwich structure fabricated on glass". In: *The Journal of Chemical Physics* 124.7 (2006), p. 074709.

[248] M. Green and F. M. Liu. "SERS substrates fabricated by island lithography: the silver/pyridine system". In: *The Journal of Physical Chemistry B* 107.47 (2003), pp. 13015–13021.

[249] K. Wu et al. "Wafer-Scale Polymer-Based Transparent Nanocorals with Excellent Nanoplasmonic Photothermal Stability for High-Power and Superfast SERS Imaging". In: *Advanced Optical Materials* 7.23 (2019), p. 1901413.

[250] E. C. Le Ru and P. G. Etchegoin. "Quantifying SERS enhancements". In: *MRS Bulletin* 38.8 (2013), p. 631.

[251] E. J. Blackie, E. C. Le Ru, and P. G. Etchegoin. "Single-molecule surface-enhanced Raman spectroscopy of nonresonant molecules". In: *Journal of the American Chemical Society* 131.40 (2009), pp. 14466–14472.

[252] L. Litti and M. Meneghetti. "Predictions on the SERS enhancement factor of gold nanosphere aggregate samples". In: *Physical Chemistry Chemical Physics* 21.28 (2019), pp. 15515–15522.

[253] D. Wang and M. Kerker. "Enhanced Raman scattering by molecules adsorbed at the surface of colloidal spheroids". In: *Physical Review B* 24.4 (1981), p. 1777.

[254] V. Joseph et al. "SERS enhancement of gold nanospheres of defined size". In: *Journal of Raman Spectroscopy* 42.9 (2011), pp. 1736–1742.

[255] C. Hrelescu et al. "Single gold nanostars enhance Raman scattering". In: *Applied Physics Letters* 94.15 (2009), p. 153113.

[256] S. L. Kleinman et al. "Structure enhancement factor relationships in single gold nanoantennas by surface-enhanced Raman excitation spectroscopy". In: *Journal of the American Chemical Society* 135.1 (2013), pp. 301–308.

[257] S. Hong and X. Li. "Optimal size of gold nanoparticles for surface-enhanced Raman spectroscopy under different conditions". In: *Journal of Nanomaterials* 2013 (2013).

[258] A. Wei et al. "Tunable surface-enhanced Raman scattering from large gold nanoparticle arrays". In: *ChemPhysChem* 2.12 (2001), pp. 743–745.

[259] S. A. Trauger et al. "High sensitivity and analyte capture with desorption/ionization mass spectrometry on silylated porous silicon". In: *Analytical Chemistry* 76.15 (2004), pp. 4484–4489.

[260] H. C. Hulst and H. C. van de Hulst. *Light Scattering by Small Particles*. New York, US: Courier Corporation, 1981.

[261] S. Babar and J. Weaver. "Optical constants of Cu, Ag, and Au revisited". In: *Applied Optics* 54.3 (2015), pp. 477–481.

[262] V. Y. Timoshenko et al. "Anisotropy of optical absorption in birefringent porous silicon". In: *Physical Review B* 67.11 (2003), p. 113405.

[263] A. D. Rakić et al. "Optical properties of metallic films for vertical-cavity optoelectronic devices". In: *Applied Optics* 37.22 (1998), pp. 5271–5283.

[264] A. O. Govorov et al. "Photogeneration of hot plasmonic electrons with metal nanocrystals: Quantum description and potential applications". In: *Nano Today* 9.1 (2014), pp. 85–101.

[265] G. Rosenblatt et al. "Nonmodal plasmonics: controlling the forced optical response of nanostructures". In: *Physical Review X* 10.1 (2020), p. 011071.

[266] C. F. Bohren. "How can a particle absorb more than the light incident on it?" In: *American Journal of Physics* 51.4 (1983), pp. 323–327.

[267] A. D. Neira et al. "Eliminating material constraints for nonlinearity with plasmonic metamaterials". In: *Nature Communications* 6.1 (2015), pp. 1–8.

[268] M. Z. Alam, I. De Leon, and R. W. Boyd. "Large optical nonlinearity of indium tin oxide in its epsilon-near-zero region". In: *Science* (2016), aae0330.

[269] L. M. Lambert. "Free Carrier Reflectivity in Optically Homogeneous Silicon". In: *Physica Status Solidi A* 11 (1972), p. 461.

[270] K. Sokolowski-Tinten and D. von der Linde. "Generation of dense electron-hole plasmas in silicon". In: *Physical Review B* 61.4 (2000), p. 2643.

[271] I. P. Nikolakakos et al. "Broadband characterization of the nonlinear optical properties of common reference materials". In: *IEEE Journal of Selected Topics in Quantum Electronics* 10.5 (2004), pp. 1164–1170.

[272] L. Zhang et al. "Nonlinear Group IV photonics based on silicon and germanium: from near-infrared to mid-infrared". In: *Nanophotonics* 3.4-5 (2014), pp. 247–268.

[273] B.-U. Sohn et al. "Nonlinear optical properties of germanium at mid-infrared wavelengths (Conference Presentation)". In: *Nonlinear Optics and its Applications 2018*. Vol. 10684. International Society for Optics and Photonics. 2018, p. 1068403.

[274] M. T. Trinh, R. Limpens, and T. Gregorkiewicz. "Experimental investigation and modeling of Auger recombination in silicon nanocrytals". In: *The Journal of Physical Chemistry C* 117 (2013), p. 5963.

[275] M. Korinek et al. "Picosecond dynamics of photoexcited carriers in interacting silicon nanocrystals". In: *Applied Surface Science* 377 (2016), p. 238.

[276] R. Narayanan and M. A. El-Sayed. "Shape-dependent catalytic activity of platinum nanoparticles in colloidal solution". In: *Nano Letters* 4.7 (2004), pp. 1343–1348.

[277] M. K. Sarmast and H. Salehi. "Silver nanoparticles: an influential element in plant nanobiotechnology". In: *Molecular Biotechnology* 58.7 (2016), pp. 441–449.

[278] B. Zhang et al. "Au-Encapsulated Fe Nanorods in Oxide Matrix with Tunable Magneto-Optic Coupling Properties". In: *ACS Applied Materials & Interfaces* 12.46 (2020), pp. 51827–51836.

[279] M. Sheik-Bahae et al. "Sensitive measurement of optical nonlinearities using a single beam". In: *IEEE Journal of Quantum Electronics* 26.4 (1990), pp. 760–769.

[280] C. B. De Araújo, A. S. Gomes, and G. Boudebs. "Techniques for nonlinear optical characterization of materials: a review". In: *Reports on Progress in Physics* 79.3 (2016), p. 036401.

[281] M. Dinu, F. Quochi, and H. Garcia. "Third-order nonlinearities in silicon at telecom wavelengths". In: *Applied Physics Letters* 82.18 (2003), pp. 2954–2956.

[282] A. D. Bristow, N. Rotenberg, and H. M. Van Driel. "Two-photon absorption and Kerr coefficients of silicon for 850–2200 nm". In: *Applied Physics Letters* 90.19 (2007), p. 191104.

[283] B. Gu et al. "Theory of Gaussian beam Z scan with simultaneous third-and fifth-order nonlinear refraction based on a Gaussian decomposition method". In: *The Journal of the Optical Society of America B* 22.12 (2005), pp. 2651–2659.

[284] S. Lettieri et al. "Nonlinear optical refraction of free-standing porous silicon layers". In: *Optics Communications* 168.5-6 (1999), pp. 383–391.

[285] B. Qiu et al. "First-principles simulation of electron mean-free-path spectra and thermoelectric properties in silicon". In: *Europhysics Letters* 109.5 (2015), p. 57006.